Nonlinear Acoustics in Underwater and Biomedical Applications: Array Performance Degradation and Time Reversal Invariance

Ibrahim M. Hallaj

A dissertation submitted in partial fulfillment of
the requirements for the degree of

Doctor of Philosophy

University of Washington

1999

Program Authorized to Offer Degree: Electrical Engineering

19991101 041

University of Washington

Graduate School

This is to certify that I have examined this copy of a doctoral dissertation by
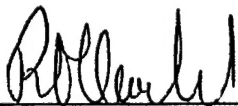
Ibrahim M. Hallaj

and have found that it is complete and satisfactory in all respects,
and that any and all revisions required by the final
examining committee have been made.
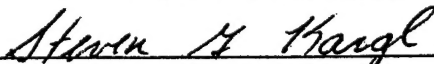
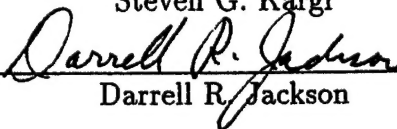Chair of Supervisory Committee:

_____
Robert P. Porter

Reading Committee:

_____
Robin O. Cleveland

_____
Steven G. Kargl

_____
Darrell R. Jackson

Date: May 21, 1999

University of Washington

Abstract

Nonlinear Acoustics in Underwater and Biomedical Applications: Array Performance Degradation and Time Reversal Invariance

by Ibrahim M. Hallaj

Chair of Supervisory Committee

Professor Robert P. Porter
Electrical Engineering

This dissertation describes a model for acoustic propagation in inhomogeneous fluid media, and explores the focusing by arrays onto targets under various conditions. The work explores the use of arrays, such as the phase-conjugate array, for underwater and biomedical applications. Aspects of propagation and phasing which can lead to reduced focusing effectiveness are described. Among the most important debilitating effects studied here are medium absorption, medium nonlinearity, and imperfect initial phasing of the signals at the array elements.

Acoustic wave propagation in fluid media is modeled by obtaining a wave equation from the basic equations of fluid mechanics, and some description of the propagating environment and its boundaries. The acoustic wave equation couples the wave motion to the medium's scalar and vector time-varying properties. Bulk velocity, sound speed, density, attenuation coefficient and nonlinearity parameter are all generally functions of three-dimensional space as well as time in an inhomogeneous medium.

The present study uses analysis and numerical simulations to study the behavior of the acoustic focusing systems described. The finite-difference time-domain (FDTD)

method is used to solve the wave equation for some applications in underwater and biomedical acoustics. The nature of the propagation of acoustic disturbances in space and time in a continuous medium suggest the numerical methods used to solve them here. The acoustic pressure disturbances are communicated along spatial and temporal grids in a natural fashion. The strengths and weaknesses of the FDTD method are discussed.

Beyond modeling and simulating the propagation and focusing of acoustic fields, this dissertation looks at the heating effects of focused ultrasound in an absorbing thermoviscous fluid. The application considered is the deposition of ultrasonic energy onto target tissue regions with the purpose of affecting therapeutic heating for hyperthermia. The acoustic model and a thermal model for tissue are coupled to solve for transient and steady temperature profiles in tissue-like media. Conclusions are presented on the effect of absorption, nonlinearity, and temperature-dependent medium properties.

TABLE OF CONTENTS

LIST OF FIGURES

iv

LIST OF TABLES

ACKNOWLEDGMENTS

The author wishes to express a sincere shout-out to a bunch of nice folks.

DEDICATION

To my Homies.

Chapter 1

INTRODUCTION

The focusing of intense acoustic beams onto targets can be used to advantage in military, industrial, and biomedical applications. It may seem ironic that the utility of the intense acoustic pressures generated by such devices is often in its useful destructive abilities. For example, focused sound may provide fast, safe minesweeping capability for ships at sea. Focused ultrasonic fields have been successfully used to break off oxidants and contaminants from semiconductor surfaces without the use of solvents or direct contact by abrasives. Further, the heat generated near regions of focused ultrasound has found application in welding plastic parts in industry, and in treatment of deep-seated tumors in tissue. In all of these examples focused sound was used to cause physical change to the region of application, most commonly causing permanent destruction of the material at the focus. This aspect is shared with lasers in that intense laser beams are often used in industrial, medical, and military applications to destroy objects in the beam. Contrast this usage with the nondestructive diagnostic and imaging uses of sound and laser light which are the most common usage for these beams at low intensities.

This study explores the propagation of intense sound beams from focused sources to propagate intense beams to a region of interest. Applications to focusing from phase conjugate arrays, and biomedical use for therapeutic tissue heating are considered. The emphasis of the study is on the physics of the wave propagation, the debilitating effects on focusing ability which may arise, and the modeling and behavior of tissue-

like media near the focus of ultrasonic beams.

In Chapter 2 a model for acoustic wave propagation will be developed. The model is used to study the motion of ultrasonic pulses propagating in inhomogeneous fluid media. First we consider wave motion in a quiescent, inhomogeneous, lossy, nonlinear thermoviscous fluid medium. Next, propagation in non-quiescent (time-varying) media is considered. Since the propagation can be very complicated, computer simulations are used to study the behavior of the acoustic field, especially near the focal zone. The finite-difference time-domain (FDTD) method for solving the wave equation is briefly outlined at the end of the chapter to facilitate the presentation of some numerical examples from the model.

Chapter 3 presents formal derivations for the field due to point sources using the Green's function. The analysis is extended to arrays of small sources and extended sources in free space. The superposition of linear acoustic fields is used to illustrate the need for geometric focusing and phasing to form intense foci. A discussion of beamsteering and some common configurations for focused acoustic sources are presented as well.

Chapter 4 considers time reversal or phase conjugation arrays. Such arrays have been shown to have remarkable abilities to automatically compensate for the effects of complicated propagation paths, scattering, and multipath effects in fluid channels. In this study we demonstrate analytically and through numerical experiments that the robustness of time reversal arrays for retrofocusing holds even under nonlinear propagation conditions. The caveat to this last statement is that the propagation medium must be nearly lossless, and no modification to the signal other than time reversal may be applied at the array. The effect of various debilitating factors on the ability of such arrays to form an intense focus at a target location is studied. For high-intensity purposes, absorption, amplification at the array elements, and error in phasing will compromise the time reversal invariance necessary for effective time reversal focusing. All of these effects act to degrade the focusing of time reversal

systems, and are shown to be especially detrimental for finite-amplitude propagation. An effort is made to elucidate the effects of individual propagation conditions on the propagation and array focusing, so minimizing the number of simultaneously acting phenomena will minimize confusion as to cause and effect. So for example, in studies investigating the effect of phase error on the focusing performance, the absorption and nonlinearity are suppressed so as not to cloud the issues being studied in that example.

In Chapter 5 the effects of focused ultrasound in tissue are studied. A thermal model for tissue-like media, based on the bioheat equation, is coupled to the previously described acoustic model. A heat equation is solved where the deposition of thermal energy into the tissue from focused ultrasound is countered by conduction and perfusion heat losses. It is known that material properties such as sound speed and absorption coefficient in biological media are temperature-dependent. The effect of the acoustic heating on the thermal and acoustic properties of tissue will have a feedback effect on the sound field and rate of heat deposition. The effect of time/temperature-varying sound speed and absorption coefficient is studied in simulations, using published laboratory data for these parameters as a function of temperature. It is found that the sharp increase in absorption coefficient as a heating treatment progresses will have an important effect on the rest of the treatment by accelerating the heating near the focal zone.

Each chapter is individually summarized at its end, but Chapter 6 ties the dissertation together by presenting conclusions from the findings of the whole study in a coherent fashion. Chapter 6 also describes some outstanding questions not addressed in this dissertation, and proposes some directions for extending this work. Some of the most important points not covered in the present study are the role of moving medium in time reversal systems, the role of time-varying properties of tissue other than sound speed and attenuation (for example, density, nonlinearity coefficient, viscosity), and the onset of phase change to treated tissue following the denaturing, or

cavitation inception. Only the phase errors in the initial phasing of time reversal systems were studied. Phase errors in the waveforms themselves can also be expected in real systems. Given the present interest in the ability of forming high-intensity foci using time reversal arrays, the time reversal systems are evaluated here based on the intensity of the focal spot generated, not on the fidelity of reproduction of the initial waveforms. This may not be the preferred judgement criterion in some of the "softer" uses of time reversal arrays, such as communication or imaging.

The present study relies heavily on numerical simulations. While all the algorithms and computer codes used in this study are original, the numerical methods used are not new. Hence the description of the numerical techniques used is discussed in the Appendix rather than in the body of the dissertation. Some comments regarding the simulation graphical output are due: to simplify reproduction of this dissertation, gray-scale coloring was used for all figures. Unfortunately, this compromised some of the detail visible in the original color output. A few colored versions of this dissertation were produced, but the official document remains in black and white. Also, some insight was gained by generating and viewing animated sequences of acoustic pulse propagation, especially for time reversal and therapeutic ultrasound pulse propagation. These too remain archived with the author and could not be included in the official dissertation. The simulations presented were carried out on the Silicon Graphics (Origin 2000) parallel computer at Boston University using the Cray parallellizing FORTRAN-77 compiler. Postprocessing was done on the Origin 2000 and Apple Macintosh computers. No Intel Pentium chips were used in this study.

Chapter 2

MODELLING THE ACOUSTIC WAVE

The first step to simulating an acoustic field is to decide on a model for sound propagation. This chapter derives the model wave equation from the basic equations of fluid mechanics and thermodynamics for a thermoviscous fluid. This study concerns itself with the compressional acoustic wave action in fluid media. The existence or generation of shear waves is not considered. The wave equation of acoustics can be derived from the fundamental equations of fluid mechanics and thermodynamics. In order to retain the nonlinear behaviour of the wave, it is necessary to retain the nonlinear terms which arise in the derivations. We keep terms up to second order in this study, a regime referred to as *finite-amplitude acoustics*. Keeping terms of higher than second order results in much more complicated expressions.

2.1 The Basic Equations of Fluid Mechanics and State in Quiescent Fluids

The equations used to derive the wave equation in fluids are Euler's equations (continuity and momentum), and an equation of state relating pressure to density and entropy. The derivations in this section apply to quiescent fluids[1], the case of fluids with time-varying background properties will be derived later in this chapter. The continuity equation expresses the conservation of mass in a fluid volume, and is given

---

[1] Defined by Pierce [61] p.14 as a fluid whose background properties are not dependent on time, and whose background velocity, $\mathbf{u}_0$, is zero.

by Kundu [51] as

$$\frac{\partial \rho}{\partial t} + \nabla \cdot (\rho \mathbf{u}) = 0, \tag{2.1}$$

where the density, ρ, and the velocity, $\mathbf{u}$, are both functions of space and time. Acoustic disturbances are considered to be small perturbations to the background state of the fluid, and the density, velocity, and pressure are written

$$\rho = \rho_0 + \rho', \tag{2.2}$$

$$\mathbf{u} = \mathbf{u}_0 + \mathbf{u}' \tag{2.3}$$

$$p = p_0 + p'. \tag{2.4}$$

The quantities with the subscript zero refer to the fluid's background (ambient) properties and are only functions of space, while the quantities having the superscript prime refer to perturbations from the background state due to the acoustic wave, and are generally functions of both space and time. Since $\mathbf{u}_0 = 0$ in all of the cases treated in this study, $\mathbf{u} = \mathbf{u}'$.

Expanding (2.1) and using (2.2) we obtain the continuity equation for a quiescent inhomogeneous fluid,

$$\frac{\partial \rho'}{\partial t} + \rho_0 \nabla \cdot \mathbf{u}' = -\rho' \nabla \cdot \mathbf{u}' - \mathbf{u}' \cdot \nabla \rho' - \mathbf{u}' \cdot \nabla \rho_0. \tag{2.5}$$

In a homogeneous medium, the last term in (2.5) would be dropped.

The next piece of fluid mechanics we will use to derive the wave equation is the momentum equation,

$$\rho \frac{D\mathbf{u}}{Dt} + \nabla p - \mathbf{F}_B - (\lambda + 2\mu)\nabla(\nabla \cdot \mathbf{u}) = 0, \tag{2.6}$$

where p' is the acoustic pressure, t is time, and μ and λ are the viscous Lamé coefficients. D denotes a material derivative,

$$\frac{D}{Dt} = \frac{\partial}{\partial t} + \mathbf{u} \cdot \nabla. \tag{2.7}$$

The body force F_B and the gradient of the background pressure, ∇p_0 cancel, since in the absence of sound, $p' = \mathbf{u} = 0$, and so (2.6) is merely

$$\nabla p_0 = \mathbf{F}_B. \tag{2.8}$$

A question may arise as to the importance of each term in the equations of fluid mechanics to the overall behavior of the fluid. To answer this question and to elucidate more of the nature of the acoustics we use an ordering scheme that clarifies which terms are small compared to the others. In this study terms of the order three and higher are ignored.

2.2 On the Ordering of Terms

We shall describe the basis for ordering the terms encountered throughout our analysis. We assume that background parameters (*e.g.* p_0, ρ_0, c_0) are of order one, denoted by $\mathcal{O}(1)$. Disturbances due to the acoustic waves are considered to be order epsilon, $\mathcal{O}(\epsilon)$, and are much smaller than the background values and $\mathcal{O}(1)$ terms. These include p', $\mathbf{u}'$, ρ', *etc.* The viscous (Lamé) coefficients are also considered small compared to the $\mathcal{O}(1)$ terms, and are first order terms denoted by $\mathcal{O}(\eta)$. Differential changes in background parameters (*e.g.* $\frac{\partial \rho_0}{\partial t}$ and $\nabla \rho_0$) are assumed to be $\mathcal{O}(\zeta)$ perturbations, where ϵ, η and ζ are all similarly-small and much less than one. Table 1.1 summarizes the ordering scheme used in this study. Note that the product of two first order terms is a second order term, thus allowing the substitution of first order terms into relations that are second order while maintaining second order accuracy. Note the distinction between the terms "order one", $\mathcal{O}(1)$, and "first order", $\mathcal{O}(\epsilon)$. Order one terms could be called "zeroth order" terms. Some examples using the ordering scheme described are

Table 2.1: The ordering scheme used in this study ($n \geq 0$, $m \geq 1$). ϵ, η and ζ are much smaller than 1. s represents space or time in the differentials.

$\frac{\partial^n p'^m}{\partial s^n}$	$\frac{\partial^n \mathbf{u}^m}{\partial s^n}$	$\frac{\partial^n \rho'^m}{\partial s^n}$	$\frac{\partial^n \rho_0^m}{\partial s^n}$	$\frac{\partial^n c_0^m}{\partial s^n}$	$\frac{\partial^n \kappa^m}{\partial s^n}$	$\frac{\partial^n \mu^m}{\partial s^n}$
$\mathcal{O}(\epsilon^m)$	$\mathcal{O}(\epsilon^m)$	$\mathcal{O}(\epsilon^m)$	$\mathcal{O}(\zeta^n)$	$\mathcal{O}(\zeta^n)$	$\mathcal{O}(\eta^{n+m})$	$\mathcal{O}(\eta^{n+m})$

$$
\begin{aligned}
\frac{1}{\rho_0 c_0^4} &= \mathcal{O}(1)\, \mathcal{O}(1^4) = \mathcal{O}(1), \quad \text{(zeroth order)} \\
\frac{\partial^3 p'}{\partial t^3} &= \mathcal{O}(1^3)\, \mathcal{O}(\epsilon) = \mathcal{O}(\epsilon), \quad \text{(first order)} \\
\frac{\partial^2 p'^2}{\partial t^2} &= \mathcal{O}(1^2)\, \mathcal{O}(\epsilon^2) = \mathcal{O}(\epsilon^2), \quad \text{(second order)} \\
p'^2 \frac{\partial c_0}{\partial t} &= \mathcal{O}(\epsilon^2)\, \mathcal{O}(\zeta) = \mathcal{O}(\epsilon^2\, \zeta) \quad \text{(third order)}.
\end{aligned}
\tag{2.9}
$$

Manipulation of second order relations such as (2.5) is possible using the first order relations described in [13, 68] while maintaining second order accuracy. For our purposes we use the first order linearized relations for mass and momentum conservation,

$$
\frac{\partial \rho'}{\partial t} = -\rho_0 \nabla \cdot \mathbf{u}', \tag{2.10}
$$

$$
\rho_0 \frac{\partial \mathbf{u}'}{\partial t} = -\nabla p', \tag{2.11}
$$

as well as a first order relation describing the dependence of density fluctuation on the background sound speed and the acoustic pressure,

$$
\rho' = \frac{1}{c_0^2} p'. \tag{2.12}
$$

These relations allow us to rewrite the right hand side of (2.5) to obtain a more useful form of the continuity equation,

$$
\frac{\partial \rho'}{\partial t} + \rho_0 \nabla \cdot \mathbf{u}' = \frac{1}{\rho_0 c_0^4} \frac{\partial p^2}{\partial t}, \tag{2.13}
$$

which will be used to derive the acoustic wave equation.

2.3 The Absorbing Nonlinear Wave Equation

A detailed treatment of the wave equation for nonlinear acoustics in fluids can be found in Hamilton and Blackstock [42]. To obtain the acoustic wave equation, the time derivative of equation (2.13),

$$\frac{\partial^2 \rho'}{\partial t^2} + \rho_0 \frac{\partial}{\partial t}(\nabla \cdot \mathbf{u}') = \frac{1}{\rho_0 c_0^4} \frac{\partial^2 p'^2}{\partial t^2} - \nabla \rho_0 \cdot \frac{\partial \mathbf{u}'}{\partial t}, \tag{2.14}$$

is subtracted from the divergence of equation (2.6)

$$\rho_0 \nabla \cdot \frac{\partial \mathbf{u}'}{\partial t} + \frac{\partial \mathbf{u}'}{\partial t} \cdot \nabla \rho_0 + \nabla^2 p' = (\lambda + 2\mu)\nabla^2(\nabla \cdot \mathbf{u}') + \nabla(\nabla \cdot \mathbf{u}') \cdot \nabla(\lambda + 2\mu),$$

$$\tag{2.15}$$

to yield

$$\nabla^2 p' - \frac{\partial^2 \rho'}{\partial t^2} + \frac{\partial \mathbf{u}'}{\partial t} \cdot \nabla \rho_0 - (\lambda + 2\mu)\nabla^2(\nabla \cdot \mathbf{u}') + \frac{1}{\rho_0 c_0^4} \frac{\partial^2 p'^2}{\partial t^2} - \nabla \rho_0 \cdot \frac{\partial \mathbf{u}'}{\partial t} = 0. \tag{2.16}$$

We return to the first order relations (2.10) and (2.11), and instead of (2.12) we use the state equation and entropy equations to second order, derived in Hamilton and Blackstock [42]

$$\rho' = \frac{p'}{c_0^2} - \frac{\kappa}{\rho_0 c_0^2}\left(\frac{1}{C_v} - \frac{1}{C_p}\right)\frac{\partial p'}{\partial t} - \frac{1}{\rho_0 c_0^4}\frac{B}{2A}p'^2, \tag{2.17}$$

where κ is the thermal conductivity, The constants A and B are the coefficients of the polynomial describing the relationship between the fluid's density and acoustic pressure variation described by Beyer [6]. B/A is proportional to the ratio of coefficients of the quadratic and linear terms in the Taylor series expression for pressure as a function of condensation. We use the second time derivative of (2.17),

$$\frac{\partial^2 \rho'}{\partial t^2} = \frac{1}{c_0^2}\frac{\partial^2 p'}{\partial t^2} - \frac{\kappa}{\rho_0 c_0^2}\left(\frac{1}{C_v} - \frac{1}{C_p}\right)\frac{\partial^3 p'}{\partial t^3} - \frac{B}{2A\rho_0 c_0^4}\frac{\partial^2 p'^2}{\partial t^2}, \tag{2.18}$$

to eliminate acoustic density from the nascent wave equation (2.16). We are now left with an equation with the acoustic pressure, p', as the sole dependent variable.

Collecting like terms, (2.16) can be written as

$$
\overbrace{\nabla^2 p' - \frac{1}{c_0^2}\frac{\partial^2 p'}{\partial t^2}}^{(a)} - \overbrace{\frac{1}{\rho_0}\nabla p \cdot \nabla \rho_0}^{(b)} + \overbrace{\frac{\kappa}{\rho_0 c_0^2}\left(\frac{1}{C_v} - \frac{1}{C_p}\right)\frac{\partial^3 p'}{\partial t^3}}^{(c)}
$$
$$
+ \overbrace{\frac{B}{2A\rho_0 c_0^4}\frac{\partial^2 p'^2}{\partial t^2}}^{(d)} + \overbrace{(\lambda + 2\mu)\frac{1}{\rho_0 c_0^4}\frac{\partial^3 p'}{\partial t^3}}^{(e)} + \overbrace{\frac{1}{\rho_0 c_0^4}\frac{\partial^2 p'^2}{\partial t^2}}^{(f)} = 0.
$$

(2.19)

The terms in the above equation are: (a) the D'Alembertian, present in all wave equations. This term describes the propagation of a pulse in time and space; (b) the ambient inhomogeneity in the medium's density, and is zero for a homogeneous medium; (c) and (e) the loss terms, due to the thermal conduction and the viscosity of the fluid respectively; and finally (d) and (f), the nonlinear terms arising from the equation of state and the continuity equation respectively. The nonlinear terms can be combined using the nonlinearity coefficient, β, which is related to the number B/A by

$$
\beta = 1 + \frac{B}{2A}.
$$

(2.20)

Simplification allows us to write the wave equation in terms of the acoustic diffusivity, δ, which accounts for both thermal and viscous losses, in a form attributed to Westervelt [73],

$$
\nabla^2 p' - \frac{1}{c_0^2}\frac{\partial^2 p'}{\partial t^2} - \frac{1}{\rho_0}\nabla p' \cdot \nabla \rho_0 + \frac{\delta}{c_0^4}\frac{\partial^3 p'}{\partial t^3} + \frac{\beta}{\rho_0 c_0^4}\frac{\partial^2 p'^2}{\partial t^2} = 0.
$$

(2.21)

We now have a second-order wave equation describing the acoustic pressure in terms of space, time, and the fluid's material properties.

The simulations presented in this study use an absorption coefficient, α, which is related to the acoustic diffusivity by

$$
\alpha = \frac{\delta \omega^2}{2c_0^3},
$$

(2.22)

and has the units of Nepers/meter [Np/m].

2.4   Similarity Solution for the Wave Equation in Quiescent Fluids

The wave equation (2.21) is given in its full dimensional form. Actual values for c_0, α_0, ρ_0, β_0, and source pressure, p_{source}, must be provided for the specific propagation medium under consideration to obtain a solution for that case. A useful technique that can be used to gain insight into the essential nature of the wave equation is a *similarity analysis*. The advantage of using similarity analysis is that two systems with different background parameters and driving pressures can be studied using the same solution, provided that certain nondimensional quantities that characterize the wave equation are the same for the two systems. This reduction of a differential equation to its simplest form with no explicit dimensional variables is also known as *nondimensionalizing* the equation. In this section we nondimensionalize a simplified version of (2.21) for illustration purposes in polar cylindrical coordinates in a homogeneous medium. The dimensional form of the wave equation is

$$\nabla^2 p' - \frac{1}{c_0^2}\frac{\partial^2 p'}{\partial t^2} + \frac{2\alpha}{c_0 \omega^2}\frac{\partial^3 p'}{\partial t^3} + \frac{2\beta}{\rho_0 c_0^4}\left[p'\frac{\partial^2 p'}{\partial t^2} + \left(\frac{\partial p'}{\partial t}\right)^2\right] = 0. \qquad (2.23)$$

A characteristic set of nondimensional variables with hats (*e.g.* $\hat{t}$) is used instead

of the dimensional variables (*e.g. t*) used in (2.23).

$$\hat{p} = \frac{p'}{p_{\text{source}}},$$
$$\hat{r} = \frac{r}{\tilde{\lambda}_0},$$
$$\hat{x} = \frac{x}{\tilde{\lambda}_0},$$
$$\hat{t} = t\omega,$$
$$\hat{c} = \frac{c}{c_0},$$
$$\hat{\rho} = \frac{\rho'}{\rho_0},$$
$$\hat{\alpha} = \frac{\alpha}{\alpha_0},$$
$$\hat{\beta} = \frac{\beta}{\beta_0},$$

(2.24)

The zero subscripts, (*e.g.* ρ_0) denote background values. In this case we take the background parameters to be constants, as the medium is assumed to be spatially homogeneous and quiescent.

In polar cylindrical coordinates the scalar Laplacian is

$$\nabla^2 p' = \frac{1}{r}\frac{\partial}{\partial r}\left(r\frac{\partial p'}{\partial r}\right) + \frac{\partial^2 p'}{\partial x^2} = \frac{\partial^2 p'}{\partial r^2} + \frac{1}{r}\frac{\partial p'}{\partial r} + \frac{\partial^2 p'}{\partial x^2},$$

(2.25)

where we have assumed axial symmetry exists and neglected any derivatives in azimuthal angle, θ. This is a useful geometry found in most experimental bowl transducers in research laboratories. The operators in (2.23) are nondimensionalized using the angular wavelength

$$\tilde{\lambda}_0 = \frac{c_0}{\omega},$$

(2.26)

and the transformations on the operators

$$\frac{\partial \hat{r}}{\partial r} = \frac{\partial}{\partial r}\left(\frac{r}{\tilde{\lambda}_0}\right) = \frac{1}{\tilde{\lambda}_0},$$

$$\frac{\partial p'}{\partial r} = \frac{p_{\text{source}}}{\tilde{\lambda}_0}\frac{\partial \hat{p}}{\partial \hat{r}},$$

$$\frac{\partial^2 p'}{\partial r^2} = \frac{p'}{\tilde{\lambda}_0^2}\frac{\partial^2 \hat{p}}{\partial \hat{r}^2},$$

$$\frac{\partial p'}{\partial x} = \frac{p_{\text{source}}}{\tilde{\lambda}_0}\frac{\partial \hat{p}}{\partial \hat{x}},$$

$$\frac{\partial^2 p'}{\partial x^2} = \frac{p'}{\tilde{\lambda}_0^2}\frac{\partial^2 \hat{p}}{\partial \hat{x}^2}, \qquad (2.27)$$

$$\frac{1}{r} = \frac{1}{\tilde{\lambda}_0\,\hat{r}},$$

$$\frac{\partial \hat{t}}{\partial t} = \frac{\partial}{\partial t}(t\omega) = \omega,$$

$$\frac{\partial p'}{\partial t} = \omega p_{\text{source}}\frac{\partial \hat{p}}{\partial \hat{t}},$$

$$\frac{\partial^2 p'}{\partial t^2} = \omega^2 p_{\text{source}}\frac{\partial^2 \hat{p}}{\partial \hat{t}^2},$$

$$\frac{\partial^3 p'}{\partial t^3} = \omega^3 p_{\text{source}}\frac{\partial^3 \hat{p}}{\partial \hat{t}^3}.$$

Applying the above transformations and multiplying through by $\left(\frac{\tilde{\lambda}_0^2}{p_{\text{source}}}\right)$ gives a dimensionless form of the wave equation in a homogeneous medium in cylindrical coordinates

$$\frac{\partial^2 \hat{p}}{\partial \hat{r}^2} - \frac{1}{\hat{r}}\frac{\partial \hat{p}}{\partial \hat{r}} + \frac{\partial^2 \hat{p}}{\partial \hat{x}^2} - \frac{\partial^2 \hat{p}}{\partial \hat{t}^2} + 2\,\alpha_0\,\tilde{\lambda}_0\,\frac{\partial^3 \hat{p}}{\partial \hat{t}^3} + \frac{2\,\beta_0\,p_{\text{source}}}{\rho_0\,c_0^2}\left[\hat{p}\frac{\partial^2 \hat{p}}{\partial \hat{t}^2} + \left(\frac{\partial \hat{p}}{\partial \hat{t}}\right)^2\right] = 0.$$
$$(2.28)$$

We pause now to examine the remaining factors in front of our operators in the nondimensional wave equation (2.28). Two points of primary importance are noted:

1. Two nondimensional terms are all that controls the behavior of any particular case of this equation, so long as the nondimensional factors are the same. These

factors are

$$\alpha_0 \, \tilde{\lambda}_0,$$

and

$$\frac{\beta_0 \, p_{\text{source}}}{\rho_0 \, c_0^2} = \beta_0 \, \epsilon. \qquad (2.29)$$

Note that the absorption term contains a factor called the absorption length $\alpha_0 \, \tilde{\lambda}_0$, which is the amount of absorption suffered in propagating the distance $\tilde{\lambda}_0$. Also note that the acoustic Mach number,

$$\epsilon = \frac{u_{\text{source}}}{c_0} = \frac{p_{\text{source}}}{\rho_0 \, c_0^2}, \qquad (2.30)$$

appears as a multiplier in front of the nonlinear term.

2. The ratio of the two nondimensional parameters in (2.29) is a measure of the importance of nonlinearity to absorption. This ratio is derived by Blackstock [7], and is called the Gol'berg number, Γ,

$$\Gamma = \frac{\beta_0 \epsilon}{\alpha_0 \tilde{\lambda}_0}. \qquad (2.31)$$

In the coming chapters we will see how the nonlinearity and the absorption both come into play in the propagation of finite-amplitude waves, and how the nonlinear steepening and the absorption are competing mechanisms in nonlinear wave propagation. Blackstock points out that the Gol'berg number can be used as an estimate of the overall nature of a pulse's propagation. If $\Gamma \gg 1$ then nonlinearity dominates and the waveforms will tend to develop steep shocked profiles, if $\Gamma \ll 1$ then absorption dominates and the waveform decays without severe steepening.

2.5 The Wave Equation with Time-Varying Background (TVB) Parameters

We re-derive the wave equation from the nonlinear equations of fluid mechanics and state, now allowing the background sound speed and density, $\rho_0(t)$ and $c_0(t)$, to be

time-varying. We refer to this as the time-varying background (TVB) scenario or solution. The motivation for deriving the TVB wave equation is that changes which occur to the background values of ρ_0 and c_0 at time scales comparable to those of the acoustic variables may contribute to the wave equation. The fluid's density and nonlinearity coefficients are assumed to remain constant. This constraint is born of the fact that only the primary propagation variable (sound speed) and the primary heating parameter (absorption coefficient) have been reported for tissue as a function of temperature. Thus for this analysis the density and nonlinearity coefficient are assumed to be constants.

The continuity equation (2.13) and the momentum equation (2.6) are manipulated as in Section 2.3, except that time-derivatives of $\rho_0(t)$ and $c_0(t)$ are assumed to be non-zero. These derivatives are taken to be first order terms. The continuity equation (2.1) is now

$$\frac{\partial \rho_0}{\partial t} + \frac{\partial \rho'}{\partial t} + \rho_0 \nabla \cdot \mathbf{u} = -\rho' \nabla \cdot \mathbf{u} - \mathbf{u} \cdot \nabla \rho' - \mathbf{u} \cdot \nabla \rho_0. \tag{2.32}$$

Equation (2.32) to first-order accuracy (neglecting $\mathcal{O}(\epsilon^2)$ and higher-order terms) is

$$\frac{\partial \rho_0}{\partial t} + \frac{\partial \rho'}{\partial t} + \rho_0 \nabla \cdot \mathbf{u} = 0 \tag{2.33}$$

from which we derive the first-order relations

$$\nabla \cdot \mathbf{u} = -\frac{1}{\rho_0} \frac{\partial \rho_0}{\partial t} - \frac{1}{\rho_0} \frac{\partial \rho'}{\partial t}, \tag{2.34}$$

$$\nabla^2 (\nabla \cdot \mathbf{u}) = -\frac{1}{\rho_0} \frac{\partial}{\partial t} \nabla^2 \rho'. \tag{2.35}$$

Next we consider the momentum equation,

$$\rho \frac{D\mathbf{u}}{Dt} + \nabla p - \mathbf{F}_B - (\lambda + 2\mu) \nabla (\nabla \cdot \mathbf{u}) = 0. \tag{2.36}$$

In the absence of sound, $p' = \mathbf{u} = 0$, and so the gradient of the background pressure and the body force cancel as in (2.8). So (2.36) for the TVB case to second order

accuracy is

$$\rho_0 \frac{\partial \mathbf{u}}{\partial t} + \nabla p' = -\rho' \frac{\partial \mathbf{u}}{\partial t} - \rho_0 \mathbf{u} \cdot \nabla \mathbf{u} + (\lambda + 2\mu)\nabla^2 \mathbf{u}, \tag{2.37}$$

where we have used the vector identity

$$\nabla(\nabla \cdot \mathbf{u}) = \nabla^2 \mathbf{u} + \nabla \times \nabla \times \mathbf{u} \tag{2.38}$$

and assumed that the flow is irrotational, *vis.* $\nabla \times \mathbf{u} = 0$. The momemtum equation to first-order accuracy in a TVB fluid can be written to first order

$$\frac{\partial \mathbf{u}}{\partial t} = -\frac{1}{\rho_0}\nabla p' + \mathcal{O}(\epsilon^2). \tag{2.39}$$

Note that this is identical to that of the quiescent medium.

A first order wave equation can be obtained by subtracting the time-derivative of (2.33) from the divergence of (2.39),

$$\nabla^2 p' - \frac{\partial^2 \rho'}{\partial t^2} = 0. \tag{2.40}$$

The equation of state for a TVB fluid is

$$p' = c_0^2 \rho' + \frac{\kappa}{\rho_0 C_p}(\gamma - 1)\frac{\partial \rho'}{\partial t} + \frac{c_0^2}{\rho_0}\frac{B}{2A}\rho'^2 + \mathcal{O}(\epsilon^3). \tag{2.41}$$

To first order this is

$$p' = c_0^2 \rho' + \mathcal{O}(\epsilon^2), \tag{2.42}$$

from which the first-order relations below may be derived

$$\begin{aligned}
\rho' &= \frac{1}{c_0^2}p' + \mathcal{O}(\epsilon^2), \\
\frac{\partial \rho'}{\partial t} &= \frac{1}{c_0^2}\frac{\partial p'}{\partial t} + \mathcal{O}(\epsilon^2), \\
\nabla \rho' &= \frac{1}{c_0^2}\nabla p' + \mathcal{O}(\epsilon^2).
\end{aligned} \tag{2.43}$$

The next step towards obtaining a second-order wave equation for nonlinear absorbing TVB media is to use first-order relations to eliminate ρ' and $\mathbf{u}$ from the wave

equation, and to express the equation in terms of p'. We write the continuity equation (2.32) as

$$
\begin{aligned}
\frac{\partial \rho_0}{\partial t} + \frac{\partial \rho'}{\partial t} + \rho_0 \nabla \cdot \mathbf{u} &= \frac{\rho'}{\rho_0} \frac{\partial \rho_0}{\partial t} + \frac{\rho'}{\rho_0} \frac{\partial \rho'}{\partial t} - \mathbf{u} \cdot \nabla \rho' - \mathbf{u} \cdot \nabla \rho_0 - \mathbf{u} \cdot \nabla \rho_0 \\
&= \frac{p'}{\rho_0 c_0^2} \frac{\partial \rho_0}{\partial t} + \frac{1}{2\rho_0 c_0^4} \frac{\partial p'^2}{\partial t} - \frac{\mathbf{u}}{c_0^2} \cdot \nabla p' - \mathbf{u} \cdot \nabla \rho_0 \\
&= \frac{p'}{\rho_0 c_0^2} \frac{\partial \rho_0}{\partial t} + \frac{1}{2\rho_0 c_0^4} \frac{\partial p'^2}{\partial t} + \frac{\rho_0}{2c_0^2} \frac{\partial u^2}{\partial t} - \mathbf{u} \cdot \nabla \rho_0 + \mathcal{O}(\epsilon^3).
\end{aligned}
\tag{2.44}
$$

If we define the Lagrangian density (*c.f.* Hamilton and Blackstock [42] Chapter 3)

$$
\mathcal{L} = \frac{1}{2} \rho_0 u^2 - \frac{p'^2}{2\rho_0 c_0^3},
\tag{2.45}
$$

then the quantity

$$
\frac{1}{c_0^2} \frac{\partial \mathcal{L}}{\partial t} = \frac{\rho_0}{2c_0^2} \frac{\partial u^2}{\partial t} - \frac{1}{2\rho_0 c_0^4} \frac{\partial p'^2}{\partial t} + \mathcal{O}(\epsilon^3),
\tag{2.46}
$$

so the continuity equation can be written as

$$
\frac{\partial \rho_0}{\partial t} + \frac{\partial \rho'}{\partial t} + \rho_0 \nabla \cdot \mathbf{u} = \frac{p'}{\rho_0 c_0^2} \frac{\partial \rho_0}{\partial t} + \frac{\partial p'^2}{\partial t} - \mathbf{u} \cdot \nabla \rho_0 + \frac{1}{c_0^2} \frac{\partial \mathcal{L}}{\partial t}.
\tag{2.47}
$$

Equation (2.47) is the same as that would be obtained in a quiescent fluid with the exception of the terms containing $\frac{\partial \rho_0}{\partial t}$, which are due to the TVB character of ρ_0.

We also rewrite the momentum equation for a TVB fluid (2.36) using the $\mathcal{O}(\epsilon)$ substitutions (2.35), (2.39), and (2.43),

$$
\begin{aligned}
\rho_0 \frac{\partial \mathbf{u}}{\partial t} + \nabla p' &= (\lambda + 2\mu) \nabla \left(-\frac{1}{\rho_0} \frac{\partial \rho_0}{\partial t} - \frac{1}{\rho_0} \frac{\partial \rho'}{\partial t} \right) + \frac{p'}{\rho_0 c_0^2} \nabla p' - \frac{\rho_0}{2} \nabla u^2 \\
&= -\frac{\lambda + 2\mu}{\rho_0} \nabla \frac{\partial \rho'}{\partial t} + \frac{1}{2\rho_0 c_0^2} \nabla p'^2 - \frac{\rho_0}{2} \nabla u^2 \\
&= -\frac{\lambda + 2\mu}{\rho_0} \nabla \frac{\partial \rho'}{\partial t} - \nabla \mathcal{L},
\end{aligned}
\tag{2.48}
$$

where the gradient of the Lagrangian density (2.45) is

$$
\nabla \mathcal{L} = \frac{\rho_0}{2} \nabla u^2 - \frac{\nabla p'^2}{2\rho_0 c_0^2}.
\tag{2.49}
$$

To obtain a wave equation we must subtract the time-derivative of (2.47),

$$\frac{\partial^2 \rho'}{\partial t^2} + \rho_0 \frac{\partial}{\partial t} \nabla \cdot \mathbf{u} = -\frac{\partial^2 \rho_0}{\partial t^2} - \nabla \cdot \mathbf{u} \frac{\partial \rho_0}{\partial t}$$
$$+ \frac{1}{\rho_0 c_0^2} \frac{\partial \rho_0}{\partial t} \frac{\partial p'}{\partial t} + \frac{1}{\rho_0 c_0^4} \frac{\partial^2 p'^2}{\partial t^2} + \frac{1}{c_0^2} \frac{\partial^2 \mathcal{L}}{\partial t^2}, \tag{2.50}$$

from the divergence of (2.48),

$$\nabla^2 p' + \rho_0 \frac{\partial}{\partial t} \nabla \cdot \mathbf{u} = -\frac{(\lambda + 2\mu)}{\rho_0 c_0^2} \nabla^2 \frac{\partial p'}{\partial t} - \nabla^2 \mathcal{L}, \tag{2.51}$$

to obtain, after substitutions and algebra,

$$\nabla^2 p' - \frac{\partial^2 \rho'}{\partial t^2} = -\frac{1}{\rho_0 c_0^4} \frac{\partial^2 p'^2}{\partial t^2} - \frac{(\lambda + 2\mu)}{\rho_0 c_0^2} \nabla^2 \frac{\partial p'}{\partial t} + \frac{\nabla \rho_0}{\rho_0} \cdot \nabla p'$$
$$+ \underbrace{\frac{\partial^2 \rho_0}{\partial t^2} - \frac{1}{\rho_0} \left(\frac{\partial \rho_0}{\partial t} \right)^2 - \frac{2}{\rho_0 c_0^2} \frac{\partial \rho_0}{\partial t} \frac{\partial p'}{\partial t}}_{TVB_{\rho_0}} - \left(\nabla^2 + \frac{\partial^2}{\partial t^2} \right) \mathcal{L}. \tag{2.52}$$

This is the "nascent" wave equation for the TVB case. The terms in (2.52) are similar to those derived for the quiescent case, with the addition of the terms labeled TVB_{ρ_0} which are due to the TVB nature of ρ_0. The background sound speed's contribution to the TVB terms will come about in the following equations where the equation of state is used to eliminate the ρ' from (2.52).

Applying first-order substitutions (2.43) to the state equation (2.41) gives a second-order expression for ρ' as

$$\rho' = \frac{1}{c_0^2} p' - \frac{\kappa}{C_p} (\gamma - 1) \frac{1}{c_0^4} \frac{\partial p'}{\partial t} - \frac{1}{\rho_0 c_0^4} \frac{B}{2A} p'^2 + \mathcal{O}(\epsilon^2). \tag{2.53}$$

Differentiation with respect to time twice gives

$$\frac{\partial^2 \rho'}{\partial t^2} = \frac{1}{c_0^2} \frac{\partial^2 p'}{\partial t^2} - \frac{1}{\rho_0 c_0^4} \frac{B}{2A} \frac{\partial^2 p'^2}{\partial t^2} - \frac{1}{\rho_0 c_0^4} \frac{\kappa(\gamma - 1)}{C_p} \frac{\partial^3 p'}{\partial t^3} - \underbrace{\frac{4}{c_0^3} \frac{\partial p'}{\partial t} \frac{\partial c_0}{\partial t}}_{TVB_{c_0}}, \tag{2.54}$$

where the term labeled TVB_{c_0} is a result of the TVB nature of c_0.

Substituting (2.54) into (2.52) eliminates the ρ' variable from the wave equation, leaving the wave equation for the TVB medium as

$$\nabla^2 p' - \frac{1}{c_0^2}\frac{\partial^2 p'}{\partial t^2} = -\frac{1}{\rho_0 c_0^4}\frac{\partial^2 p'^2}{\partial t^2}\left(1 + \frac{B}{2A}\right) - \frac{(\lambda + 2\mu)}{\rho_0 c_0^4}\frac{\partial^3 p'}{\partial t^3} - \frac{1}{\rho_0 c_0^4}\frac{\kappa(\gamma - 1)}{C_p}\frac{\partial^3 p'}{\partial t^3}$$
$$+ TVB_{\rho_0} + TVB_{c_0} - \left(\nabla^2 + \frac{\partial^2}{\partial t^2}\right)\mathcal{L},$$

$$(2.55)$$

or after some manipulation, and neglecting the $\mathcal{L}$ terms,

$$\nabla^2 p' - \frac{1}{c_0^2}\frac{\partial^2 p'}{\partial t^2} + \frac{\delta}{c_0^4}\frac{\partial^3 p'}{\partial t^3} + \frac{\beta}{\rho_0 c_0^4}\frac{\partial^2 p'^2}{\partial t^2} - \frac{1}{\rho_0}\nabla p' \cdot \nabla \rho_0$$
$$\underbrace{-\frac{\partial^2 \rho_0}{\partial t^2} + \frac{1}{\rho_0}\left(\frac{\partial \rho_0}{\partial t}\right)^2 + \frac{2}{\rho_0 c_0^2}\frac{\partial \rho_0}{\partial t}\frac{\partial p'}{\partial t} + \frac{4}{c_0^3}\frac{\partial p'}{\partial t}\frac{\partial c_0}{\partial t}}_{TVB_{\rho_0,c_0}} = 0.$$

$$(2.56)$$

Note that $\delta = b/\rho_0$ where $b = \lambda + 2\mu + \frac{\kappa}{\rho_0 C_p}(\gamma - 1)$.

As a comment, truncating higher than second order terms in the derivation of the above equations results in a reasonably compact wave equation. Keeping higher order terms than second order would result in significantly more complicated equations.

2.5.1 Nondimensionalizing the TVB Wave Equation

We nondimensionalize (2.56) for a one-dimensional case using characteristic nondimensional variables with hats (*e.g.* $\hat{\rho}_0$) as before, with some new nondimensional variables

$$\hat{c}_0 = \frac{c_0}{c_{00}},$$
$$\hat{\rho}_0 = \frac{\rho_0}{\rho_{00}},$$
$$\hat{\alpha}_0 = \frac{\alpha_0}{\alpha_{00}},$$
$$\hat{\beta}_0 = \frac{\beta_0}{\beta_{00}}.$$

$$(2.57)$$

The parameters with zero subscripts, (*e.g.* ρ_0) denote background values, which are functions of time[2]. The parameters with double-zero subscripts (*e.g.* ρ_{00}) are background parameters of the undisturbed background state of the fluid before any interactions altering the background properties take place in the fluid, and are constants.

The wave equation in nondimensional form is

$$
\frac{\partial^2 \hat{p}}{\partial \hat{x}^2} - \frac{1}{\hat{c}_0^2}\frac{\partial^2 \hat{p}}{\partial \hat{t}^2} + \frac{\hat{\alpha}_0}{\hat{c}_0}\alpha_{00}\tilde{\lambda}_{00}\frac{\partial^3 \hat{p}}{\partial \hat{t}^3} + \frac{\hat{\beta}_0}{\hat{\rho}_0\hat{c}_0^2}\frac{\beta_{00}p_{\text{source}}}{\rho_{00}c_{00}^2}\frac{\partial^2 \hat{p}^2}{\partial \hat{t}^2} - \rho_{00}\frac{\partial \hat{p}}{\partial \hat{x}}\frac{\partial \hat{\rho}_0}{\partial \hat{x}}
$$
$$
- \frac{\partial^2 \hat{\rho}_0}{\partial \hat{t}^2} + \frac{1}{\hat{\rho}_0}\left(\frac{\partial \hat{\rho}_0}{\partial \hat{t}}\right)^2 + \frac{2}{\hat{\rho}_0\hat{c}_0^2}\frac{\partial \hat{\rho}_0}{\partial \hat{t}}\frac{\partial \hat{p}}{\partial \hat{t}} + \frac{4}{\hat{c}_0^3}\frac{\partial \hat{p}}{\partial \hat{t}}\frac{\partial \hat{c}_0}{\partial \hat{t}} = 0.
$$
(2.58)

2.5.2 Ordering the Terms in the TVB Wave Equation

In subsequent chapters on thermal effects of focused ultrasound we will find it convenient to show that not all terms from (2.58) need to be computed if some are much smaller than the others. To this end, we now examine (2.58)'s terms to set their magnitudes to some scale for comparison.

For reasonable amounts of variation, the background parameters are $\mathcal{O}(1)$,

$$
\hat{c}_0,\ \hat{\rho}_0,\ \hat{\alpha}_0,\ \hat{\beta}_0 = \mathcal{O}(1),
$$
(2.59)

because for any background parameter χ_0

$$
\hat{\chi}_0 = \frac{\chi_0}{\chi_{00}} = \frac{\mathcal{O}(1)}{\mathcal{O}(1)}.
$$
(2.60)

We can thus drop the *hatted* groups of parameters leading the terms in (2.58) as $\mathcal{O}(1)$, so

$$
\frac{\partial^2 \hat{p}}{\partial \hat{x}^2} - \frac{\partial^2 \hat{p}}{\partial \hat{t}^2} + \alpha_{00}\tilde{\lambda}_{00}\frac{\partial^3 \hat{p}}{\partial \hat{t}^3} + \frac{\beta_{00}p_{\text{source}}}{\rho_{00}c_{00}^2}\frac{\partial^2 \hat{p}^2}{\partial \hat{t}^2} - \rho_{00}\frac{\partial \hat{p}}{\partial \hat{x}}\frac{\partial \hat{\rho}_0}{\partial \hat{x}}
$$
$$
- \frac{\partial^2 \hat{\rho}_0}{\partial \hat{t}^2} + \left(\frac{\partial \hat{\rho}_0}{\partial \hat{t}}\right)^2 + \frac{\partial \hat{p}}{\partial \hat{t}}\frac{\partial \hat{\rho}_0}{\partial \hat{t}} + \frac{\partial \hat{p}}{\partial \hat{t}}\frac{\partial \hat{c}_0}{\partial \hat{t}} = 0.
$$
(2.61)

---

[2]We assume that some mechanism changes the background properties. In the case of focused ultrasound surgery, background parameters have been measured to be functions of temperature. Since the temperature of the tissue in this case is time-dependent, so are the background properties.

In order to determine the importance of the terms relative to one another, we rewrite (2.61) as

$$
\begin{aligned}
\frac{\partial^2 \hat{p}}{\partial \hat{x}^2} - \frac{\partial^2 \hat{p}}{\partial \hat{t}_a^2} + \alpha_{00}\tilde{\lambda}_{00}\frac{\partial^3 \hat{p}}{\partial \hat{t}_a^3} + \frac{\beta_{00}p_{\text{source}}}{\rho_{00}c_{00}^2}\frac{\partial^2 \hat{p}^2}{\partial \hat{t}_a^2} - \rho_{00}\frac{\partial \hat{p}}{\partial \hat{x}}\frac{\partial \hat{\rho}_0}{\partial \hat{x}} \\
- \frac{\tau_a^2}{\tau_b^2}\frac{\partial^2 \hat{\rho}_0}{\partial \hat{t}_b^2} + \left(\frac{\tau_a}{\tau_b}\frac{\partial \hat{\rho}_0}{\partial \hat{t}_b}\right)^2 + \frac{\tau_a}{\tau_b}\frac{\partial \hat{p}}{\partial \hat{t}_a}\frac{\partial \hat{\rho}_0}{\partial \hat{t}_b} + \frac{\tau_a}{\tau_b}\frac{\partial \hat{p}}{\partial \hat{t}_a}\frac{\partial \hat{c}_0}{\partial \hat{t}_b} = 0,
\end{aligned}
\tag{2.62}
$$

where two nondimensional times have been defined corresponding to the acoustic and the thermal time scales:

$$
\hat{t}_a = \frac{t}{\tau_a},
\tag{2.63}
$$

$$
\hat{t}_b = \frac{t}{\tau_b},
\tag{2.64}
$$

and we used the manipulation (an example is given here),

$$
\frac{\partial \hat{c}_0}{\partial \hat{t}_a} = \frac{\partial \hat{c}_0}{\partial \hat{t}_b}\frac{\partial \hat{t}_b}{\partial \hat{t}_a} = \frac{\partial \hat{c}_0}{\partial \hat{t}_b}\frac{\partial (t/\tau_b)}{\partial (t/\tau_a)} = \frac{\partial \hat{c}_0}{\partial \hat{t}_b}\frac{\tau_a}{\tau_b}.
\tag{2.65}
$$

Now that the equation is written in terms of partial derivatives which are all order unity, we can now use the factor τ_a/τ_b as an estimator of relative magnitudes of the terms.

$$
\begin{aligned}
\overbrace{\frac{\partial^2 \hat{p}}{\partial \hat{x}^2}}^{\mathcal{O}(1)} - \overbrace{\frac{\partial^2 \hat{p}}{\partial \hat{t}_a^2}}^{\mathcal{O}(1)} + \overbrace{\alpha_{00}\tilde{\lambda}_{00}\frac{\partial^3 \hat{p}}{\partial \hat{t}_a^3}}^{\mathcal{O}(\alpha_{00}\tilde{\lambda}_{00})} + \overbrace{\frac{\beta_{00}p_{\text{source}}}{\rho_{00}c_{00}^2}\left[\hat{p}\frac{\partial^2 \hat{p}}{\partial \hat{t}_a^2} + \left(\frac{\partial \hat{p}}{\partial \hat{t}_a}\right)^2\right]}^{\mathcal{O}(\beta_{00}p_{\text{source}}/\rho_{00}c_{00}^2)} \\
- \overbrace{\frac{\tau_a^2}{\tau_b^2}\frac{\partial^2 \hat{\rho}_0}{\partial \hat{t}_b^2}}^{\mathcal{O}(\tau_a/\tau_b)^2} + \overbrace{\left(\frac{\tau_a}{\tau_b}\frac{\partial \hat{\rho}_0}{\partial \hat{t}_b}\right)^2}^{\mathcal{O}(\tau_a/\tau_b)^2} + \overbrace{\frac{\tau_a}{\tau_b}\frac{\partial \hat{p}}{\partial \hat{t}_a}\frac{\partial \hat{\rho}_0}{\partial \hat{t}_b}}^{\mathcal{O}(\tau_a/\tau_b)} + \overbrace{\frac{\tau_a}{\tau_b}\frac{\partial \hat{p}}{\partial \hat{t}_a}\frac{\partial \hat{c}_0}{\partial \hat{t}_b}}^{\mathcal{O}(\tau_a/\tau_b)} = 0.
\end{aligned}
\tag{2.66}
$$

As an example, we perform an order-of-magnitude analysis of (2.66) for the case of soft tissue medium insonated by a sinusoid at acoustic angular frequency ω_a of 1 MHz. Our experience [37], and laboratory measurements [45, 11, 65] at typical therapeutic biomedical device source pressures (1 MPa) shows that for an acoustic source with period $\tau_a = 1\mu s$, tissue heating occurs over time scales on the order of $\tau_b = 1s$. Thus

$$
\frac{\tau_a}{\tau_b} \approx 10^{-6}.
\tag{2.67}
$$

For typical background reference properties of soft tissue,

$$c_{00} = 1600 \text{ m/s},$$

$$\rho_{00} = 1100 \text{ kg/m}^3,$$

$$\alpha_{00} = 4.5 \text{ Np/m}, \qquad (2.68)$$

$$\beta_{00} = 5.5,$$

we conclude that the D'Alembertian terms in (2.66) are of magnitude unity, the absorption and the nonlinear terms are of magnitude 10^{-3}, and the TVB terms are of magnitude 10^{-6} and 10^{-12}. This result shows formally that for hyperthermia applications (to be discussed in detail in Chapter 5) the TVB is negligible in its effect on the wave equation. In other words, the acoustic field is not measurably influenced by the change in tissue background parameters when viewed at time scales τ_a.

2.5.3 Conclusions Regarding the Wave Equation for TVB media

The analysis suggests that dynamic background medium properties, $\rho_0(t)$ and $c_0(t)$, can be important enough to be included in a second-order wave equation. The nondimensionalized equations suggest that the time-variation of ρ_0 and c_0 can be neglected if the characteristic time of change for these parameters is much longer than the acoustic characteristic time scale, the period. From this we conclude that while in the biomedical ultrasound example at 1 MHz and higher we don't expect temperature-driven variations in tissue parameters to be fast enough to be included in the acoustic wave equation calculations. The simulations to be shown in Chapter 5, run over the time of several seconds, do show that the variation in background parameters (especially α) is very important to temperature predictions in the focal region.

This analysis is distinct from analysis of spatially-varying media as a debilitating factor in time reversal arrays. Propagation in the ocean over long enough ranges to allow the channel to change appreciably over the time scale of propagation from source to array is possible. Dowling [22] and Dowling and Jackson [21] studied this

effect, and conclude that while the time reversal process is robust enough to allow for good retrofocusing even in realistic ocean channel conditions, the beamwidth is increased. Experimental evidence for this was provided by Kuperman *et al.* [52], who suspended a 400 Hz vertical line array in the Mediterranean Sea, and were able to successfully focus onto a source 6.3 km away from the array.

Chapter 3

FOCUSED SOURCES AND ARRAYS

In this chapter basic terminology and concepts of focusing are presented. The application of focusing to time reversal arrays and therapeutic ultrasound devices is left until later specialized chapters on these topics. The means of controlling the position of a focal spot are described here, and some simple implementations of the wave propagation model developed in Chapter 2 are shown and compared to solutions by other methods for verification.

3.1 Fields in Free Space

Our goal is to use multiple sources to construct an extended focused source or an array. We begin with a description of the acoustic field due to a single source much smaller than a wavelength, commonly known as a *point source*.

3.1.1 The Green's function in free space

A periodically-varying mass in unbounded space having spherical symmetry has a harmonic complex field. The Green's function at some spatial location $\mathbf{x}$ due to a source at $\mathbf{x}_s$, denoted by $G(\mathbf{x}|\mathbf{x}_s)$, is defined as the solution to the inhomogeneous Helmholtz equation,

$$(\nabla^2 + k^2)\, G(\mathbf{x}|\mathbf{x}_s) = -4\pi\, \delta(\mathbf{x} - \mathbf{x}_s), \tag{3.1}$$

where the Dirac delta function $\delta(\mathbf{x} - \mathbf{x}_s)$ is an impulsive source at position $\mathbf{x}_s$. The solution to this equation in an unbounded medium is the *free-space Green's function*,

$$G(\mathbf{x}|\mathbf{x}_s) = \frac{e^{ikR}}{R}, \tag{3.2}$$

where the displacement $R = |x - x_s|$. This shows that a field due to a point source in free-space will experience a $1/R$ decay without any medium attenuation. A focused source uses the combined fields from many small (or an extended) sources. The sources are geometrically arranged so that a stronger field results at locations where the arrivals from the individual component sources meet. The gain obtained by allowing the fields of many small sources (or the integrated extended source) to add up is called *geometric gain*. For linear acoustics, this gain is the result of superposition, and is an algebraic sum of the individual fields of the component sources.

3.2 Focusing Using Arrays

This section describes an acoustic source consisting of more than one active element (an *array*) driven in some deliberate fashion to affect a localized region of heightened average acoustic intensity in space, time, or both, called a *focus*. The position of the focus in space and time is determined by the geometry and phase relation of the array elements, as well as propagation path parameters.

For focusing in the linear acoustics case using the superposition principle and multiple transducer elements, a wide body of literature exists demonstrating the theory and application of linear array beamsteering [19, 62, 69]. The focusing can be performed mechanically by placement of the elements, exploiting their geometry, or electronically by applying phasing to the driving signals, [62]. Lithotripsy and therapeutic focused ultrasound treatment are examples of the use of focusing to form an intense acoustic field at some desired location, while diagnostic imaging and sonar are examples of using electronic beamforming to locate and identify objects in the acoustic beam.

3.2.1 Parameters we cannot control

In most applications the propagation path is given by the nature of the application. In underwater and biological applications, the path can be complicated. The presence of scatterers, three-dimensional inhomogeneous medium, as well as absorption, non-linearity, and dispersion, make it difficult to model the propagation in these media. We will see how phased arrays and time reversal systems can be used to overcome some of the difficulties associated with obtaining a focus in such complicated media.

3.2.2 Parameters we can control

Typically, we can specify the geometry of an array only during its manufacture. Since the array is usually an expensive component of the hardware, arrays must be carefully designed for the purpose at hand for best efficiency. Once an array is chosen, the phasing of the elements is the parameter most often used to create and position the focus. This process is called *beamforming*, and has long been used to advantage in underwater engineering applications. Mechanical manipulation of the array as well as electronic beamsteering can be used to move the main lobe of a focused array. Diagnostic ultrasound equipment generates images of extended regions using such techniques to construct a multi-dimensional image from several snapshots (B-scans) in the receive mode along a direction.

3.3 Linear Arrays

Perhaps the simplest manifestation of multiple-element sources is the linear array, consisting of multiple elements arranged along a straight line. Note that a linear array refers to its geometry, and should be distinguished by context from the term used to describe small-signal acoustics. Figure 3.1 shows a diagram of a simple linear array. For an inter-element separation, d, and a sound speed, c, we can calculate some relations for phasing the elements of a linear array for focusing purposes by
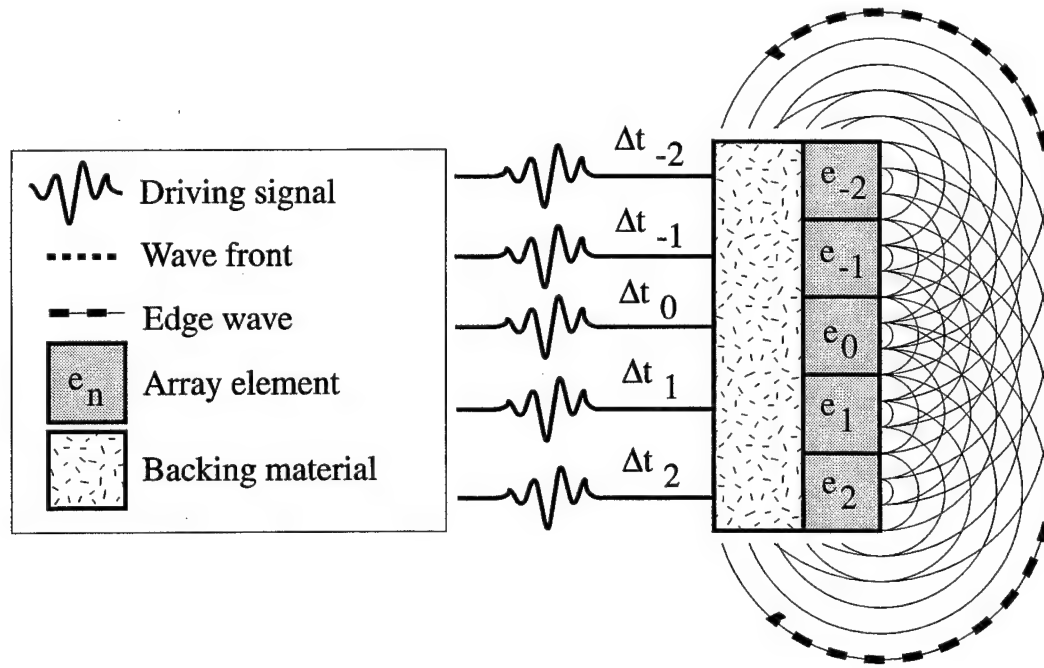
Figure 3.1: A line array of sources phased by time delays Δt_n.

controlling the time delay for the nth element, Δt_n. The richness of the device can be appreciated by considering the following few control scenarios:

- Beamsteering: making the time delays, Δt_n, increase linearly, $\Delta t_{n+1} = \Delta t_n + \delta$. This will cause the main wave front to propagate along a direction other than normal to the face of the transducer array. The time delays to affect this steering are,

$$\Delta t_n = n\frac{d}{c}\sin\theta + T. \tag{3.3}$$

- Focusing: including a quadratic variation in the time delays to obtain focusing at some range, F, as well as steering angle, θ. In this case the time delays are

given by Von Ramm and Smith [62] as,

$$\Delta t_n = \frac{F}{c}\left(1 - \left[1 + \left(\frac{nd}{F}\right)^2 - 2\frac{nd}{F}\sin\theta\right]^{1/2}\right) + T. \qquad (3.4)$$

- Sidelobe reduction: including array shading, whereby various amplitude-weighting windows are applied to the array aperture. This is also known as *apodization.* The cross-sectional intensity profile of a beam may be controlled using such techniques. This can be used to reduce the normally unwanted sidelobes or grating lobes of a beam, where acoustic energy is heightened at periodic angular directions by constructive interference from periodic array sources.

Note that an overall time offset, T, is added to the delays to preclude any of the time delays in this causal system from being negative.

Other details such as individual element directivities are not considered in this dissertation, but will affect the overall array field pattern. In the case of linear acoustics, such field patterns are routinely studied and calculated and measured for individual arrays at the time of manufacture. For finite-amplitude acoustics it is generally not possible to calculate field patterns due to the nonlinearity and possible interaction between the fields of the individual elements, except via approximations, laboratory measurements, and computer simulations.

3.4 Arrays with Polar Axial Symmetry

Figure 3.2 shows some geometries of focused sources with axial symmetry. Such source geometries are commonly found in applied and research settings. In (a) a single element in the shape of a bowl achieves its focus at the center of curvature. Single-element spherical bowls are common in hyperthermia research labs, and while they provide little flexibility, they are relatively simple to use. Another simple single-element focused source is shown in (b), and uses an acoustic lens with a different

sound speed than the surrounding propagation medium to produce the focusing. This configuration is also simple to use, but requires knowledge of the properties of the lens and the propagation medium [54, 53]. In addition, problems of heating can occur in the lens due to absorption. Another common source is shown in (c), and
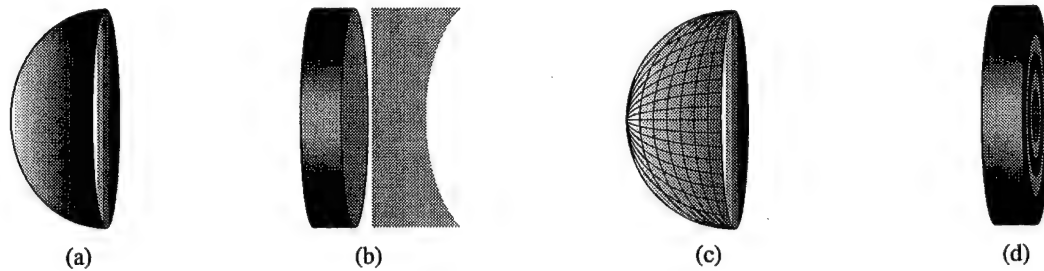
Figure 3.2: A focused source can be obtained by manufacturing a single element as a bowl (a), a single flat piston source with a curved acoustic lens (b), an array of elements arranged on a bowl (c), or a flat annular array (d).

consists of multiple small elements arranged on the face of a bowl-shaped substrate. This configuration requires sophisticated driving electronics to operate correctly, but provides more flexibility in forming the focus than a single-element, and allows more advanced control of sidelobes for example. Finally, (d) shows a flat annular array, which allows for positioning of a focus along the axis of symmetry of the array. Grating lobes in annular arrays depend on geometry, number of elements, and wavelength, but can be reduced by increasing the bandwidth of the signals [23]. While (a) and (b) are only capable of one focus, the use of banks of array elements in groups allows (c) and (d) to form multiple foci if desired [24].

Numerically, we consider arrays of finite aperture as consisting of many electroacoustic transducer elements which have no appreciable spatial extent themselves, and which may be driven independently by an external signal generator. This suggests the term "sampled aperture" as a descriptor of an array. Another common modeling assumption is to take the frequency responses of all the elements to be identical, *i.e.*,

the elements have the same transfer functions. If we assume that the total resulting acoustic field is the linear superposition of the fields from each of the small sources we can compute the CW field quite easily. Similarly, if the sources are pulsed, then a time-varying version of the field is obtained. The focusing is now both spatial and temporal, and simple time-of-flight calculations allow us to compute when and where the maximal intensity region will occur. Conversely, the focus can be achieved at the desired position and time by controlling the applied pulses with time delays in a predictable manner.

While this study is primarily interested in the time domain behavior of arrays, analogous statements can be made for the frequency domain representation of the array response. The frequency response of the array is the superposition of the frequency responses of the array elements.

An array may be used in a transmit (active) mode or in a receive (passive) mode assuming the transduction properties of the elements (both electric and acoustic) have such symmetry. This allows many array systems to be used for transmission of acoustic energy towards a given position, or to be used as a receiving device for recording sound, the greatest sensitivity being at the focus. Also, we can make the distinction between focusing at some range and beamsteering along some steering angle, however we will refer to the combined effect of these localizations in space as well as in time simply as *focusing*.

For random or inhomogeneous media, the Green's function of the propagation medium may not be known *a priori*, and the effects of medium variability may not be predicted entirely without using measuring instruments or numerical simulations.

3.5   A Numerical Example: 1-D Propagation

We now present a simple example of wave propagation using the model developed in this chapter. For the purposes of numerical modeling, the nonlinear term is expanded

into two terms, and the absorption coefficient is used. The wave equation is discretized and solved in the following form,

$$\nabla^2 p - \frac{1}{c_0^2}\frac{\partial^2 p}{\partial t^2} - \frac{1}{\rho_0}\nabla p \cdot \nabla \rho_0 + \frac{2\alpha}{c_0\omega^2}\frac{\partial^3 p}{\partial t^3} + \frac{2\beta}{\rho_0 c_0^4}\left[p\frac{\partial^2 p}{\partial t^2} + \left(\frac{\partial p}{\partial t}\right)^2\right] = 0. \qquad (3.5)$$

Solving an equation using finite differences involves discretizing the differentials in the partial differential equation via an expansion. The continuous variables are represented by discrete approximations, given in a matrix representing the computational grid and stored in computer memory. The finite-difference time-domain (FDTD) method is one of the oldest and most intuitive methods for solving differential equations on the computer. Details of the numerics are left for the Appendix.

For our example, a one-dimensional plane wave is propagated from a plane wave source in a homogeneous medium according to equation (3.5), in Cartesian coordinates,

$$\frac{\partial^2 p}{\partial x^2} - \frac{1}{c_0^2}\frac{\partial^2 p}{\partial t^2} - \frac{1}{\rho_0}\frac{\partial p}{\partial x}\frac{\partial \rho_0}{\partial x} + \frac{2\alpha}{c_0\omega^2}\frac{\partial^3 p}{\partial t^3} + \frac{2\beta}{\rho_0 c_0^4}\left[p\frac{\partial^2 p}{\partial t^2} + \left(\frac{\partial p}{\partial t}\right)^2\right] = 0. \qquad (3.6)$$

3.5.1 Solution Using the FDTD Method

Solving (3.6) numerically involves discretizing the unknown pressure field, $p(x, t)$ onto the spatial and temporal grids in computer memory. The discrete representation of the pressure is $p(x_i, t_n)$, or simply p_i^n, with integers $i = [1, 2, \dots, I_{max}]$ and $n = [1, 2, \dots, N_{max}]$. The grid locations are given by

$$x_i = x_0 + (i-1)\delta_x, \qquad (3.7)$$

$$t_n = t_0 + (n-1)\delta_t. \qquad (3.8)$$

where δ_t and δ_x are the separation between adjacent grid locations is time and space. Note that the present discussion is only valid for uniform grid spacing. The spatial extent of the simulation, or the computational domain, is $x = [x_0, (I_{\max} \delta_x)]$, and the simulation time frame is $t = [t_0, (N_{\max} \delta_t)]$.

The representation of the differentials is derived in the Appendix, but we list here the relevant expressions for the terms in the wave equation, accurate to $\mathcal{O}(\delta_x^2, \; \delta_t^2)$:

$$\frac{\partial^2 p}{\partial x^2} = \frac{1}{\delta_x^2} \overbrace{\left(p_{i+1}^n - 2p_i^n + p_{i-1}^n\right)}^{z_1} + \mathcal{O}(\delta_x^2),$$

$$\frac{\partial p}{\partial t} = \frac{1}{2\delta_t} \overbrace{\left(3p_i^n - 4p_i^{n-1} + p_i^{n-2}\right)}^{z_5} + \mathcal{O}(\delta_t^2),$$

$$\frac{\partial^2 p}{\partial t^2} = \frac{1}{\delta_t^2} (p_i^{n+1} \overbrace{-2p_i^n + p_i^{n-1}}^{z_2}) + \mathcal{O}(\delta_t^2), \quad \text{(centered)} \tag{3.9}$$

$$= \frac{1}{\delta_t^2} \overbrace{\left(2p_i^n - 5p_i^{n-1} + 4p_i^{n-2} - p_i^{n-3}\right)}^{z_4} + \mathcal{O}(\delta_t^2), \quad \text{(right-sided)}$$

$$\frac{\partial^3 p}{\partial t^3} = \frac{1}{2\delta_t^3} \overbrace{\left(6p_i^n - 23p_i^{n-1} + 34p_i^{n-2} - 24p_i^{n-3} + 8p_i^{n-4} - p_i^{n-5}\right)}^{z_3} + \mathcal{O}(\delta_t^2).$$

We assume that we know what the initial and all previous conditions of the pressure field are, *i.e.* all variables are known except the future values of $p(x, \; t)$. All pressures prior to $t = 0$ are initialized to zero in our simulations. A driving pulse is applied at source locations on the grid, which propagates according to the wave equation. The expressions (3.9) are substituted into (3.6) and rearranged to solve for pressure at the next time step, p_i^{n+1},

$$p_i^{n+1} = q_1 \; z_1 + q_2 \; z_3 + q_2 \left(p_i^n \; z_4 + \frac{z_5^2}{4} \right) - z_2, \tag{3.10}$$

where

$$q_1 = \frac{c^2 \delta_t^2}{12 \delta_x^2},$$

$$q_2 = \frac{\alpha c}{\delta_t \omega^2}, \tag{3.11}$$

$$q_2 = \frac{2\beta}{\rho c^2}.$$

3.5.2 Boundary Conditions

We impose absorbing boundary conditions (ABC) at the edges of the computational domain to prevent or to minimize reflections from the edges of the domain. By

doing so the simulations approximate the behavior of waves in infinite media. Low order ABC's are relatively easy to implement, for example using Kosloff and Kosloff's technique which applies a progressively more absorbing layer near the edges of the domain [50], while Mur's well-known method [60] applies a radiation condition

$$\frac{\partial p'}{\partial x} - \frac{1}{c_0}\frac{\partial p'}{\partial t} = 0. \tag{3.12}$$

The ABC's and their implementation will be left for the Appendix.

For simulations possessing polar cylindrical symmetry, only one half of the two-dimensional (r, x) domain is calculated, or $r = [0, r_{max}]$, $x = [x_{min}, x_{max}]$. The boundary condition at $r = 0$ is

$$\frac{\partial p'}{\partial r} = 0. \tag{3.13}$$

The boundary conditions along the other edges use radiation condition ABC's.

Chapter 4

TIME REVERSAL ARRAYS

Several factors are cited for reducing the quality of focusing or imaging with phased arrays [62]:

- nonideal response of transducer arrays and limitations in delay line systems

- refraction errors due to medium inhomogeneities

- target ambiguities due to phase quantization errors

A linear time reversal array (TRA) or phase-conjugate array can correct for all but the last deficiency of phased array systems listed above. By so doing, the TRA uses the medium as a matched filter to automatically generate the delays at each element for transmission and focusing [20]. Time reversal arrays are alternately called time reversal mirrors (TRM) owing to the way in which the array acts as a temporal mirror for the captured signals.

Time reversal mirrors have found several uses in medical and underwater applications [72, 67, 52]. The concept of time reversal is an extension of phase conjugation theory, which is known to hold for linear fields in reciprocal media [48, 27]. The time reversal array captures not only the initial phase, given by Δt_n, but also the waveform by sampling signals coming from the target through a propagation medium which ideally remains stationary. The basic operation of a TRM is explained in a number of articles by Fink [27, 28], and is illustrated in Figure 4.1 as a three-step process consisting of target illumination, signal collection, and time-reversed retransmission. Most

time reversal studies consider an abbreviated sequence of events, starting with the array receive mode (b), followed by the array transmit mode (c).
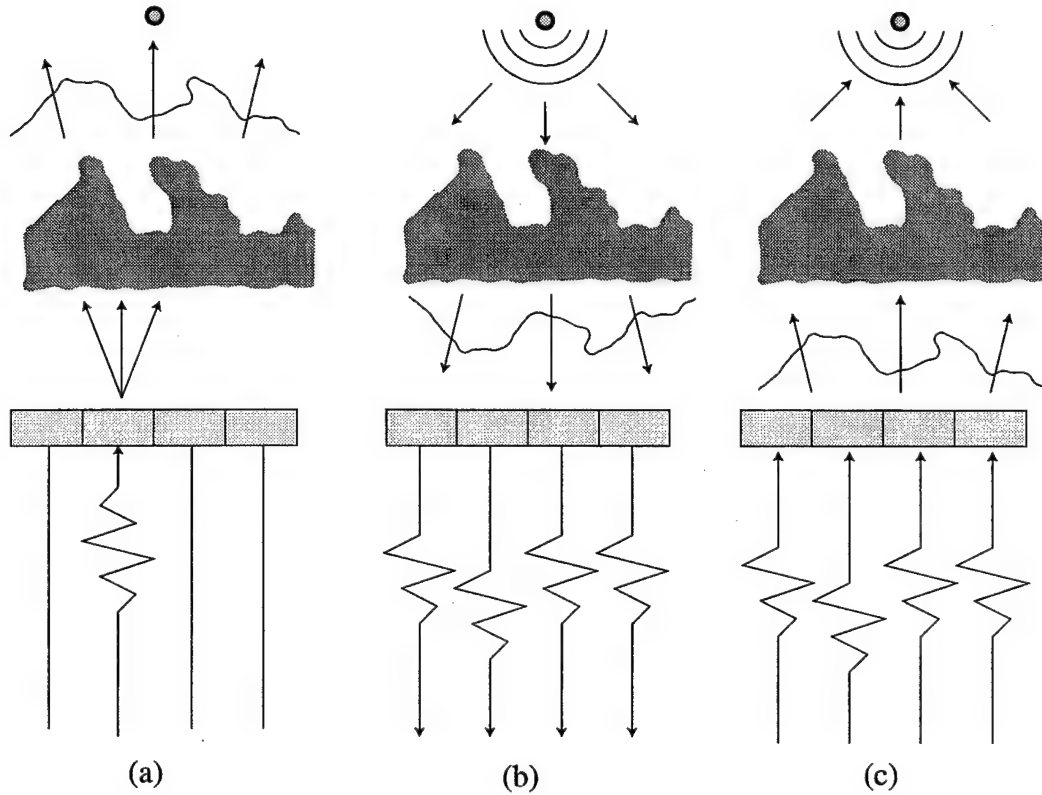
Figure 4.1: Time reversal array operation after Fink [27]. In (a) the target is illuminated by a pulse from a single element, in (b) the *receive mode* where the illuminated target acts as a small scatterer emitting a spherical pulse while the array is recording, in (c) the *transmit mode* the array retransmits the time-reversed pulses recorded in the receive mode.

4.1   Impulse Response Analysis

Fink [27] has described the behavior of linear time reversal systems in terms of the impulse response. The impulse function $\delta(t)$ can be used to describe the dynamics

of the reception and retransmission of acoustic pulses. The impulse response analysis to follow is after Fink [27]. If an array element E_i causes a (nondimensional) velocity excitation $v(t) = \delta(t)$, the acoustic velocity potential at some point in space, $\mathbf{x}_0$, is described by the diffraction impulse response $h_i^t(\mathbf{x}_0, t)$ for the illuminating (transmission) event due to E_i. A related impulse response $h_i^r(\mathbf{x}_0, t)$ can be defined for the receiving event due to an impulse source at $\mathbf{x}_0$. A very useful aspect of the time reversal system is that the exact impulse responses do not need to be known or calculated. What is necessary is that the transmit and the receive modes have identical impulse responses, whatever these may be.

This analysis is dependent on acoustic reciprocity. For a Green's function, $G(\mathbf{x}_0, t_0 | \mathbf{x}, t)$, representing the field at $\mathbf{x}$ at time t due to an impulse excited at $\mathbf{x}_0$ at time t_0, the reciprocity theorem for the Green's function states that

$$G(\mathbf{x}_0, t_0 | \mathbf{x}, t) = G(\mathbf{x}, t_0 | \mathbf{x}_0, t). \tag{4.1}$$

We can write the diffraction impulse responses in terms of the Green's functions over the transducer surface, S_i,

$$h_i^r(\mathbf{x}, t) = \int_{S_i} G(\mathbf{x}_0, t_0 | \mathbf{x}, t) dx, \tag{4.2}$$

$$h_i^t(\mathbf{x}_0, t) = \int_{S_i} G(\mathbf{x}, t_0 | \mathbf{x}_0, t) dx. \tag{4.3}$$

Therefore, we need not distinguish between the receive and the transmit mode diffraction impulse responses, since they are identical by (4.1). Using the notation of Fink [27], we simply denote these responses by $h_i(\mathbf{x}_0, t)$.

Another set of transfer functions need to be accounted for. That is the transfer functions describing the conversion of acoustic energy into electrical energy during the receive mode, $h_i^{ae}(t)$, and the conversion of electrical energy into acoustical energy during the transmit mode, $h_i^{ea}(t)$. These transfer functions are convolved with those of the propagation during the time reversal process. The steps of the time reversal operation, starting with emission of the illumination pulse from the target are:

1. The *receive mode*: For a target located at $\mathbf{x}_0$, the observed (illumination) signal is the convolution

$$h_i^{ae}(t) \otimes h_i(\mathbf{x}_0, t). \tag{4.4}$$

The emission from the illuminated target is sampled by the TRM over a time interval T, which we expect to contain the desired signal information. The time-reversed signal is thus

$$h_i^{ae}(T - t) \otimes h_i(\mathbf{x}_0, T - t). \tag{4.5}$$

2. The *transmit mode*: The time-reversed signals must now be retransmitted by the array, requiring convolution through $h_i^{ea}(t)$ and propagation to the target through $h_i(\mathbf{x}_0, t)$,

$$h_i^{ae}(T - t) \otimes h_i(\mathbf{x}_0, T - t) \otimes h_i^{ea}(t) \otimes h_i(\mathbf{x}_0, t). \tag{4.6}$$

The maximum response is obtained at time $t = T$, and if $h_i^{ea}(t) = h_i^{ae}(t)$, which is a reasonable assumption for high-quality transducers. The reason is that the maximum output of a linear system having impulse response $h(t)$ is achieved when the input is of the form $h(-t)$. Such a response is calculated from the convolution $h(t) \otimes h(-t)$, and is an even function with a maximum at $t = 0$.

The total field due to the array is then the sum over the elements,

$$\sum_i h_i^{ae}(T - t) \otimes h_i(\mathbf{x}_0, T - t) \otimes h_i^{ea}(t) \otimes h_i(\mathbf{x}_0, t). \tag{4.7}$$

The elements achieve constructive interference at $\mathbf{x} = \mathbf{x}_0$ and $t = T$, resulting in a strong focal spot field akin to that due to geometrical focusing.

4.2 Time Reversal Array (TRA) Debilitating Factors

One goal of the present study was to examine the feasibility of using TRAs in a shallow water environment to focus acoustic energy onto waterborne mines for possible

neutralization by acoustic pressure. Due to the resolution and dynamic range limitations of current systems, uncertainties in amplitude, time-domain waveform, and phase will result. This will cause a general degradation of the performance of the phased array system. An effective mine countermeasure (MCM) system will certainly require going to such high intensities that nonlinear properties of the transduction devices and the propagation medium will become important. The effect of finite-amplitude propagation on the performance of a TRA and the effect of absorption in the propagation medium are also studied as debilitating effects on TRA focusing. These debilitating effects will be studied in the remainder of this chapter.

4.3 TRA Initial Phase Error Effect

Error in the initial time delay for TRA elements is the first debilitating factor we will examine in this chapter. This can be expected to be one of the most important debilitating factors which degrade the performance of a TRA system. Since the TRA is a phased array, the integrity of the temporal or phase information is crucial to its operation. The most important phase data is that which determines the initial arrival times of the pulses from the array elements at the location of a target. This feature is shared with ordinary phased arrays or time-delay focusing, which relies on time of flight of the pulses to form a focus by superposition at the target location. Other phase effects would involve the phase information for the pulses emitted by each TRA channel following initial activation, this would determine the focusing quality due to multipaths, multiple scattering, and phase aberration correction from medium refraction index inhomogeneities.

4.3.1 Signal Phase Error

Error in the signal initial phase was modeled by introducing random stochastic jitter into the time-domain signals that the array elements record during the receive mode.

The jitter can result from limited-resolution data acquisition electronics in the receive and/or transmit modes. The jitter is calculated for each array element individually as a time delay in the *initial* phase of each signal. Because the present study seeks to define a starting point for evaluating the relative effects of the more important parameters described that reduce the effectiveness of the time reversal array, only the simplest cases are studied. For example, one could have introduced jitter into each cycle of the wavetrains, or into each time step. In addition, amplitude jitter could be included. The simulations in this study only introduce jitter into the initial phase information of the pulses because the latter effects should be investigated in the category of pulse shape uncertainties, which is not addressed here.

The jitter is given in terms of a fraction of the narrow-band signal's period. For a time-domain signal at array element k of the form $p_k(t)$, we introduce a time delay, δt_k, so that

$$p_k(t) \rightarrow p_k(t + \delta t_k). \tag{4.8}$$

The base source waveform is a sinusoidal envelope. The uncertainty is introduced for each of the elements independently, padding the leading (jitter) time, δt, with zeros. The jitter's duration is computed randomly for the kth element from the narrow-band period, τ_0, the maximum error, A, as a fraction of 2π of the base wavelength for a run, and a random multiplier, σ_k,

$$\delta t_k = \sigma_k A \tau_0. \tag{4.9}$$

The random variable, σ_k, can range from zero to unity, and is different for each element, but the maximum possible jitter for any array element is A for a given simulation. Of course, the jitter can be defined in other ways, and could be thought of as being due to two processes: one during the receive mode, and the other during the transmit mode of the array.

4.3.2   TRA Simulations in a Shallow Water Channel

A vertical, 64-element, equally-spaced linear array with an aperture of 25.6 m is located in the center of a shallow water channel. A 2 kHz narrow-band point source is located 51.2 m away from the array, shown in Figure 4.2.
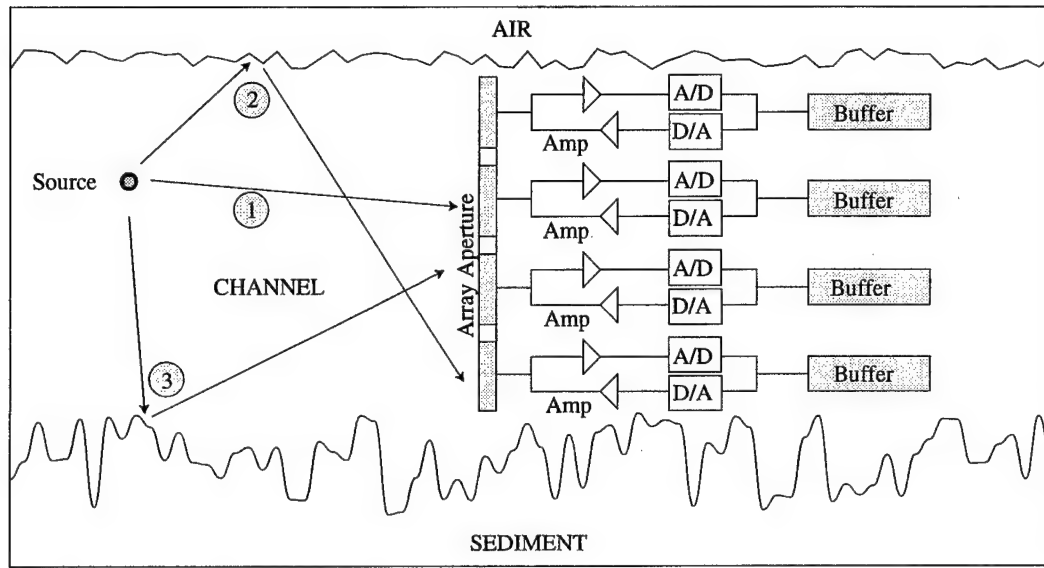
Figure 4.2: Diagram of the layout of the channel and time reversal system simulated in this study. The block diagram of the time reversal system is after Jackson and Dowling [48].

The Solution Method

The linear inhomogeneous acoustic wave equation was used for the simulations presented in this section,

$$\nabla \cdot \left(\frac{\nabla p}{\rho} \right) - \frac{1}{\rho c^2} \frac{\partial^2 p}{\partial t^2} = 0, \tag{4.10}$$

with the primary variable being the acoustic pressure, $p(\mathbf{r}, t)$.

The wave equation is solved in the time domain using a two-dimensional second-order accurate (in space and time) finite-difference time-domain (FDTD) code. The

calculations are carried out on a rectangular grid space of dimensions 1024 horizontal by 512 vertical mesh points. Absorbing boundary conditions were used at the extreme upper and lower edges of the computational domain to simulate an extended spatial region for visual clarity, although this is not necessary, as the time reversal method is valid in situations where multiple paths and scattering exist.

The Propagation Medium
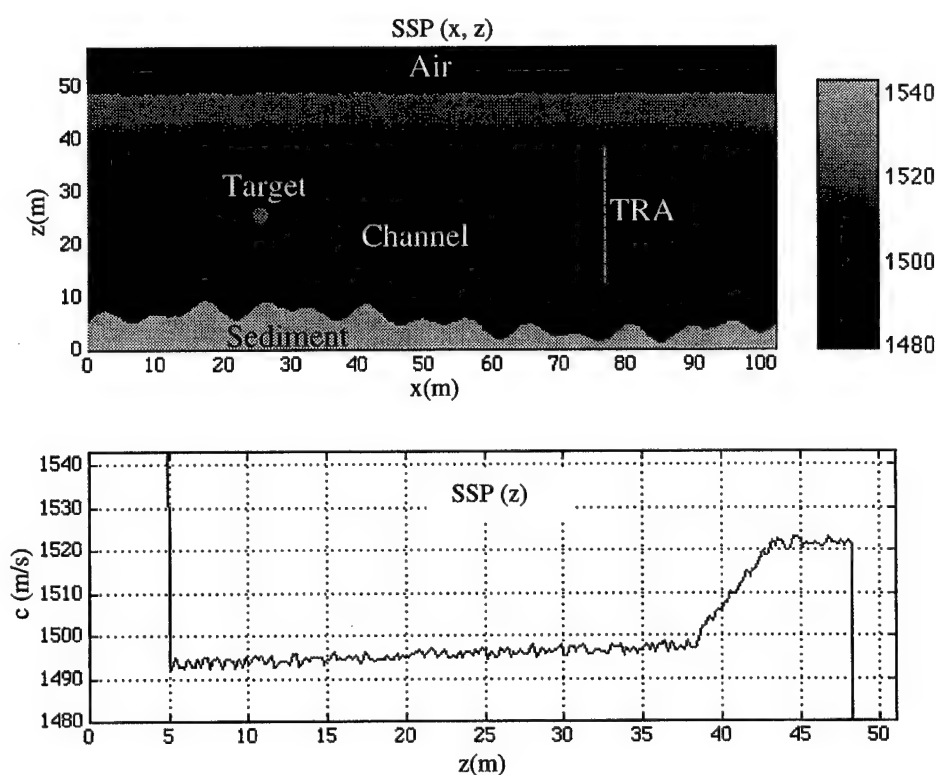
Figure 4.3: The sound speed profile used in the simulations. The extreme values for sediment and air are truncated to better illustrate the profile in water.

The wave equation (4.10) is solved in an inhomogeneous medium modeled as air above a water channel approximately 50 m deep with a (fast) fluid sediment below it.

The sound speed profile (SSP) is fashioned after data given in [25] and [1]. A graphical representation of the SSP is shown in Figure 4.3. Although the basic SSP profile is similar to that used in many studies, it serves to illustrate the physical concepts only, and is not meant to be an accurate oceanographic representation of the SSP of any actual body of water. The properties used for 20°C air were a homogeneous sound speed of 343 m/s and a density of 1.2 kg/m^3. The sound speed in the water channel was a function of depth below the surface, with inhomogeneities added to that profile. The sediment also had inhomogeneities built on top of an average sound speed of 1650 m/s, and an average density of 1860 kg/m^3. Spectral statistics of the channel properties were not considered for the present study. The density field was obtained in a similar manner to complement the SSP. Inhomogeneities in the water and sediment are in the form of small fluctuating regions of excess sound speed and density. Figure 4.3 gives an idea of the roughness of this scale and its magnitude. Furthermore, a fine random component is added to the sound speed and density to give some fine structure.

The shapes of the air-water and water-sediment interfaces are composed of combinations of sinusoids with small, local, random fluctuations. Again, the intention is to provide simulations in a non-uniform medium with rough interfaces and not to model any oceanographic spectra at this time.

4.3.3 Results for TRA in shallow water channel simulations

The results of the simulations confirm that the time reversal method successfully focuses linear acoustic waves onto a target in an lossless inhomogeneous medium with multipath effects and rough boundaries. Two snapshots are shown for the reference (ideal) case run. Figure 4.4 shows the pressure field during the receive mode of the array in the top panel, and the instant of maximum focus onto the source during the transmit mode of the array in the lower panel.
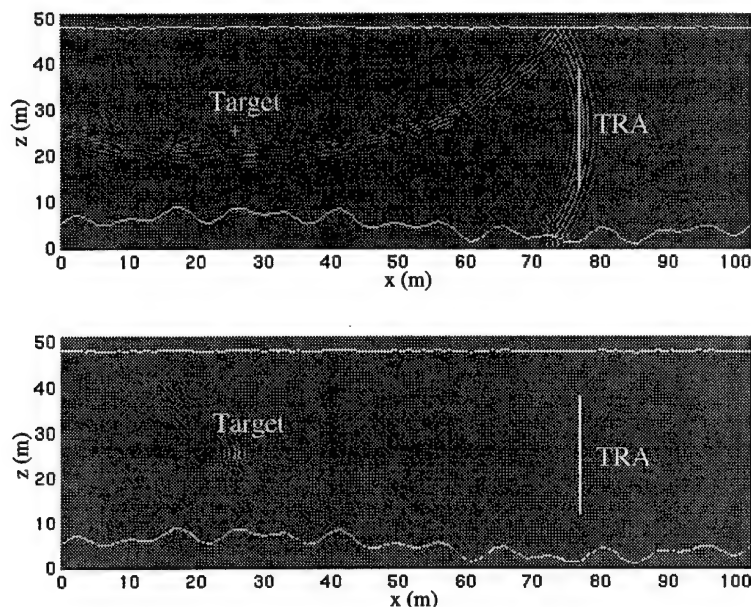
Figure 4.4: The acoustic pressure field. The top frame shows the pressure some time after leaving the source during the array's receive mode operation. The lower frame shows the pressure after the array's transmit mode, when the maximum pressure occurs at the source location.

Description of TRA Phase Jitter

Random time-domain jitter is introduced in the form of zero padding leading the initial phase signal from each array element. Figure 4.5 shows the pressure field in dB around the location of the source at the instant of maximum focusing. The values are referenced to the maximum pressure (at the source's location usually). It was found that the location of the focus maximum remained near the original location of the source. The reason is that for many-element arrays the focal shift would tend to average out to its original value because the error has a zero mean. On the other hand, significant degradation in focus quality was observed for jitter exceeding about one-tenth of a wave period. As expected, the initial phases of the waveforms were shown

to be very important to the focusing ability of the array. Simulations were conducted with jitter that ranged from 10%(2π) up to a full 2π of a period. The -3 dB points did not show any appreciable spreading from case to case, but the magnitude of the acoustic pressure for the cases with large jitter was far reduced and spread over a large region of the channel, resulting in significant focusing degradation for jitters greater than 10% to 20% of one period (see Figure 4.5). This result was published in [41] and is confirmed for line arrays in general by Von Ramm and Smith [62], who state that a maximum phase error equating to $\lambda/8$ is tolerable for arrays with at least 16 elements. Wang *et al.* [70] also find that for a two-dimensional hyperthermia applicator a phase error equivalent to $\lambda/6$ is tolerable. In the studies cited above, the authors find that an acceptable focus was maintained for random phase errors up to 15 to 20% of a wavelength.

The surface and bottom reflections can act as virtual sources to enlarge the effective aperture of the time reversal array [5]. Further, the inhomogeneities and the multipath reflections can act to enlarge the effective aperture of the array. The latter phenomenon has been recognized by Dowling and Jackson, who refer to it as "superfocusing" in [22]. The localized differences in the index of refraction act as distributed sources which are present throughout the medium. The focal zone's full width at half maximum (FWHM) spot size in free-space is given by the diffraction limit as

$$w = 1.2 \, \lambda z/a, \tag{4.11}$$

the width is proportional to the range, z, and inversely proportional to the aperture, a. In our case the FWHM would be approximately 1.8 m in free-space. We observe that the FWHM points in the channel occur at $\pm$ 0.3 m from the source location, and attribute this result to the virtual array due to the multipath propagation and the superfocusing described above.
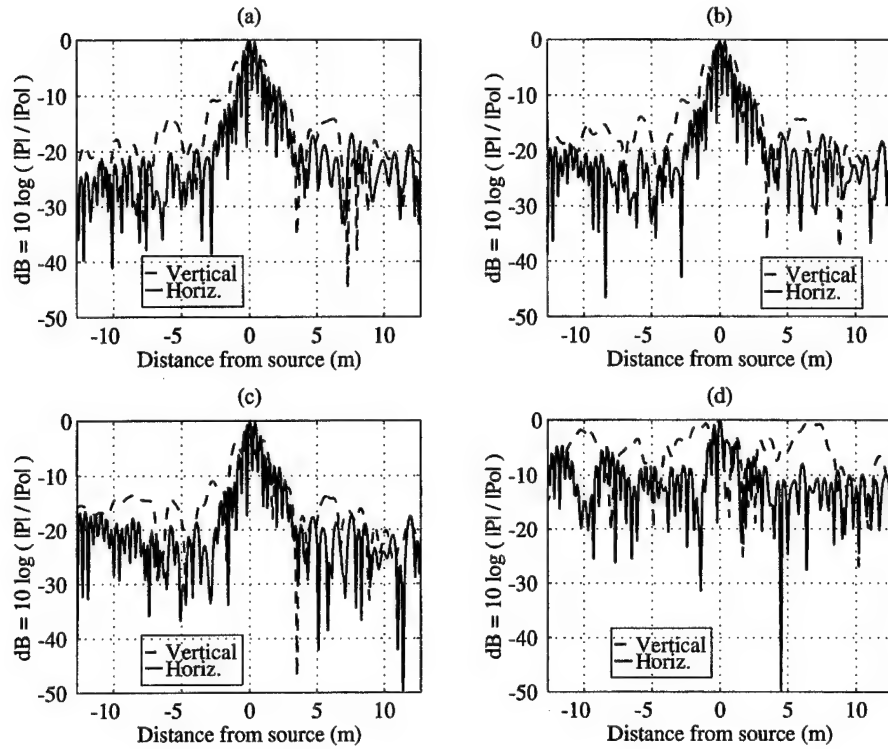
Figure 4.5: Slices through the source position at the time of maximum focusing for various jitter conditions. The dashed lines denote the vertical slices (parallel to the array), while the solid lines denote the horizontal slices (perpendicular to the array). Panels are for (a) No jitter (reference case), (b) Max. jitter $10\%(2\pi)$, (c) Max. jitter $20\%(2\pi)$, (d) Max. jitter $= 100\%(2\pi)$.

4.3.4 Phase Jitter Simulation Conclusions

The premise of using phase conjugate arrays for the focusing of intense acoustic fields onto a remote waterborne target has implications for MCM system design. The possibility of remote neutralization of pressure-sensitive mines would be an asset to the MCM arsenals that exist today [31]. The concept has been demonstrated in theory and in the laboratory for ultrasonic frequencies in medical applications. Ocean field experiments in shallow water have been conducted recently by Kuperman *et al.* [52]. These experiments were conducted at 400 Hz, and would not encounter the

difficulty with electronic jitter that high frequency arrays would suffer. However, the results obtained so far from experimental [18] and theoretical [22] groups show a remarkable robustness when using the time reversal technique with multiple scattering and reflection in random media.

We used linear acoustics to model sound propagation through a shallow water channel with an inhomogeneous sound speed profile as well as a rough surface and bottom. The results for cases that are expected to degrade the focusing ability of a time reversal array by altering the initial phase information are given. Initial phase timing is corrupted by some jitter in the time-domain signals, which affect the relative phases of the transmitted array element waveforms.

The array's focusing appears to hold up well under these circumstances for jitter up to 10% to 20% of the narrow-band period. Jitter greater than about 20% of a period results in significant loss of focal pressure. These results are confirmed by other studies of linear phase quantization errors [62, 70]. The location of maximum pressure remained at the location of the source because the jitter is a zero-mean random variable, indicating that initial phase of the returned signals is more important than the details of the waveform phase shape. This is encouraging, since the data aquisition of a broadband time-reversal signal, and the translation of that signal into a corresponding high-intensity array pressure output is unlikely with current technology. This is especially true if the array consists of elements whose bandwidth is significantly greater than PZT transducers.

Other factors not presented thus far which are detrimental to the focusing of phase conjugate arrays are the nonlinear behavior of the medium and the transducer and electronics' transfer functions. The nonlinearity of the propagation process plays an important role in conjunction with absorption that will be studied in Section 4.5, and casts serious doubt on the feasibility of using time reversal systems for real MCM applications.

4.4 The Effect of Absorption on TRA's

In this section the linear absorption of the propagation medium will be examined as a debilitating factor on the performance of a focusing TRA. The motivation for including absorption as a debilitating factor is that some applications for TRA focusing may be carried out in media where, unlike water, the absorption coefficient may significantly affect the propagating waves.

One example of absorbing media is biological tissue. This section presents an example of a TRA in a coupling water bath used to focus acoustic energy onto a target inside a modeled human head. The transcranial focusing experiences a drastic effect on time reversal when crossing the highly-absorbing bone layer of the skull.

4.4.1 Violation of Time Reversal Invariance by Absorption

We use a linear version of the model wave equation (2.21), derived in Chapter 2,

$$\nabla^2 p - \frac{1}{c_0^2}\frac{\partial^2 p}{\partial t^2} - \frac{1}{\rho_0}\nabla p \cdot \nabla \rho_0 + \frac{2\alpha}{c_0\omega^2}\frac{\partial^3 p}{\partial t^3} = 0, \qquad (4.12)$$

where the absorption term is written in terms of the absorption coefficient, α, related to the acoustic diffusivity δ by

$$\alpha = \frac{\delta\omega^2}{2c^3}. \qquad (4.13)$$

If we consider the left hand side (LHS) of (4.12) as a linear differential operator, $\mathcal{L}$, acting on the acoustic pressure, we can write (4.12) as

$$\mathcal{L}p \equiv \mathrm{LHS}(4.12) = 0. \qquad (4.14)$$

We can test whether the differential operator, $\mathcal{L}$, is time-reversible by examining its effect on the forward time solution and its backward time counterpart. If $p = \phi(\mathbf{x}, t)$ is a forward time solution of (4.12), that is, $\phi(\mathbf{x}, t)$ satisfies

$$\mathcal{L}\phi(\mathbf{x}, t) = 0, \qquad (4.15)$$

then by direct calculation we can test whether $q(\mathbf{x}, t) \equiv \phi(\mathbf{x}, -t)$ is a solution of the wave equation as well. If so, then (4.12) is time reversal invariant, *i.e.*, it holds under time reversal.

Since for $\tau \equiv -t$, the partial derivative $\partial \tau / \partial t = -1$, upon making the transformation $t \to \tau$, the time derivatives of p are

$$\frac{\partial^n p(\mathbf{x}, -t)}{\partial t^n} = \frac{\partial^n p(\mathbf{x}, \tau)}{\partial \tau^n} \left(\frac{\partial \tau}{\partial t} \right)^n = (-1)^n \frac{\partial^n p(\mathbf{x}, \tau)}{\partial \tau^n}. \qquad (4.16)$$

That the odd-ordered partial derivatives with respect to time undergo a sign change is significant in our discussion. This simple fact is correctly cited for holding the key to the time-reversibility of the lossless acoustic wave equation, and has been noted by Fink [27].

Now we substitute for $p(\mathbf{x}, t)$ its time-reversed companion solution, $q(\mathbf{x}, t)$, into (4.12) and use (4.16) to obtain

$$\mathcal{L}q = \left[\left(\nabla^2 - \frac{1}{c^2} \frac{\partial^2}{\partial t^2} \right) \phi - \frac{\nabla \rho_0}{\rho_0} \cdot \nabla \phi - \frac{\delta}{c^4} \left(\frac{\partial^3 \phi}{\partial t^3} \right) \right]\Bigg|_{(\mathbf{x}, -t)}, \qquad (4.17)$$

from which,

$$\mathcal{L}q = \mathcal{L}\phi - \frac{2\delta}{c^4} \frac{\partial^3 \phi}{\partial t^3}. \qquad (4.18)$$

Thus we conclude that $q(\mathbf{x}, t) \equiv \phi(\mathbf{x}, -t)$ is not a solution of (4.12) in the presence of absorption. Physically speaking, this says that the linear wave equation (4.12) is not time reversible due to the presence of the absorption term.

4.4.2 Example of TRA in an Absorbing Medium

We use a numerical example to illustrate the detrimental effects absorption has on time reversal focusing systems. Figure 4.6 shows the scenario presented in this example, which involves a two-dimensional simulation of the acoustic field due to a line array operated as a TRA in a water coupling bath to insonate a scatterer in the human brain. A scatterer is positioned at some location within a cross-section of a human
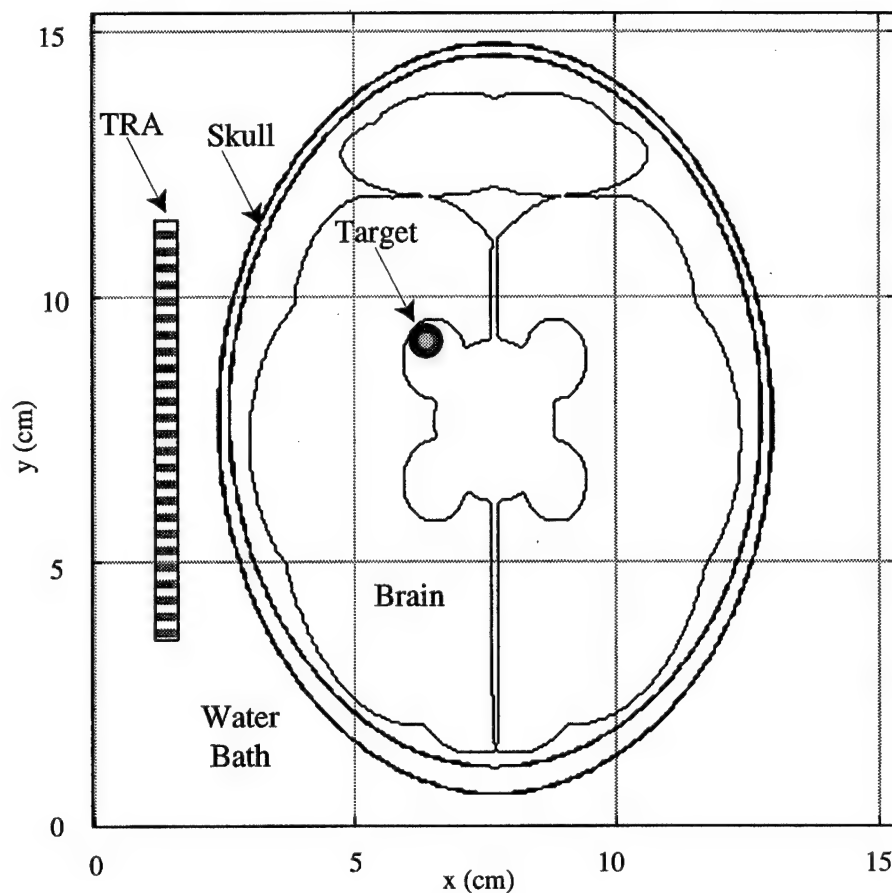
Figure 4.6: Diagram of the propagation model, showing the position of the linear array to the left of the head, and the point scattering target within the brain.

head containing various inhomogeneous organs, and most importantly, a bone skull layer. The propagation properties for the organs and the skull bone were obtained from the literature [77, 55, 30]. Ellipses were used to generate the geometrical layout of the head cross-section, in a fashion similar to that used to generate tomographic phantoms [49, 55]. Twenty-three ellipses were used to construct the 2-D phantom in Figure 4.6. A line array of 64 elements were simulated to lie in the water about 1 cm from the head. Simulations of TRA focusing with and without absorption were performed and the results on the focal pressure amplitude were compared.

A second-order FDTD solution for the acoustic pressure was solved on the 2-D computational domain to simulate an illuminated point scatterer emitting a pulse while the array collected data in the receive mode. This step was followed by transmittal of unamplified time-reversed signals from the array elements, which will focused onto the target. Due to the limited aperture provided by the array, not all the illumination pulse energy was captured by the array. Hence, the time-reversed focus amplitude was only a fraction of the original amplitude, even in the lossless case. Figure 4.7 shows the time traces of the acoustic pressure as measured at the 64 array
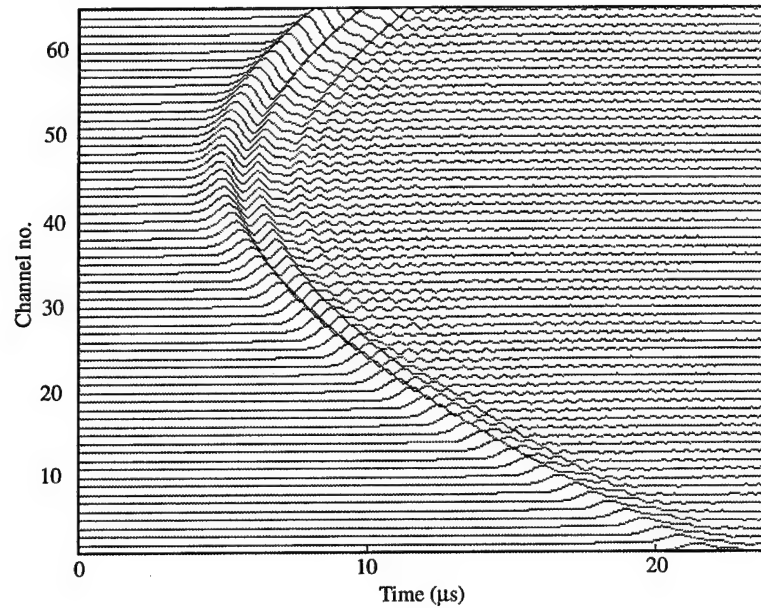
Figure 4.7: Time traces measured by each of the 64 TRA elements during the receive phase of the time reversal operation.

elements. To lowest order, the initial delay time was due to time-of-flight time representing the distance separating the array element and the illuminated target point. These were the signals which will be time reversed by the TRA during the transmit

phase of the process.

Figure 4.8 shows the acoustic pressure along the x and the y axes taken through the target location at the instant of maximum focusing. The waveform emitted by
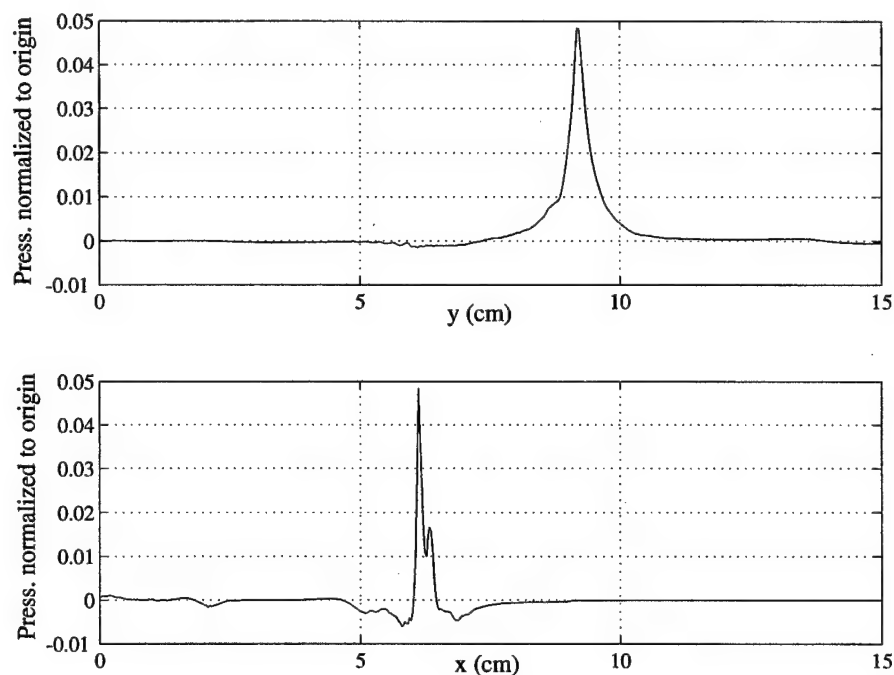
Figure 4.8: Spatial slices of the pressure field along the x and the y axes passing through the target at the instant of maximum focusing.

the target and the waveform returned to the target should be the same, except scaled in amplitude and time-reversed. Figure 4.9 shows the original pulse sent out by the scatterer during the receive mode in (a), and the time trace at the target location upon time reversal focusing from the transmit phase (b). Note that some of the high-frequency features have been lost in the two-way propagation. This is because the pulse used as the illumination signal was obtained from laboratory measurements with broadband instruments of a shock wave generated by a spark lithotripter source, and the absorption in the fluid acted as a low-pass filter. For the case where thermoviscous
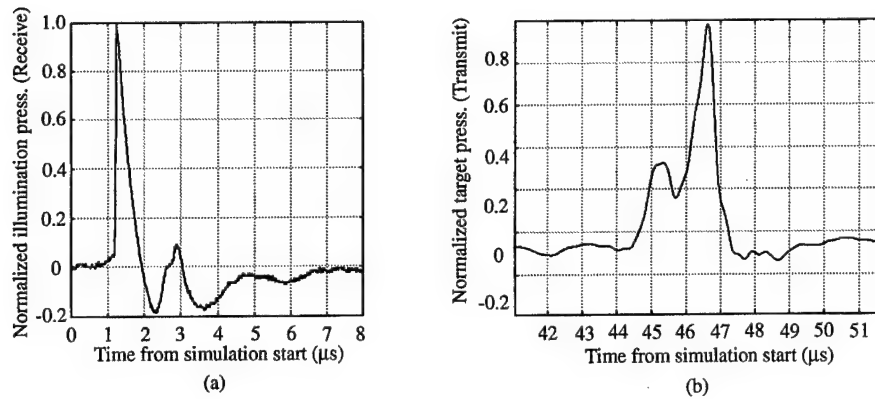
Figure 4.9: Original pressure pulse as sent out by the scatterer (a), and the pulse as measured at the target upon time reversal (b) for the case with absorption.

absorption was included, the focal amplitude was reduced due to linear absorption due to thermal and viscous losses, as explained in Chapter 2, and time reversal invariance violation, as explained in the previous section. Figure 4.10 shows a comparison of peak pressure at the target location at the time of maximum focusing. The spatial slices through the target location at the instant of maximum acoustic focusing pressure show that the lossless case provided a much higher amplitude at the focus. In our case the peak pressure at the focus for the lossless case was 2.2% of the original pressure of the scatterer pulse. When absorption was taken into account the pressure at the focus dropped to 1.3% of the maximum pulse pressure. This reduction in focal pressure by about one half was due to the two effects mentioned in the previous paragraph. The reduction in focal pressure is not due to propagation impediments such as enhanced acoustic impedance mismatch for example. The same sound speeds and densities are used for both lossless and lossy simulations. The severe inhomogeneity (the skull layer) was responsible for the fact that focal pressure was so low compared to a case where no absorption would occur. For this reason a section of skull bone is normally removed surgically from the array aperture prior to insonation of the brain in animal
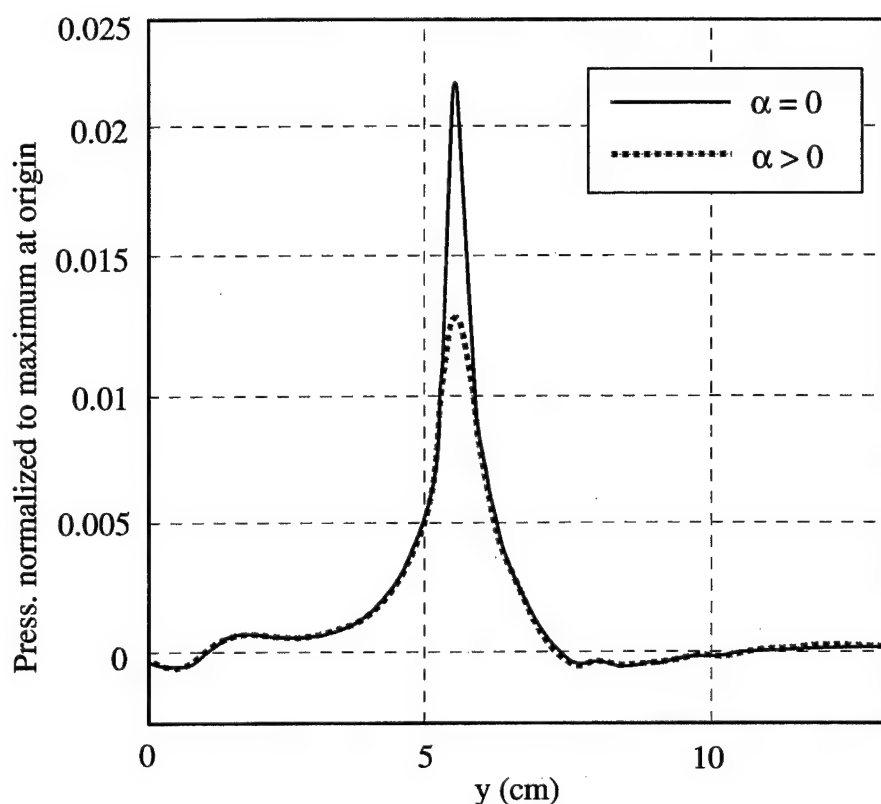
Figure 4.10: Acoustic pressure at the focus at the instant of maximum focusing, showing the lossless case achieving almost twice the peak pressure as the lossy case.

experiments. Otherwise the large absorption in the skull bone would cause excessive heating near the skull. This aspect of biomedical acoustics will be discussed in detail in Chapter 5, which deals with hyperthermia applications.

Finally, we present snapshots of the acoustic pressure for both the lossless and the lossy simulations. Figure 4.11 shows one snapshot of the pressure field during the receive mode of the TRA operation, where (a) is the lossless case and (b) is the lossy case. Then a pair of frames are taken from the transmit stage of the TRA operation at the instant of maximum focusing. Frame (c) is the field for the lossless simulation, and frame (d) is the field at the same time for the lossy simulation. While the gray
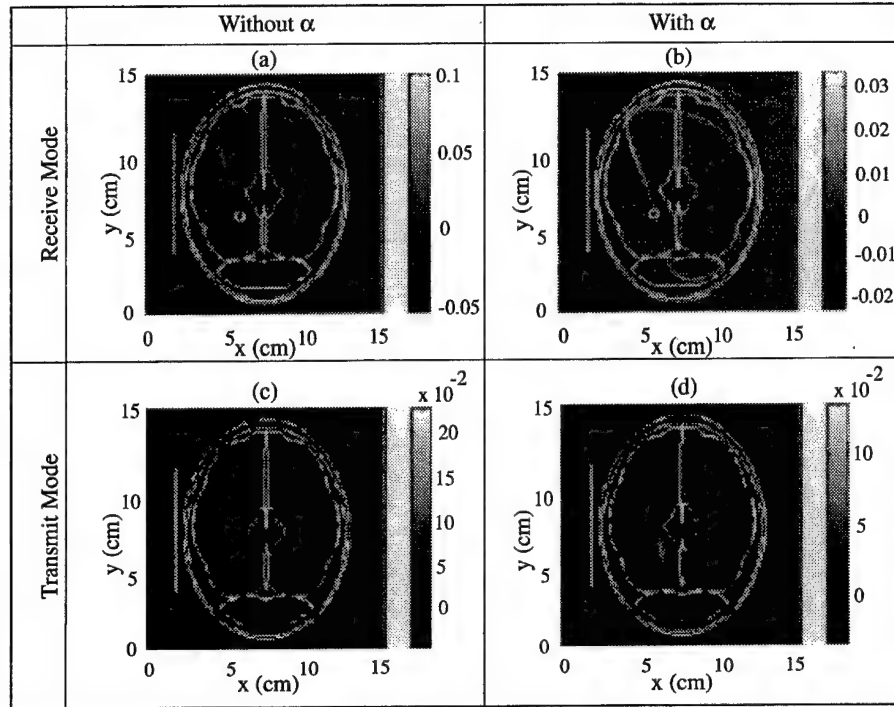
Figure 4.11: Snapshots of the acoustic pressure during the receive mode (a) and (b) and the transmit mode at focusing (c) and (d). The frames on the left (a) and (c) are for the lossless simulation, while the frames on the right (b) and (d) are for the lossy simulation.

scale was fully utilized in each of the four frames, the scales to the side show that the peak pressure for the lossy case was about one half of that of the lossless case. Also it can be seen from the transmit mode frames and from Figure 4.10 that the full-width-at-half-maximum (FWHM) for the lossy case is increased. In this example, the FWHM went from 4 mm for the lossless case to 9 mm for the lossy case.

We have seen how absorption can degrade the focusing ability of a TRA. It might seem that one solution to partially overcome this debilitating effect is to amplify the signal at the array. However, if the amplification is such that the signal is of finite amplitude we encounter further debilitating effects due to nonlinearity, which will be discussed in the next section.

4.5   The Effect of Nonlinearity on TRA's

Nonlinear propagation in absorbing sound channels is proposed as a debilitating factor to time reversal array system performance. Since we have seen the detrimental effect of linear absorption on TRA's in the previous section, we investigate the combined role of absorption and nonlinearity in this section. Here we ask the question: what extra role if any does nonlinear propagation of finite-amplitude sound play in degrading the time reversal invariance of a TRA?

4.5.1   Background for Nonlinear TRA Analysis

We now look at the effect of finite-amplitude (nonlinear) propagation on time reversal systems operated in lossless and in lossy media. A finite-amplitude sound wave distorts as it propagates through the medium. The distortion is manifested as a transfer of energy from the originial frequency spectrum into higher harmonics. Because most media exhibit absorption that increases with frequency, one might expect that nonlinear distortion would lead to greater absorption, and hence worse time reversal. Muir *et al.* [59] conducted an experiment where a finite-amplitude sinusoidal pulse was propagated through water and then reflected off of a pressure-release surface. For their pulse the pressure-release surface caused an amplitude multiplication by -1, which for a sinusoidal signal is similar to introducing a 180° phase shift. They found that the pulse undistorted after reflection, which suggests that time reversal invariance may hold in the presence of nonlinear distortion. In other words, while it was not a time reversal operation, the experiment showed that nonlinear distortion effects could be undone.

The setup for the problem under study is as follows: a source emits a plane wave acoustic pulse which propagates to a time reversing array of two elements, positioned on either side of the source. The acoustic field recorded by the array is time reversed, and then retransmitted. This simple setup is suitable for studying the effects of

nonlinear distortion of an acoustic field. Of particular interest is the debilitating effect that nonlinearity may have on a time reversal system's ability to form an intense focus near the original source. This is of practical interest to those wishing to use time reversal systems to achieve high-intensity acoustic fields at a target, such as in the destruction of kidney stones by lithotripsy [67], the ablation of tumors in tissue [66], or the remote neutralization of mines at sea [41].

Two scenarios were studied: first, a finite-amplitude pulse was emitted from a source and propagated outward to the time reversal array (the receive stage of the time reversal operation). The signal was then time reversed and retransmitted from the array elements (the transmit stage of the time reversal operation). We label this scenario the nonlinear-nonlinear case because the traveling pulse had finite amplitude during both the receive and the transmit stages of time reversal, and hence, undergoes nonlinear effects during both stages of the process. The second scenario considered was where the source emitted a low-amplitude pulse, which propagated without appreciable nonlinear steepening to the array during the receive mode, followed by amplification of the time-reversed signal at the array during the transmit mode. The amplification for the transmit mode propagation led to nonlinear distortion of the pulse. This case is referred to as the linear-nonlinear scenario in our study.

4.5.2 The Nonlinear Absorbing Wave Equation

The model equation used in this study for propagation of finite-amplitude acoustic pressure pulses, $p(\mathbf{x}, t)$, in a thermoviscous medium was derived in Chapter 2,

$$\left(\nabla^2 - \frac{1}{c_0^2}\frac{\partial^2}{\partial t^2}\right)p - \frac{\nabla \rho_0}{\rho_0} \cdot \nabla p + \frac{\delta}{c_0^4}\frac{\partial^3 p}{\partial t^3} + \frac{\beta}{\rho_0 c_0^4}\frac{\partial^2 p^2}{\partial t^2} = 0. \qquad (4.19)$$

The last term on the left hand side of (4.19) is the nonlinear term, discussed in Chapter 2.

The most salient features of pulse propagation in an absorbing nonlinear medium
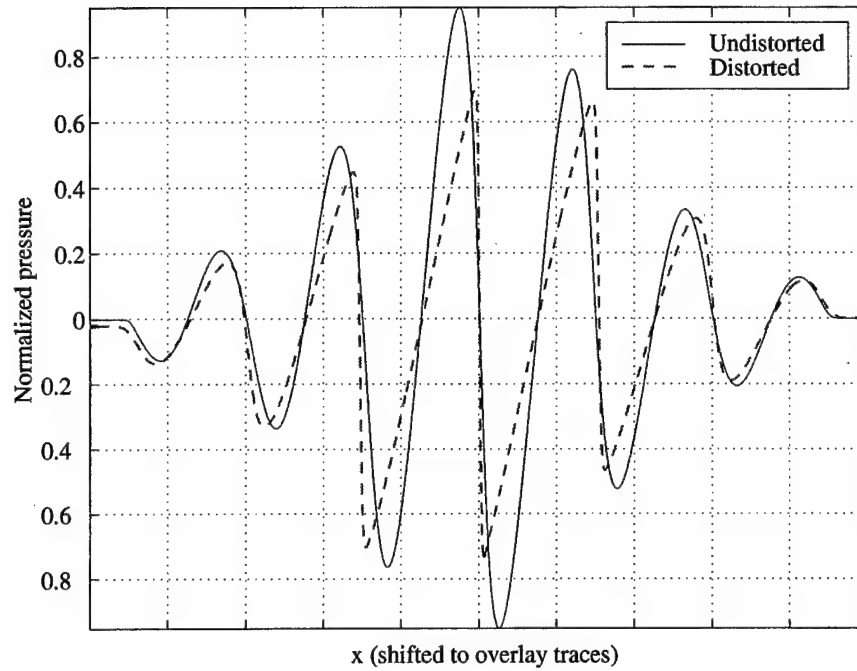
Figure 4.12: Comparison of the pulse used in the present study as emitted from the source (solid line) and as observed some time later (dashed line). The pulse steepens due to nonlinearity and decays due to absorption.

are the amplitude reduction due to absorption and the waveform distortion, or shocking, due to the nonlinearity. An example of the pulse used in this study before and after propagating some distance in an absorbing nonlinear medium is shown in Fig. 4.12.

4.5.3 The Conditions for Time Reversal Invariance

Following the method used in the section 4.4, we now consider the left hand side (LHS) of (4.19) as a nonlinear differential operator, $\mathcal{D}$, acting on the acoustic pressure, and

write (4.19) as

$$\mathcal{D}p \equiv \text{LHS}(4.19) = 0. \tag{4.20}$$

If $p = \phi(\mathbf{x}, t)$ is a forward time solution of (4.19), that is, $\phi(\mathbf{x}, t)$ satisfies

$$\mathcal{D}\phi(\mathbf{x}, t) = 0, \tag{4.21}$$

then we can test whether $q(\mathbf{x}, t) \equiv \phi(\mathbf{x}, -t)$ is a solution of the wave equation. If so, then (4.19) is time reversal invariant, *i.e.*, it holds under time reversal. We can expect the absorption term to lead to time reversal invariance violation, as was found in Section 4.4, but we will also uncover effects due to nonlinearity.

Substituting for $p(\mathbf{x}, t)$ its time-reversed companion solution, $q(\mathbf{x}, t)$, into (4.19) we obtain

$$\mathcal{D}q = \left[\left(\nabla^2 - \frac{1}{c^2} \frac{\partial^2}{\partial t^2} \right) \phi - \frac{\nabla \rho}{\rho} \cdot \nabla \phi - \frac{\delta}{c^4} \left(\frac{\partial^3 \phi}{\partial t^3} \right) + \frac{\beta}{\rho c^4} \frac{\partial^2 \phi^2}{\partial t^2} \right] \Big|_{(\mathbf{x}, -t)}, \tag{4.22}$$

from which,

$$\mathcal{D}q = \mathcal{D}\phi - \frac{2\delta}{c^4} \frac{\partial^3 \phi}{\partial t^3}. \tag{4.23}$$

Thus we conclude for the nonlinear absorbing wave equation that $q(\mathbf{x}, t) \equiv \phi(\mathbf{x}, -t)$ is not a solution of (4.19) in the presence of absorption, as for the linear absorbing wave equation.

Mathematically, the result indicates that the nonlinear term itself is *not* responsible for time reversal violation. However, as stated earlier, real nonlinear wave propagation is always accompanied by absorption in the medium. The result is an irreversibility of nonlinear acoustics. Therefore, for finite-amplitude propagation we would expect a degradation of the performance of a time reversal system. The above discussion applies to our first test scenario for this study, the nonlinear-nonlinear case.

Now we modify the analysis for the second scenario under study, the linear-nonlinear case. If the acoustic pressure received is not only time reversed, but amplified, then the correct test for time reversal invariance checks $\mathcal{D}$ for the case where

$q(\mathbf{x}, t) \equiv a\phi(\mathbf{x}, -t)$, where a is a constant real amplification factor. In this case $a\phi$ is substituted for ϕ in (4.22),

$$
\begin{aligned}
\mathcal{D}q &= \left.\left[\left(\nabla^2 - \frac{1}{c^2}\frac{\partial^2}{\partial t^2}\right)a\phi - \frac{\nabla\rho}{\rho}\cdot\nabla a\phi - \frac{\delta}{c^4}\left(\frac{\partial^3 a\phi}{\partial t^3}\right) + \frac{\beta}{\rho c^4}\frac{\partial^2 (a\phi)^2}{\partial t^2}\right]\right|_{(\mathbf{x},-t)} \quad (4.24)\\
&= a\left[\mathcal{D}\phi - \frac{2\delta}{c^4}\frac{\partial^3\phi}{\partial t^3} + (a-1)\frac{\beta}{\rho c^4}\frac{\partial^2\phi^2}{\partial t^2}\right]. \quad (4.25)
\end{aligned}
$$

Note that the propagation is strictly "nonlinear" in both travel directions, but the nonlinear effects are negligible during the first (receive) leg of the travel due to low amplitude. The amplitude is amplified by using $a \gg 1$ for the transmit mode of the operation.

The result above shows that when the signal undergoes amplitude amplification, time reversal invariance in a nonlinear medium no longer holds, even if the fluid is lossless. For time reversal invariance to hold for nontrivial solutions this case requires that

1. $a = 1$ or $\beta = 0$, and

2. $\delta = 0$.

The physical explanation is that aside from pure scaling of the solution, the change in signal amplitude from receive to transmit modes implies that different nonlinear distortion occurs during the two stages of the time reversal process, which will invalidate the time reversal invariance. While not strictly a violation of reciprocity, this is analogous to doing time reversal in a medium which was not steady for the duration of the two stages of the time reversal process. The receive and transmit mode propagation occur in what is essentially different filters in the channel.

4.5.4 Numerical Study of Finite-Amplitude TRA's

Numerical simulations were used to investigate the behavior of time reversal systems while controlling the absorption coefficient and the coefficient of nonlinearity in the

wave equation. The peak pressure amplitude in the receive mode (at the source) and in the transmit mode (at the array) was independently controlled also to allow for one-way or two-way finite-amplitude propagation, as desired.

4.5.5 Description of the Nonlinear TRA Simulations

The wave equation (4.19) was solved numerically for the acoustic pressure, p, using a finite-difference time-domain (FDTD) code. The finite differencing was fourth order accurate in space and second order accurate in time. The simulations were performed for a homogeneous thermoviscous fluid. Numerical considerations such as stability and numerical dispersion limited the parameter space which could be covered using the explicit FDTD method used. However, good resolution of the acoustic pressure field was possible for the range of parameters used in this study.
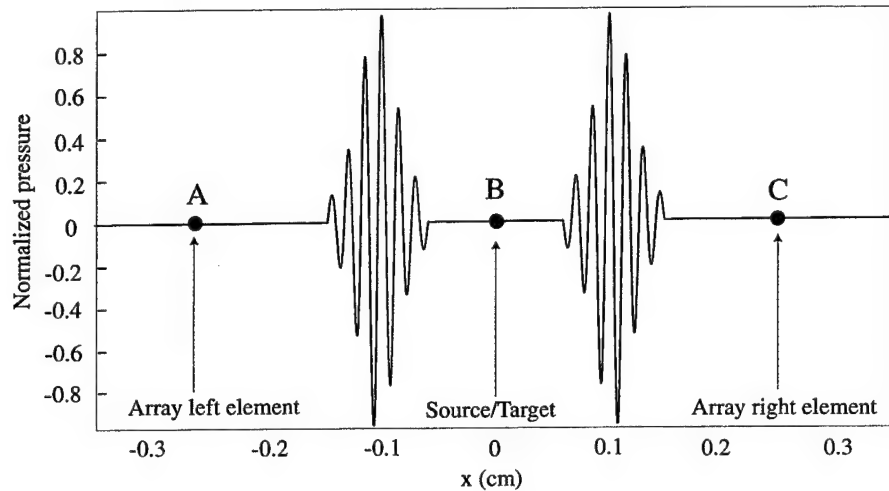
Figure 4.13: Geometry of the plane wave time reversal simulations showing a temporal snapshot in the array receive mode. The source is at location B, while the two array elements are at locations A and C.

4.5.6 Run Geometry and Parameters

The simulations were carried out in a one-dimensional coordinate system with x denoting the spatial coordinate. The source from which the source pulse was emitted is located at $x = 0$. Fig. 4.13 shows the location of the source and the elements with relation to each other. The source element (B) was driven with a sinusoidal burst, shown in Fig. 4.12, having a duration of 6 μs, a center frequency $f = 1$ MHz, and a Gaussian envelope. The driving pressure waveform applied at the source had a maximum pressure amplitude of 1 MPa for the simulations requiring nonlinear receive mode propagation, and 1 Pa for those requiring linear propagation in the receive mode (where the computational domain was much shorter than the shock formation distance).

The calculations presented in this study were for a fluid having a small signal sound speed $c = 1500$ m/s, and density $\rho = 10^3$ kg/m^3, but otherwise was not meant to represent water. The values chosen for the absorption and the nonlinearity coefficients, as well as the frequency and the peak pressure of the pulses cover a parameter space well-suited for the numerical method used in the study. Effects such as absorption and nonlinearity are cumulative, and will manifest themselves in the waveforms over some distance and time. In this study, we attempted to demonstrate the effects under study over a span of 50 wavelengths using full wave simulations suitable for detailed study of the pulses in space and time. The values of α and β are not those of any specific fluids, and are chosen to have an effect on the propagation over the distance used in the simulations. We could have alternatively used the value of peak acoustic pressure to vary the shock formation distance, for example.

In order to simplify and generalize the results some useful quantities which were discussed in Chapter 2 are repeated here for convenience. The acoustic Mach number

$$\epsilon = \frac{p_o}{\rho c^2}, \qquad (4.26)$$

where p_o is a characteristic acoustic pressure of the pulse. The shock formation

distance, x_{shock}, is the distance a sinusoidal plane wave travels before developing a shocked profile, and is defined by

$$x_{\text{shock}} = \frac{1}{\beta \epsilon k},\tag{4.27}$$

where k is the wave number given by $2\pi f/c$. Note the dependence of ϵ, and hence x_{shock}, on the peak pressure amplitude, p_o. Finally, the Gol'berg number,

$$\Gamma = \frac{\beta \epsilon}{\alpha \tilde{\lambda}},\tag{4.28}$$

is used, where $\tilde{\lambda} = 2\pi/k$.

4.5.7 Results for Finite-Amplitude TRA's

We have seen in Section 4.5.3 that the absorbing nonlinear wave equation treated as a differential operator acting on the acoustic pressure should be time-invariant when the absorption term is negligible for the nonlinear-nonlinear scenario. For the linear-nonlinear scenario, we also saw that the absorption has to be negligible, but in addition, that either the amplification at the array must be negligible ($a = 1$) or the nonlinearity coefficient must be negligible ($\beta = 0$). In this section we show the relative importance of the nonlinearity and the absorption in time reversal using the two scenarios:

1. *Nonlinear-Nonlinear time reversal*: In this scenario the source is driven with a high peak amplitude (1 MPa), resulting in nonlinear steepening occurring during the array receive mode. The detected signals at the array elements are time reversed without modification to the amplitude of the signals at the array elements. The retransmitted pulses leave the array with a significant fraction of the original source amplitude, and nonlinear effects occur during the transmit stage of the time reversal as well. The values of the absorption coefficient, α, and the nonlinearity coefficient, β, were controlled, and were the same for a given run for both the receive and the transmit stages of the time reversal operation.

2. *Linear-Nonlinear time reversal*: A low-amplitude (1 Pa) pulse was emitted from a plane source. The pulse was then captured by two array elements positioned on either side of the source. The received signals were time reversed and retransmitted from the array elements (also plane sources), but the amplitude of the retransmitted signal was amplified at the array by scaling it up to 1 MPa peak pressure. Again, various values of α and β were used to investigate the effects of time reversal in nonlinear absorbing media. For this scenario the low amplitude of the receive mode propagation ensured that the outgoing pulse propagated without undergoing nonlinear distortion, as the shock formation distance was much larger than the propagation distance. The array transmit stage, on the other hand, caused the pulse to undergo significant distortion due to the large pressure amplitude provided by the array.

4.5.8   Nonlinear-Nonlinear Time Reversal

This case may apply if either a large target is interrogated or illuminated by a high-amplitude pulse, or if a source emits a high-amplitude pulse to be time reversed. Here we expect waveform steepening during both stages of the time reversal process, as the signal will have appreciable amplitude during both the receive and the transmit modes. Note that capturing and retransmitting a shocked waveform experimentally requires broadband array elements and electronics to obtain good fidelity.

A reference simulation was run in which both the absorption and the nonlinearity were suppressed by setting $\alpha = 0$ and $\beta = 0$. This run gave data for the "ideal" time reversal case, as would be expected given our earlier analysis. The peak positive pressure obtained at the source/target location upon time reversal is denoted by p^*_{target}. In this case, the waveforms emitted by the source were fully recovered in shape and amplitude back at the source position following the time reversal operation. Note that p^*_{target} for the nonlinear-nonlinear scenario was not the same as p^*_{target} for
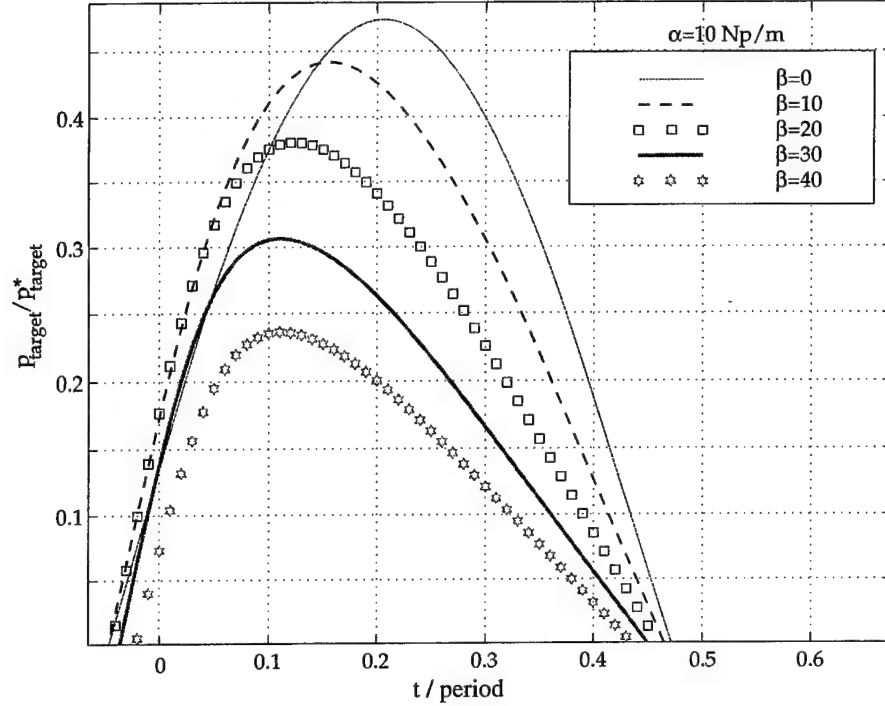
Figure 4.14: Nonlinear-nonlinear time reversal: Greatest positive half cycle of the pulse at the target, normalized to the ideal case ($\alpha = 0, \beta = 0$), for different values of β, with $\alpha = 10$ Np/m. Note that some numerical error is noticeable in the waveform for the case $\beta = 40$.

the linear-nonlinear scenario, but within each scenario, pressures were normalized to the peak target pressure for the ideal case at hand, $\alpha = 0$ and $\beta = 0$.

Fig. 4.14 shows the time trace of the largest positive half cycle at the target upon time reversal, normalized to p^*_{target}. For the case of $\alpha = 10$ Np/m, we found that the best retrofocusing, with $\beta = 0$, resulted in only 47% of p^*_{target}. When β was increased such that the source-to-array separation, $x_{src\text{-}array}$, was 1 shock formation distance, the peak target pressures achieved were about 37% of p^*_{target}. The peak target pressure decreased monotonically to about 23% of p^*_{target} for a $x_{src\text{-}array}$ of about 1.8 x_{shock}, or
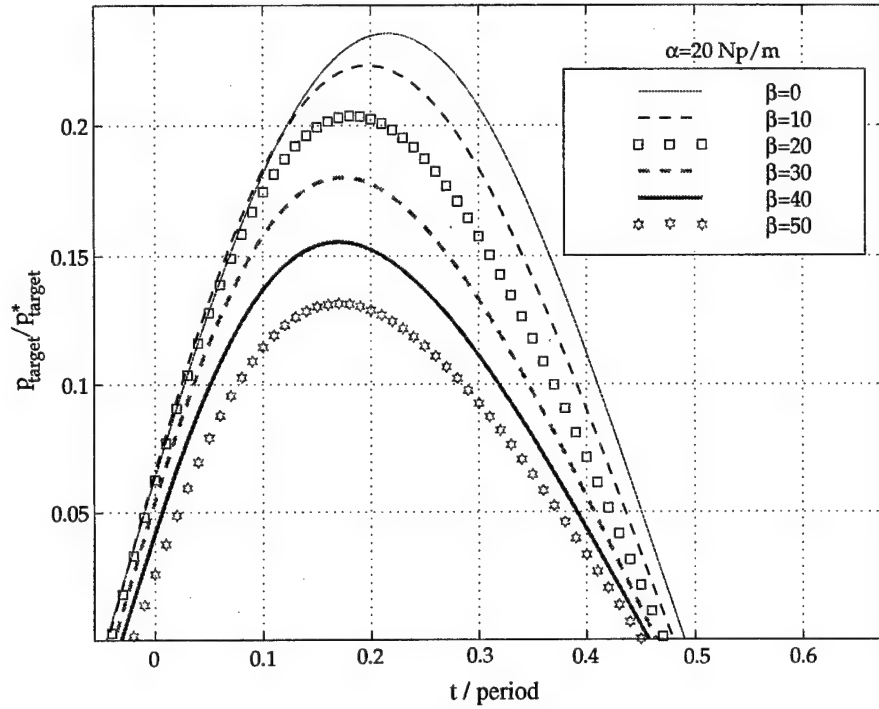
Figure 4.15: Nonlinear-nonlinear time reversal: Greatest positive half cycle of the pulse at the target for different values of β, with $\alpha = 20$ Np/m.

a β of 40.

For a higher absorption value, $\alpha = 20$ Np/m, the pressure at the target was even lower, see Fig. 4.15. Here the peak positive target pressure for $\beta = 0$ was about 24% of p^*_{target} due to the high absorption, and became less as β was increased through 50, where peak pressure was only 13% of p^*_{target} at a source-array separation of about 2.3 x_{shock}.

Fig. 4.16 shows how peak pressure at the target varied as a function of nonlinearity for $\alpha = 10$ and 20 Np/m. Nonlinearity is measured in terms of the number of shock

Figure 4.16: Nonlinear-nonlinear time reversal: Comparison of peak pressure at the target for different values of β, with $\alpha = 10, 20$ Np/m. While source-to-array distance, $x_{\text{src-array}}$ is constant, increasing β reduces the shock formation distance x_{shock}.

formation distances separating the array and the target. This can be related to β by

$$\frac{x_{\text{src-array}}}{x_{\text{shock}}} = 50\pi\beta\epsilon. \tag{4.29}$$

It was noticed that the rate of evolution of such mature pulses slowed down, as the creation of harmonics by nonlinearity was brought into balance with their absorption. Also, once significantly attenuated, the waveforms did not experience as much nonlinear distortion, owing to their smaller pressure amplitude.

As a measure of the effect of nonlinearity, when compared to the case $\beta = 0$, we noted a relative decrease in peak target pressure of about 22% when the source-target separation was 1 shock formation length for $\alpha = 10$ Np/m, and about 17% decrease for $\alpha = 20$ Np/m.
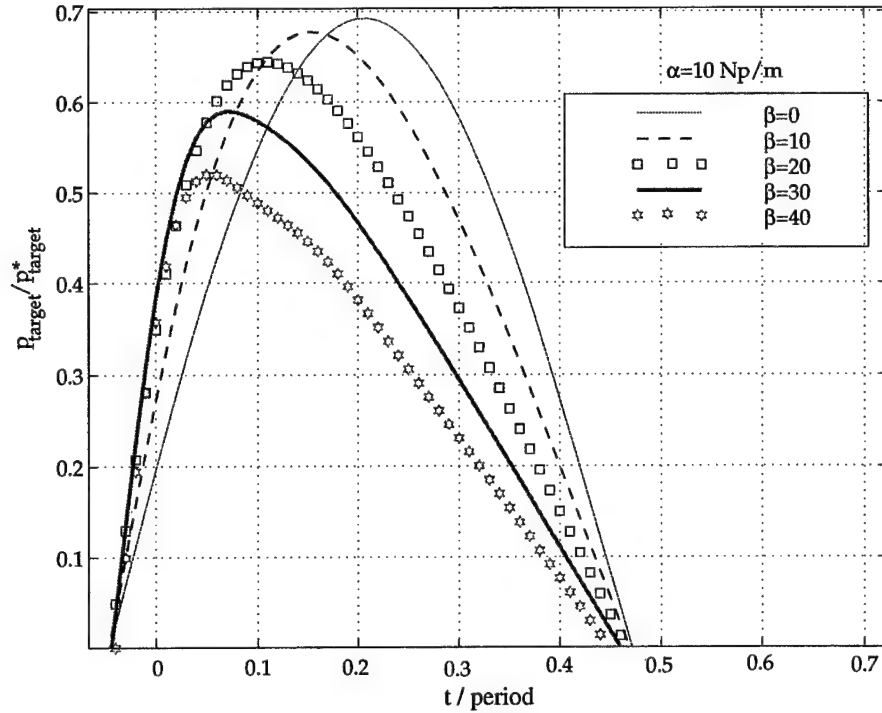
Figure 4.17: Linear-nonlinear time reversal: Greatest positive half cycle of the pulse at the target for different values of β, with $\alpha = 10$ Np/m.

4.5.9 Linear-Nonlinear Time Reversal

This scenario is the most common in acoustic phase conjugation experiments, where the source emits (or target is interrogated with) low-amplitude pulses, but in the transmit mode the retransmitted time reversed pulse is highly amplified. In these simulations the source emitted a 1 Pa acoustic pulse, which was captured by the array elements and retransmitted at 1 MPa, an amplification factor of $a \approx 10^6$, or 120 dB.

Fig. 4.17 shows results from the case where $\alpha = 10$ Np/m, and β was varied between 0 and 40, corresponding to Γ between 0 and 7.5. It was observed that
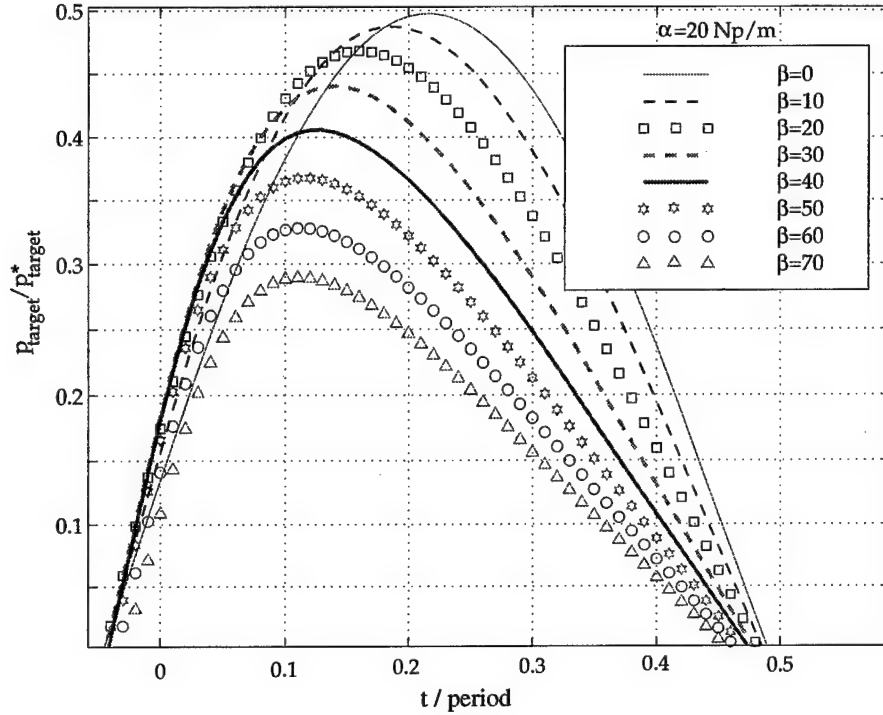
Figure 4.18: Linear-nonlinear time reversal: Greatest positive half cycle of the pulse at the target for different values of β, with $\alpha = 20$ Np/m.

in all of the runs having absorption the peak pressure at the target following time reversal was lower than p^*_{target}. This is to be expected from our proof in section 4.5.3. In addition, a monotonic decrease in retrofocusing peak pressure was observed with increasing nonlinearity parameter. Above a β of 40 the waveforms were too shocked to be simulated using the current method. The best result for this absorption value was obtained for $\beta = 0$, in which case the peak pressure at the target was 69% of p^*_{target}. As β was increased, equivalent to increasing the source-target separation up to about 3.3 shock formation distances, the peak target pressure was reduced to about 51% of p^*_{target}. So while the absorption was clearly responsible for time reversal focusing degradation, the presence of nonlinearity and the amplification at the array further

reduced peak target pressure by a further 25%.

More dramatic effects were seen when the absorption was increased to 20 Np/m. Fig. 4.18 shows the peak pressure half cycle at the target for the higher absorption. Here β was varied from 0 to 70 before numerical errors developed in the highly shocked waveforms. As before, the best time reversal refocusing was obtained when β was zero. In this case the peak positive pressure at the target was 50% of p^*_{target}. As β was increased to 70 (a Γ of 6.5), the peak attainable pressure dropped to less than 30% of p^*_{target}. The effect of both α and β on the peak positive achievable pressure at the target normalized to p^*_{target} is shown in Fig. 4.19 for the linear-nonlinear scenario.

As a measure of the effect of nonlinearity in the linear-nonlinear scenario, when compared to the case $\beta = 0$, we noted a decrease in peak target pressure of about 8% when the source-target separation was 1 shock formation distance for $\alpha = 10$ Np/m and about 6% for $\alpha = 20$ Np/m. This was about one third the relative decrement noted in the nonlinear-nonlinear scenario.

We further note that in comparison to Figs. 4.14 and 4.15 where approximately sinusoidal waveforms were recovered, Figs. 4.17 and 4.18 show highly distorted pulses recovered at the target. This is because in the linear-nonlinear scenario there is no nonlinear distortion from the receive mode to be undone by the distortion in the transmit mode, recall Muir's aforementioned experiment [59]. This could pose a problem in applications where pulse shape reconstruction is a measure of time reversal system performance.

4.6 Conclusions

This chapter described time reversal arrays, and studied the effects of various debilitating factors on the ability of time reversal systems to form intense pressures at the focus of the TRA. Initial phase uncertainty was studied in a simulated shallow water channel containing inhomogeneities and multipath reflections. It was found that the
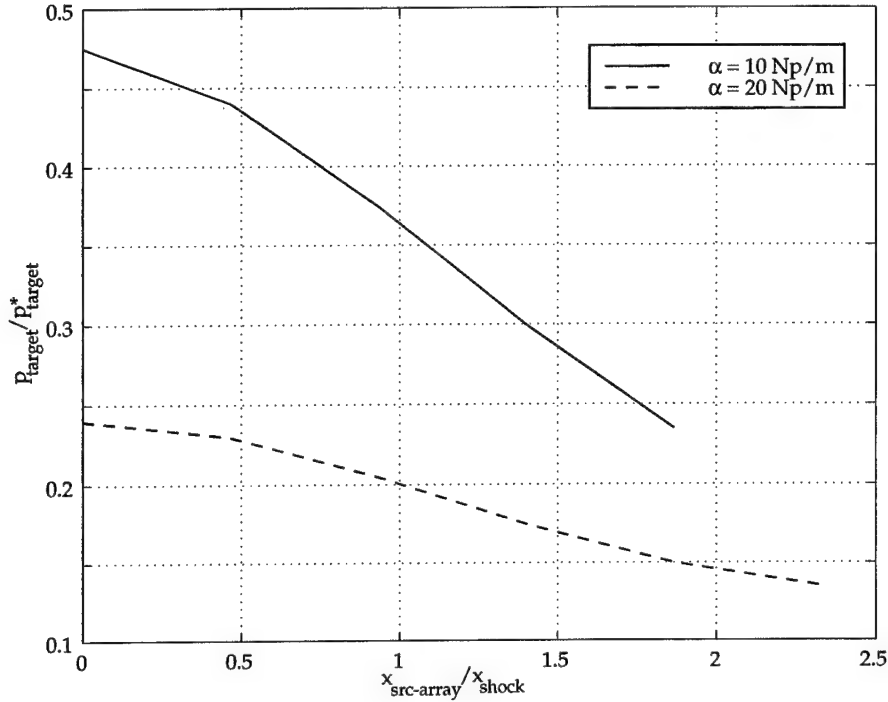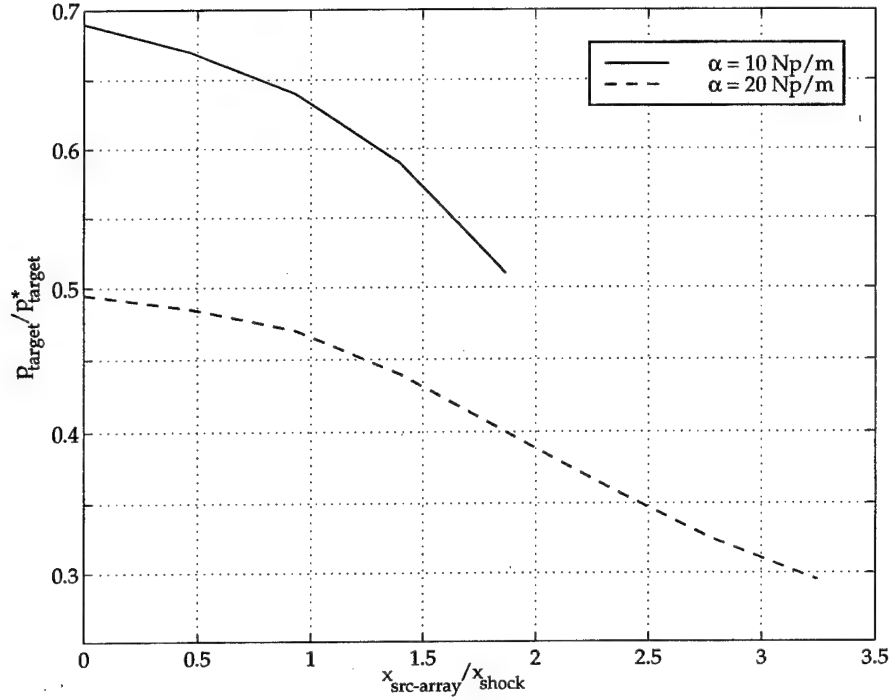
Figure 4.19: Linear-nonlinear time reversal: Comparison of peak pressure at the target for different values of β, with $\alpha = 10, 20$ Np/m. While source-to-array distance, $x_{\text{src-array}}$ is constant, increasing β reduces the shock formation distance x_{shock}.

maximum allowed delay errors in the initial signal phasing was equivalent to about 1/6 of a cycle for a periodic signal. Most applications of time reversal systems in acoustics exploit their ability to backpropagate acoustic energy to a scattering target or a source. As such, it is important to know the limits of usefulness for such retrodirective focusing, or the potential for achieving maximal intensity at the focal spot. One issue known to plague time reversal systems is absorption in the propagation medium. Amplitude compensation has been used with some success to correct for amplitude distortion [66], but such techniques have not been explored for nonlinear propagation, in which case the amplitude compensation at the array will have detrimental effects of its own. This study assumed that the effectiveness of a time reversal

system can be measured solely by the amplitude of the pressures at the target. However, in some cases the waveform shape may also contribute to the fidelity of the time reversal. Under nonlinear propagation conditions this fidelity will be compromised by the tendency for the positive portions of the waveform to travel at greater sound speed than the negative portions of the waveform.

It was shown that time reversal focusing can still occur in absorbing media, since the phasing of the signals is not affected, however, the absorption leads to a violation of time reversal invariance, and hence the effectiveness of the TRA is compromised if the goal is achieving a high-intensity focus. While the spatial extent of the focal spot is unaffected by the inclusion of absorption, the reduction in peak amplitude causes an increase in the FWHM of the focus.

Since most media exhibit a frequency power law of absorption, it is important to know what effect the nonlinear harmonic generation will have on time reversal systems if they are to be used at finite amplitude. Another issue raised by this study is how amplification of the signals received by the array elements will compromise the time reversal process. We showed that for the nonlinear-nonlinear case the nonlinearity in the wave equation only affects the time reversal invariance in that it introduces extra absorption due to the generation of higher frequency content in an acoustic waveform. This indirect effect appears to be nearly as important as the medium's absorption coefficient in cases where well-formed shock waves appear, or where propagation over several shock formation lengths occurs. Caution is in order if one contemplates increasing the gain on the time reversal array element amplifiers in an attempt to overcome the focusing loss, as in the linear-nonlinear case. Since the shock formation distance is directly related to the peak source pressure, shock formation will occur sooner, leading to a reduction in the performance of the system for a given source-array separation. We conclude that altering the amplitude of the time reversed signals at the array will lead to degradation of the focus in a nonlinear propagation situation, even if the medium is lossless.

It was shown that for propagation over several shock formation distances the effects of nonlinearity-enhanced absorption are almost as important as the effects of the absorption itself. The extra absorption of shocked waveforms will significantly degrade the ability of a time reversal system to deposit a high-intensity acoustic pressure field onto a target. Additionally, amplitude alteration at the array elements in a nonlinear medium can have detrimental effects on the time reversal array's performance. These results have implications for future uses of high-intensity acoustic time reversal systems such as mine neutralization, hyperthermia, and lithotripsy using time reversal arrays.

Chapter 5

TISSUE HYPERTHERMIA USING FOCUSED SOURCES

5.1 Introduction

There exists ample motivation to explore the possibility of performing noninvasive, or bloodless, treatment of deep-seated tumors in the human body. Traditional surgery to reach and remove tumors requires cutting a path to the affected region, controlling the damage to the intervening organs, controlling the resultant bleeding, and maintaining infection-free conditions during and after the surgery. The concept of using focused ultrasound to destroy the offending tumor tissue by heating it until the affected cells die due to the thermal dose was postulated almost half a century ago [29]. It is only recently that the technology to build and control and image the focused ultrasound surgery has become possible. These efforts have intensified in the past ten years, as successful experiments in animals have been conducted, and a small but aggressive industry now seeks to test and license such devices for treatment in humans.

General descriptions of focused ultrasound surgery (FUS), also known as high-intensity focused ultrasound (HIFU), are given in Hynynen [47], ter Haar [65], and Sanghvi and Hawes [63]. Research on therapeutic ultrasound is interdisciplinary, and is of interest to scientists working in medical applications as well as clinicians with some grasp of the physics and engineering of ultrasound. This study maintains the perspective of physical acoustics and does not emphasize the pathology of cell injury. The mechanism for the destruction of the afflicted tissue sites is known as *necrosis*, associated with the pathologic change following progressive degradation due to lethal injury of living cells. Cell structure and membranes are known to suffer as a result of

thermal overdose from the deposition of acoustically-driven heat in the tissue. Other mechanical damage, notably as a result of cavitation are known to occur at high intensities [46, 71], but are not investigated here.

Because of the complexity of propagation in biological tissue, analytical and computational solutions to pressure field and heating calculations can only be obtained using simplifications and assumptions. For example, when describing medical ultrasound devices and their effect it is common to find the assumption that the propagation medium is homogeneous [9, 15], linear [36, 56, 58, 39], or both [14, 24, 74, 32, 35]. Sophisticated numerical studies have been conducted recently whereby measured tissue properties are used in the calculation of acoustic fields [57, 38, 40].

Despite the recent advances in computational power, realistic three-dimensional simulations remain slow, costly, and conspicuously absent from the literature. One reason for this other than the computing shortage is that 3-D measurements in tissue would require unconventional measurement techniques such as MRI or tomography, and would be much more difficult to obtain. Some important problems in wave propagation can be studied using finite-difference methods in 2-D. This chapter presents results from simulations of therapeutic ultrasound in tissue-like media. The questions addressed are: what are the effects of nonlinearity and absorption on the propagation and heating of a focal region? and what is the effect of medium inhomogeneity, and the effect of temperature-dependent tissue parameters on the heating behavior near the focus of therapeutic ultrasound devices? Single pulse and continuous wave (CW) simulations were carried out. The modeling of the acoustic propagation and focused sources has already been given in Chapter 2. In this chapter a common model for the thermal behavior of tissues, known as the bioheat equation, will be explained, and means of coupling the acoustic and the thermal aspects of the problem will be presented.

The simulations address the following phenomena and their effect on transient and steady-state acoustic pressure and temperature fields: First, the nonlinear effects

resulting from propagation from pulsed devices which can produce finite-amplitude effects. Second, the effect of inhomogeneities in two dimensions, as deduced from simulations in data from slices of human tissue obtained by experimental measurements, reported by other researchers. Third, the effect of temperature-dependent, time-varying tissue background parameters. It is found that inhomogeneity of soft tissue can have the effect of displacing and breaking up the site of sound and heat deposition, but will have little effect on the overall thermal dose. Finite-amplitude effects are more important in calculating the size and temperature of the hot spot. Temperature-dependent tissue characteristics appear to be quite important in prediction of thermal effects of focused ultrasound from CW devices.

5.2   Heating Model: The Bioheat Equation

As a consequence of the thermal and viscous properties of fluids, energy loss results when an acoustic disturbance passes through the fluid. The acoustic wave deposits the absorbed energy as heat [61, 14, 74]. For the case of tissue, a linear *bioheat equation* commonly used to describe the thermal effects [16] is

$$\frac{\partial T}{\partial t} = \frac{K_{\text{tiss}}}{\rho C_{\text{tiss}}} \nabla^2 T - \frac{W_b C_b}{\rho C_{\text{tiss}}} (T - T_a) + \frac{Q}{\rho C_{\text{tiss}}} \qquad (5.1)$$

where T is the difference between the tissue temperature and the ambient (arterial) temperature ($37^\circ C$), K_{tiss} is the thermal conductivity of the tissue (0.6 W/m-K), C_{tiss} is the heat capacity (3700 J/kg-K), W_b is the perfusion or cooling by blood flow (0.5 kg/m^3-s), C_b is the heat capacity of the blood (3800 J/kg-K), T_a is the ambient arterial temperature, and Q is the heat deposition source term, described in Pierce [61],

$$Q = \frac{2\alpha}{\rho_0 c_0 \omega^2} \left(\frac{\partial p}{\partial t}\right)^2 . \qquad (5.2)$$

We assume that α is the loss due to absorption, and scattering loss is negligible in the attenuation of sound. In a thermoviscous fluid, the absorption α is related to δ

and $\omega = 2\pi f$ by [42]

$$\delta = \frac{2c_0^2 \alpha}{\omega^2} \tag{5.3}$$

5.2.1 FDTD Solution of the Bioheat Equation

In a manner analogous to the solution of the wave equation, we solve (5.1) using the FDTD method. The partial derivatives are discretized to second order, and the temperature is advanced in time from one time step to the next. Define the variables on the interior grid cells having spatial and temporal discretization δ_x and δ_t respectively,

$$A_t = \frac{1}{2\delta_t}, \tag{5.4}$$

$$A_x = \frac{1}{(\delta_x)^2}, \tag{5.5}$$

$$A_y = \frac{1}{(\delta_y)^2}, \tag{5.6}$$

$$B_{i,j} = \frac{K_{\text{tiss}}}{\rho_{i,j} \, C_{\text{tiss}}}, \tag{5.7}$$

$$C_{i,j} = \frac{W_b \, C_b}{\rho_{i,j} \, C_{\text{tiss}}}, \tag{5.8}$$

$$D_{i,j} = \frac{2 \, \alpha_{i,j}}{\rho_{i,j} \, c_{i,j} \, \omega^2}, \tag{5.9}$$

and

$$V_{t\,i,j} = (T_{i,j}^{n+1} - T_{i,j}^{n-1}), \tag{5.10}$$

$$V_{x\,i,j} = (T_{i+1,j}^n - 2T_{i,j}^n + T_{i-1,j}^n), \tag{5.11}$$

$$V_{y\,i,j} = (T_{i,j+1}^n - 2T_{i,j}^n + T_{i,j-1}^n), \tag{5.12}$$

$$V_{a\,i,j} = (T_{i,j}^n - T_a). \tag{5.13}$$

The partial derivatives are written to second order

$$\frac{\partial T}{\partial t} = A_t\ V_t,$$
$$\frac{\partial^2 T}{\partial x^2} = A_x\ V_x, \tag{5.14}$$
$$\frac{\partial^2 T}{\partial y^2} = A_y\ V_y,$$

and the source term, $Q_{i,j}^n$ can be calculated from

$$Q_{i,j}^n = D_{i,j}\ A_t{}^2\ (p_{i,j}^{n+1} - p_{i,j}^{n-1})^2. \tag{5.15}$$

The bioheat equation then can be used to solve for the temperature at the next time step, $n+1$,

$$T_{i,j}^{n+1} = (\frac{1}{A_t})^2 \left[B_{i,j}(A_x\ V_{xi,j} + A_y\ V_{yi,j}) - C_{i,j}\ V_{ai,j} + \frac{Q_{i,j}^n}{\rho_{i,j}C_{\text{tiss}}} \right] + T_{i,j}^{n-1}. \tag{5.16}$$

5.3   The Effect of Nonlinearity: Single Pulse Simulations

Theoretical and experimental studies of nonlinear propagation and focusing in tissue and tissue-like materials have shown that increased heating will result from steepened or shocked waveforms in tissue. There has been increasing interest in the use of high intensity ultrasound in tissue. At high intensities finite-amplitude effects can lead to the production of nonlinearly generated harmonics. These harmonics have been exploited in recent years to improve imaging capabilites in diagnostic ultrasound machines - a technique commonly referred to as harmonic imaging. In addition, focused ultrasound surgery (FUS) is a promising technique that uses high-intensity ultrasound to destroy tissue in a confined region which will avoid the necessity of traditional invasive methods.

The explanation for increased heating from nonlinear ultrasonic applicators is explained by Wu and Du [75] and Bacon and Carstensen [3], and can briefly be summarized as follows: Most materials exhibit a frequency power law for the absorption of sound, i.e., the conversion of acoustic energy into heat energy. For single-frequency

waves, the small signal absorption coefficient, α, depends on the frequency of the acoustic waves, f, and a real exponent, ν,

$$\alpha \sim f^{\nu}, \tag{5.17}$$

where ν is between 1 and 2, and is about 1.1 for most soft tissues [2]. The nonlinear generation of higher-frequency harmonics implies excess absorption will occur for steepened or shocked waveforms.

While bioeffects have been widely studied in the laboratory [65], it is difficult to obtain detailed spatial measurements without disrupting the acoustic field. It has been known for some time that high intensity ultrasound, and the accompanying finite-amplitude effects result in different bioeffects than linear propagation would predict [3, 10]. In a thermoviscous fluid, the absorption is proportional to the square of the frequency, so as higher frequency content is generated during wave steepening, it has been shown that increased heating will result.

5.3.1 Results of the Nonlinear Simulations

Some simulation results are shown in this section to illustrate the output of the numerical code. The example outputs are for a focused bowl source array of 64 simple sources having azimuthal symmetry. The source was driven by a 1 MHz sinusoidal burst of 6 cycles modulated by a Gaussian envelope in time. The geometric focus of the array was situated 3 cm from the array face. The source aperture was 4 cm; the computational domain spanned an area of 5.12 cm $\times$ 5.12 cm. The grid spacing was $\Delta x = \Delta r = 0.1$ mm and $\Delta t = 10$ ns.

The propagation medium was modeled as a tissue-like material, having properties similar to those reported in the literature for soft tissue.[13] The parameters used in the acoustic problem were: $c_0 = 1600$ m/s, $\rho_0 = 1100$ kg/m^3, $\alpha = 4.5$ Np/m, and $\beta = 5.5$. For the bioheat equation the following parameters were used: $k_t = 0.6$ W/(m·K), $C_t = C_b = 3800$ J/(kg·K) and $W_b = 0.5$ kg/(m^3·s). Figure 1 shows some
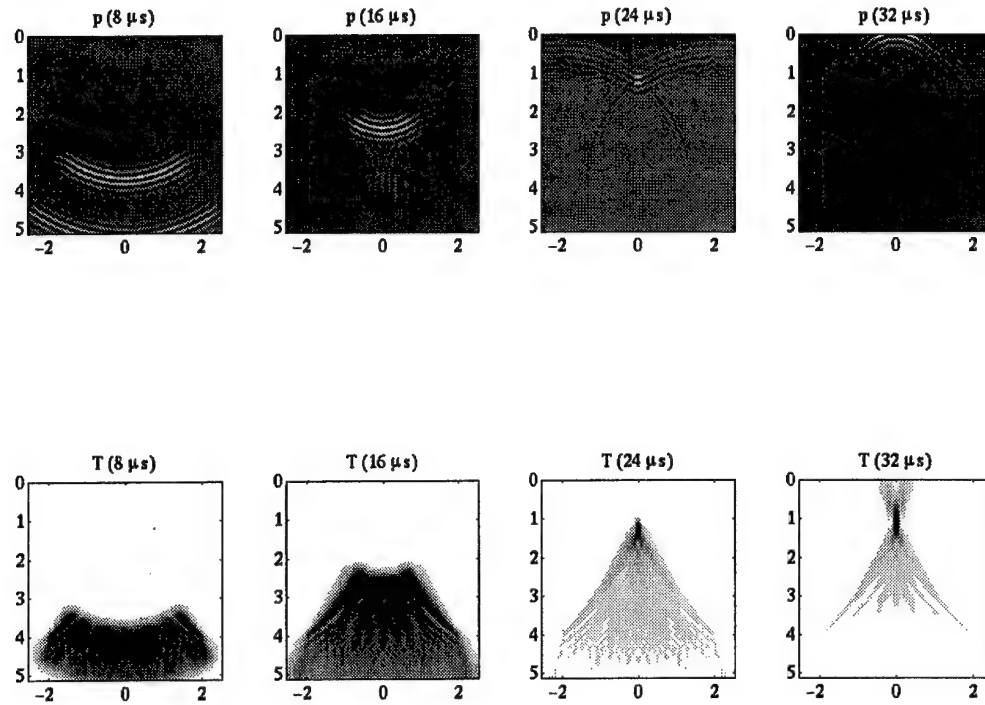
Figure 5.1: Snapshots of the pressure (top row), and temperature (bottom row) for the 1 MPa nonlinear simulation. The axes are labeled in cm.

snapshots of the pressure and temperature fields resulting from nonlinear propagation in the medium.

Figure 5.3.1shows axial slices of the temperature fields at 32 μs for linear and nonlinear simulations at source pressures ranging from 1 MPa to 10 MPa. The linear simulations were achieved by setting β to zero. Temperature elevation increased with source pressure. For nonlinear simulations excess heating increased dramatically for source pressures above 5 MPa. For the 1 MPa nonlinear simulation the the heating was only 2% above the linear predictions and at 2 MPa the excess heating was 4%. However, at 5 MPa excess heating was 27% and at 10 MPa it was 80%. High source levels were required to observe excess heating because the entire propagation path was
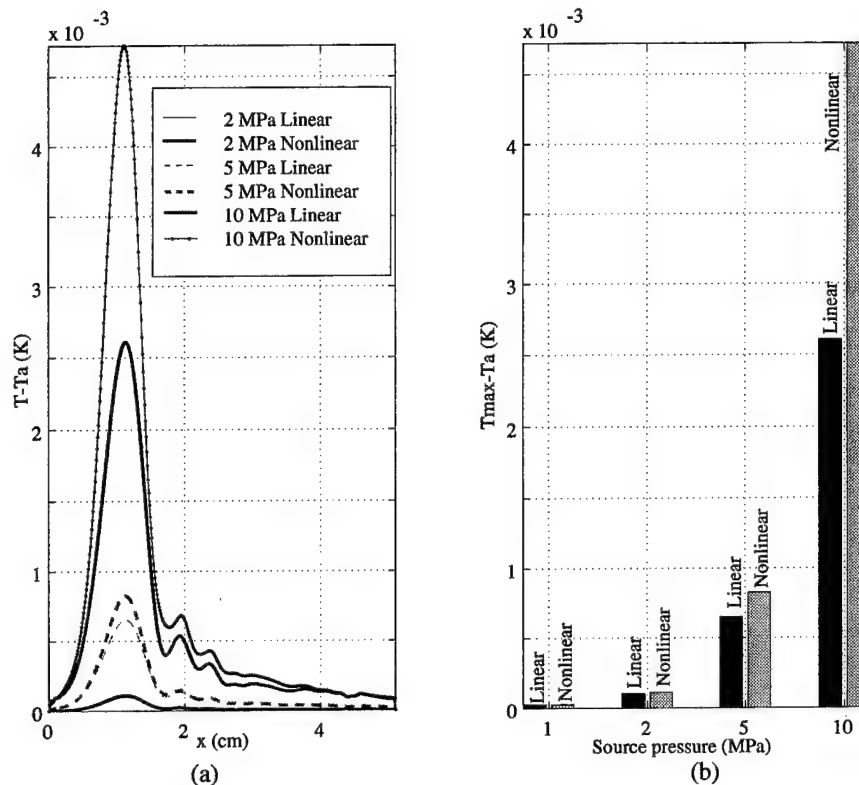
(a) Axial slices of the temperature at 32 μs for various source pressures with and without nonlinearity. (b) Peak temperature elevation for several source conditions, showing the increasing effect of nonlinear distortion.

modeled as tissue. Tissue has a relatively large absorption and prevents steep shocks, with significant harmonic content, from forming. For propagation through water, which is much less absorbing, steep shocks occur much more readily and consequently excess heating becomes important at lower source levels.

5.3.2 Conclusions from the Nonlinear Effect Simulations

Accurate knowledge of the behavior of ultrasonic beams in tissue allows for better prediction of bioeffects of ultrasound, and improved treatment and device design. The

FDTD method for simulation of transient finite-amplitude acoustic fields has been described with an application in medical ultrasound used as an example. Heating in tissue, modeled as a thermoviscous fluid, was obtained for a short acoustic pulse from a focused bowl source. Peak temperature rises from a 1 MHz ultrasonic pulse propagating nonlinearly through a tissue-like material was observed to depend on the degree of nonlinear distortion and ranged from 2% to 80% excess temperature rise for 1 MPa to 10 MPa source pressure conditions.

5.4   The Effect of Inhomogeneity: A 2-D Study

In this section we look at the role played by tissue inhomogeneity in the context of nonlinear therapeutic ultrasound propagation. A 1 MHz pulse of ultrasound is propagated using FDTD simulations in 2-D Cartesian coordinates. The propagation medium was constructed from 2-D measurements of tissue propagation delay times obtained from researchers at the University of Rochester, described by Hinkleman, et al., [43, 44]. The data were adapted for our use in the simulations by scaling the magnitude of the inhomogeneity in sound speed, density, absorption coefficient, and nonlinearity coefficient to the desired contrast. In the original study, human breast and abdominal wall tissue slices were preserved, and delay times were measured at fine intervals across the samples, generating a 2-D map of the inhomogeneities in the samples. One such sample is used in this study. It can be expected that local effects such as diffraction and hot spot distortion occur in inhomogeneous media. We look at this effect in the context of therapeutic ultrasound as a function of the strength of the inhomogeneity.

5.4.1   Description of the Propagation Medium

The inhomogeneity contrast (magnitude of the variations in background propagation parameters) is controlled for the study, and varies from ±0% (homogeneous tissue)
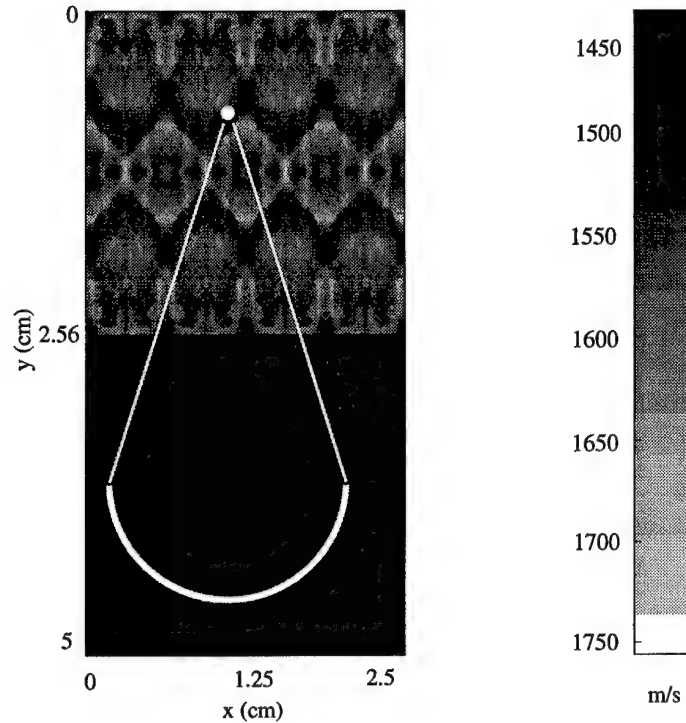
Figure 5.2: The sound speed used for the ±10% inhomogeneity contrast case, having a base value of 1600 m/s in tissue half plane, and 1500 m/s in the water half plane. The position of the curved source and geometric focus are also shown. Note that the source is slightly offset to the left to avoid the occurrence of left-right symmetries about the center.

to ±20% contrast. The following assumptions are made in generating the data files for the background properties:

1. Data was only provided for delay time, or sound speed. We assume the inhomogeneous contours for sound speed delineated regions of different tissue type and composition. Hence it is assumed that all tissue properties vary along the same contour lines in space.

2. The percentage of contrast in each of the background properties is the same.

i.e. a ±10% variation in sound speed implies a ±10% variation in density, *etc.*

3. There exists a qualitative correlation between the sign of the variation in the properties compared to the time delays. The assumption used here is that sound speed, density, and absorption coefficient have the same tendency to increase or decrease together, while the nonlinearity coefficient tends to violate this direction, *i.e.* a ±10% variation in sound speed corresponds to a ∓10% variation in nonlinearity coefficient. This last assumption is borne by qualitative examination of tissue measurement data given in the literature [33, 34, 77].

It is known that realistic 3-D inhomogeneities will have a quantitatively different effect than the present 2-D inhomogeneities, but 3-D data is not available for such a study at this time. We expect 3-D diffraction to have a more severe effect on the pressure and temperature fields than 2-D diffraction, and so the results reported here are expected to be conservative in their estimation of real body effects.

The inhomogeneous initial condition data file for a medium parameter, $\chi_0(x, y)$, which is a function of 2-D space is generated according to the following formula:

$$\chi_0(i, j) = \chi_{00} + \frac{r}{100}\, \chi_{00}\, Z(i, j), \qquad (5.18)$$

where χ_{00} is a reference background value to be perturbed according to the template file, Z, which contains the inhomogeneous data measured and normalized to lie between $[-1,\ 1]$, and r is the contrast (percent) desired for the run. Only one half of the computational domain is filled with this inhomogeneous tissue-like medium. The other half is assumed to be homogeneous water containing the focused source. An example of an inhomogeneous data file used in these simulations in given in Figure 5.2, showing a ±10% contrast in sound speed. The measured data were only given on a 32×128 grid due to the original sample size. For the purposes of the simulations, the measured data was extended over the entire tissue portion of the domain by tiling and reflecting it to fill a 256×256 grid region. This increased the apparent size of the
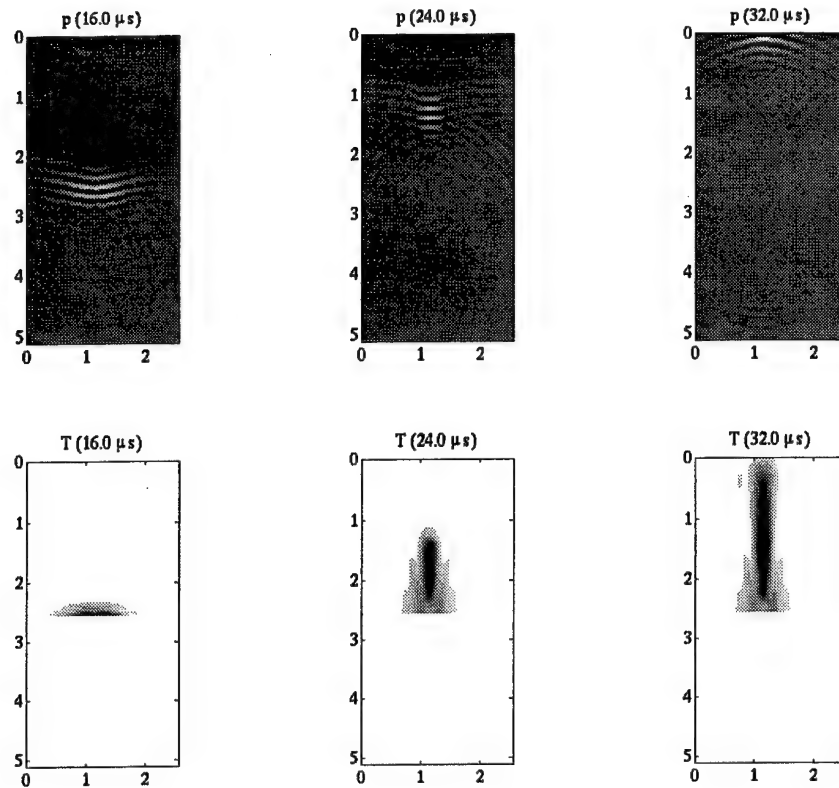
Figure 5.3: Acoustic pressure and temperature above background (37°C) at 16μs, 24μs, and 32μs. The water half plane appears unheated due to the very low absorption coefficient in water compared to tissue. Each figure is scaled independently to take advantage of the full gray-scale color range. Axes labeled in cm.

tissue sample, while minimizing any effects of repetition on the sound field, *e.g.* giving artificial discontinuities, which could cause reflections. Since the inhomogeneous data is symmetrical about the x=1.28 cm position to the left and to the right, the source was slightly offset to the left so that the left and the right portions of the beam do not pass through identical media.

Figure 5.4: Acoustic pressure and temperature above background (37°C) at 16μs, 24μs, and 32μs for the $\pm$10% inhomogeneity contrast case. Axes labeled in cm.

5.4.2 Results From the Inhomogeneous Medium Study

The reference (no inhomogeneity, zero contrast) run was one having two half planes, each of which was homogeneous. The water half plane uses the following values for all the simulations in this study:

$$
\begin{aligned}
c &= 1500 \text{ m/s,} \\
\rho &= 1000 \text{ kg/m}^3, \\
\alpha &= 2.88 \times 10^{-4} \text{ Np/m,} \\
\beta &= 3.5.
\end{aligned}
\tag{5.19}
$$

The mean values for the tissue parameters, about which the inhomogeneous files were built were:

$$c = 1600 \text{ m/s},$$
$$\rho = 1100 \text{ kg/m}^3,$$
$$\alpha = 4.5 \text{ Np/m},$$
$$\beta = 5.5.$$

(5.20)

These parameters are similar to those published in a number of sources over the last two decades [33, 34, 77]. Note the 4 orders of magnitude disparity in the absorption coefficient between water and tissue. For this reason, the temperature profile shows measurable temperature rise only in the tissue half plane, while the water half plane heating is negligible.

Snapshots from the pressure and corresponding temperature calculations for the reference run are shown in Figure 5.3. Only the water-tissue interface interferes with the beam. The snapshots are taken at 16, 24, and 32 microseconds from launch at the source. Peak focusing occurred at about 24 μs as the pulse reached the geometric focus. The thermal hot spot continues to heat up even after 24 μs because of the slow time to dissipate heat by conduction and perfusion. Upon introducing inhomogeneities within the tissue, the acoustic focus is broken up and distorted at various scales. This is seen in Figure 5.4 along with its effect on the temperature distribution for the $\pm 10\%$ inhomogeneity contrast case. Increasing the inhomogeneity contrast to $\pm 20\%$ results in the fields shown in Figure 5.5. Slices along the x and y axes are taken from the acoustic pressure fields for the contrast cases $\pm 0\%$, $\pm 10\%$, $\pm 20\%$ at 24μs and are shown in Figure 5.6. The acoustic field is scattered and distorted by the inhomogeneities in the case for nonzero contrast in the tissue. This can be seen in the reduced amplitude of the field at the geometric focus. Note that this reduction does not stem from increased absorption, but is due to the fact that the slices were taken through the geometric focus. In other slices in the plane it will appear that the
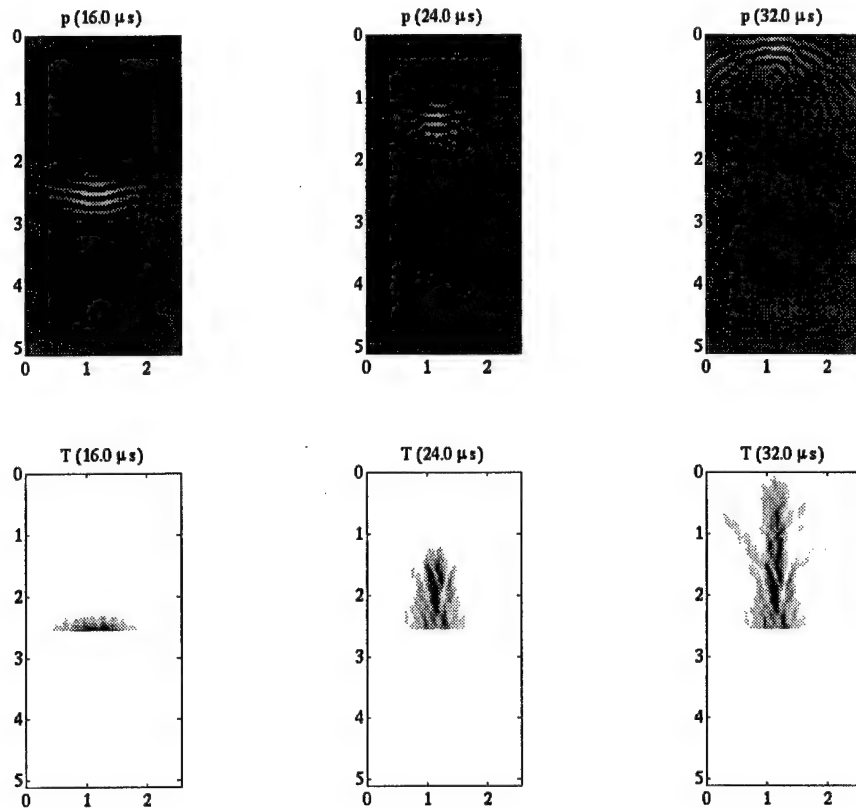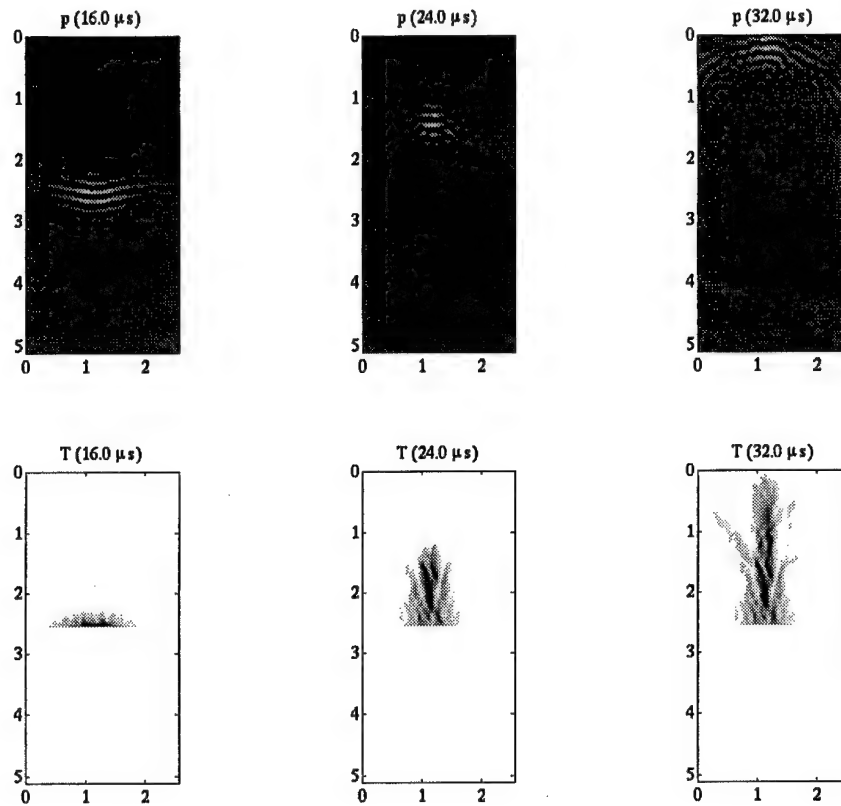
Figure 5.5: Acoustic pressure and temperature above background (37°C) at 16μs, 24μs, and 32μs for the ±20% inhomogeneity contrast case. Note that the ±20% and the ±10% cases give qualitatively similar results, because the inhomogeneities are in the same locations. Axes labeled in cm.

inhomogeneous case fields are stronger there. Reflection from the water-tissue interface can be seen at about x=2.75 cm. The reflections from all three slices coincide, as the travel path between the source to the interface through homogeneous water is the same. The temperature profiles along slices in x and y passing through the geometric focus are shown in Figure 5.7 at 32μs. Again, comparisons of the overall heating effect are difficult to make based on slices through any particular point, as the local effects of the inhomogeneity will affect the slice profiles.
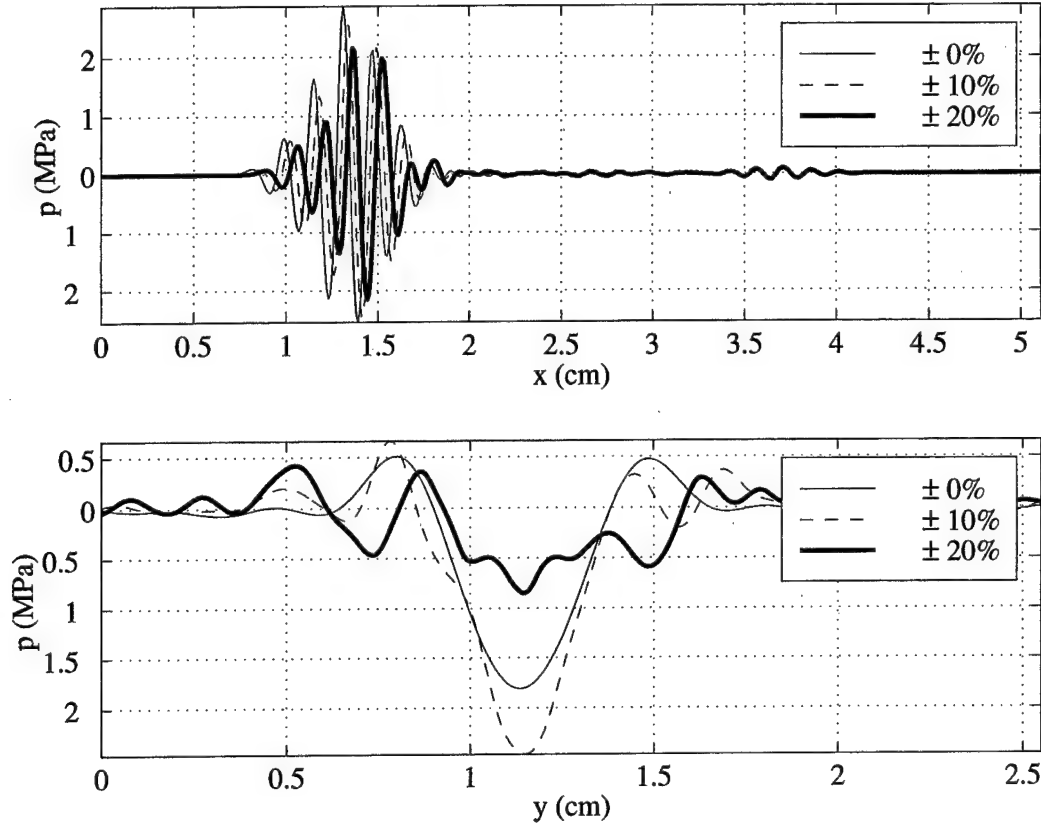
Figure 5.6: Acoustic pressure slices along x and y through the geometric focus for the ±0%, ±10%, and ±20% inhomogeneity contrast cases.

The Overall Effect of Tissue Inhomogeneity

It is difficult to gauge the effect of tissue inhomogeneity on the heating by taking single slices through the tissue. Instead, we perform a numerical integral in 2-D space over the tissue half-plane to determine the average heating that occurred in this region of interest. The formula used is

$$T_{sum} = \sum_i \sum_j T_{i,j} \tag{5.21}$$

where the sum is taken over the computational domain. We find that T_{sum} is identical, independent of the amount of inhomogeneity contrast present. The reason for this is
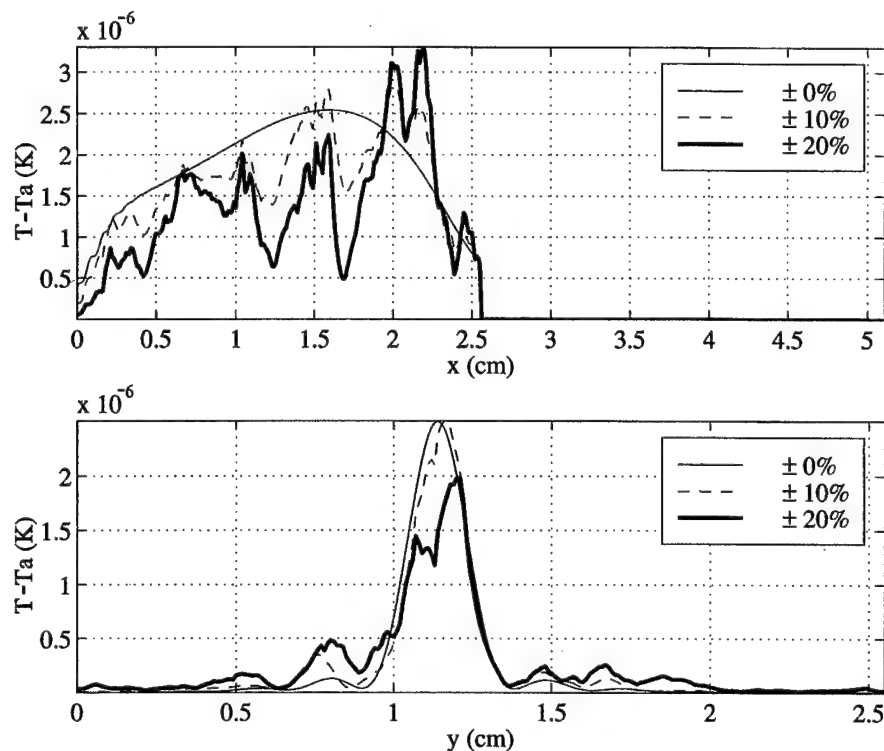
Figure 5.7: Temperature elevation slices along x and y through the geometric focus for the ±0%, ±10%, and ±20% inhomogeneity contrast cases.

that while the beam pattern is distorted in the region of interest for the inhomogeneous runs, the amount of absorption and the center frequency remain the same as for the reference case. Hence, the amount of acoustic energy deposited is the same.

The localized field distortion in inhomogeneous tissue leads to local regions of elevated temperature which can lead to higher peak temperatures than for the zero contrast case. Small-scale diffraction and lensing effects are more pronounced for the runs with higher inhomogeneity contrast. Figure 5.8 shows the peak temperature found in the tissue for each of the inhomogeneity contrast runs for the same initial conditions at the source. It is noted that a monotonic trend to higher peak local temperatures is obtained as inhomogeneity contrast increases. This can have rami-
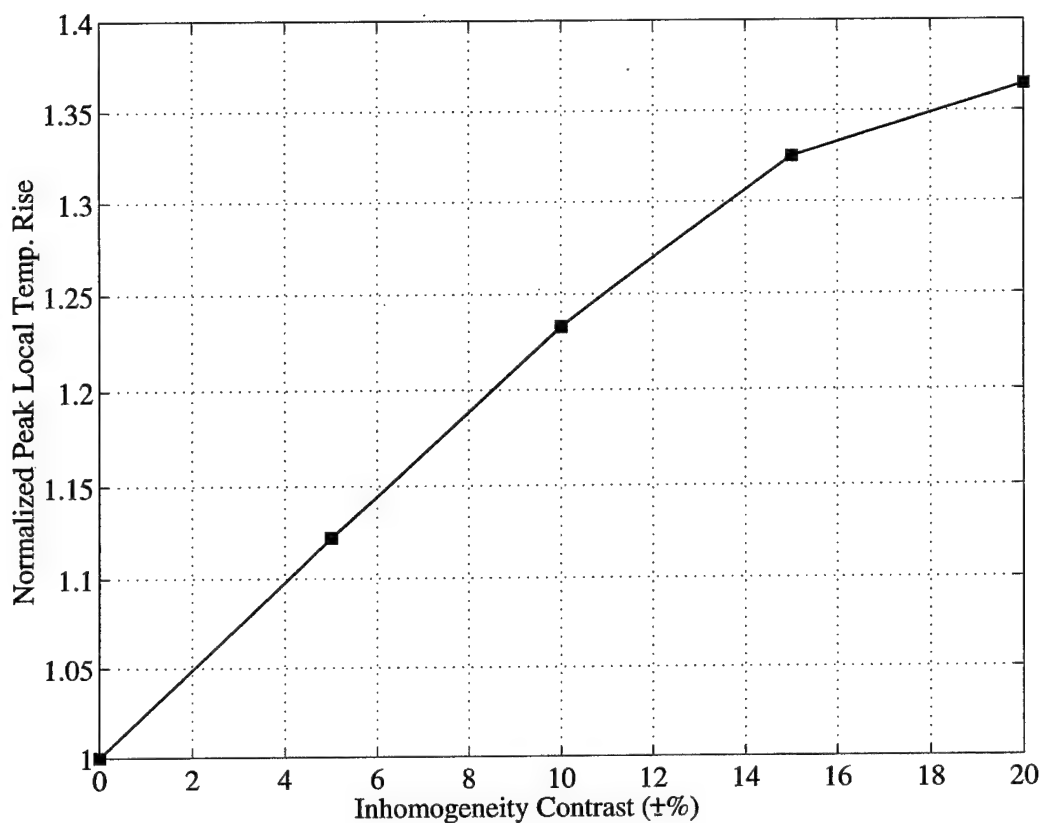
Figure 5.8: Peak local temperature rise found in the tissue for various inhomogeneity contrast cases, showing a general trend to higher peak local temperatures for higher inhomogeneity contrast.

fications to dose and safety studies, where the maximum pressure and temperature may be of concern. Real soft tissues can be expected to exhibit about ±10% inhomogeneity contrast in the values of their background propagation parameters at constant temperature, depending on the organ [43].

5.4.3 Severe Inhomogeneity Effects

Next we look briefly at an example where a severe mismatch in properties between the tissue and some inclusion in the tissue exists. This may occur if a cavitation

cloud, a gas pocket, or a bone cross section are in the path of the propagation. In our example we assume the properties within the inclusion are homogeneous, and have the values
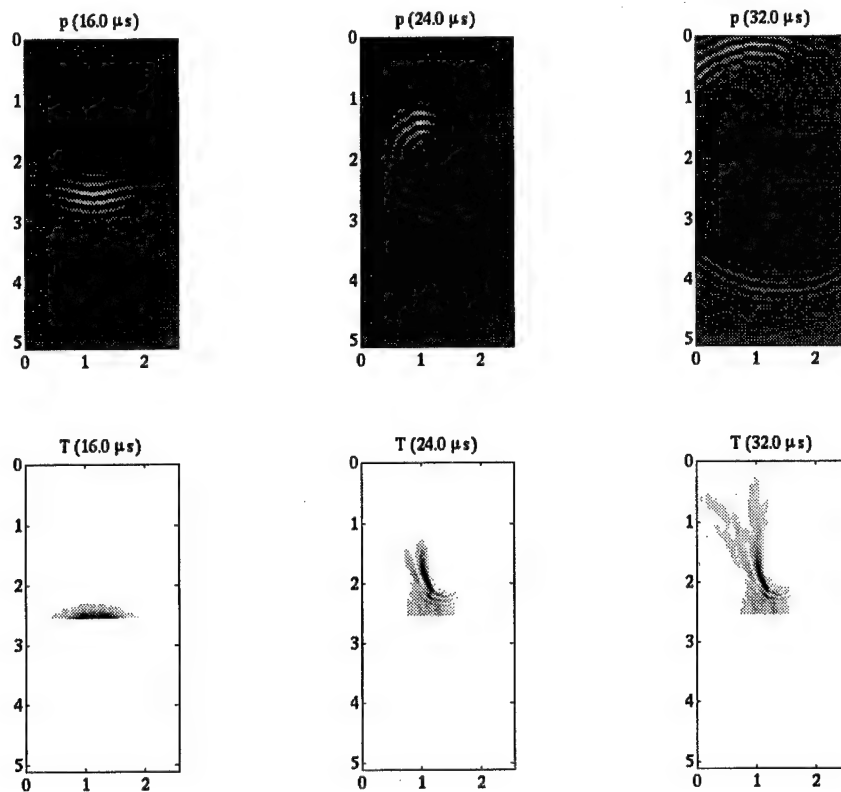
Figure 5.9: Pressure and temperature elevation for the case where a severely mismatched cavity inhomogeneity lies in the tissue in the vicinity of the beam. Axes labeled in cm.

$$
\begin{aligned}
c &= 250 \text{ m/s}, \\
\rho &= 500 \text{ kg/m}^3, \\
\alpha &= 1 \text{ Np/m}, \\
\beta &= 10.
\end{aligned}
\tag{5.22}
$$

These values attempt to represent parameters which might be found in a region containing cavitation bubbles. No details of the properties of such an inclusion are available at the time of writing, but it can be expected that both the sound speed and the density of the effective medium are lower than that of the tissue, and that the nonlinearity coefficient would be significantly higher than that of the tissue [42].

Figure 5.9 shows simulation output from an example with strong scattering. The severe ρc mismatch displaces the pulse to the left (24μs), and leaves a distorted hot spot (32μs). The tissue inhomogeneity contrast for this run was $\pm 10\%$. Output such as this suggests that focused ultrasound surgery is most accurate in soft tissue with minimum obstructions. Any significantly mismatched inclusion will move a typical size therapeutic beam off course by an amount comparable to the size of the inclusion. Further, treatment of tissue in the inclusion's shadow is precluded if the mismatch leads to strong scattering of the sound.

5.5 CW Heating in Quiescent Tissue

We now consider tissue heating due to continuous wave (CW) insonation. The insonations presented in the following sections will have longer durations than the single pulses seen earlier. For insonations of several seconds duration we can expect real tissue to experience physical changes in its material properties. These time-varying background (TVB) changes will be discussed in the next section, but for now we limit our study to quiescent, or unchanging tissue. For these simulations we use the same acoustic and thermal algorithms developed earlier in this chapter, but we allow the source to be active for a longer duration (100 μs) so that the entire computational domain can be filled with sound and reach a time-harmonic steady state. Figure 5.10 shows snapshots of the pressure and temperature for a 100 μs pulse, which is long enough for the acoustic pressure field to reach a time-harmonic steady state, as propagation across the computational domain requires only 30 μs. Absorbing boundary

conditions on all outer edges of the computational domain act to minimize reflected sound waves into the interior of the domain. Since all the remaining calculations require knowledge of the acoustic pressure field only in addition to the tissue properties, we can use the results from the long pulse simulation to infer the behavior of the pressure and temperature fields for any time period desired. This assumption that the pressure field will look the same from one acoustic cycle to the next is what we call continuous wave (CW) behavior in a quiescent medium. To confirm that the
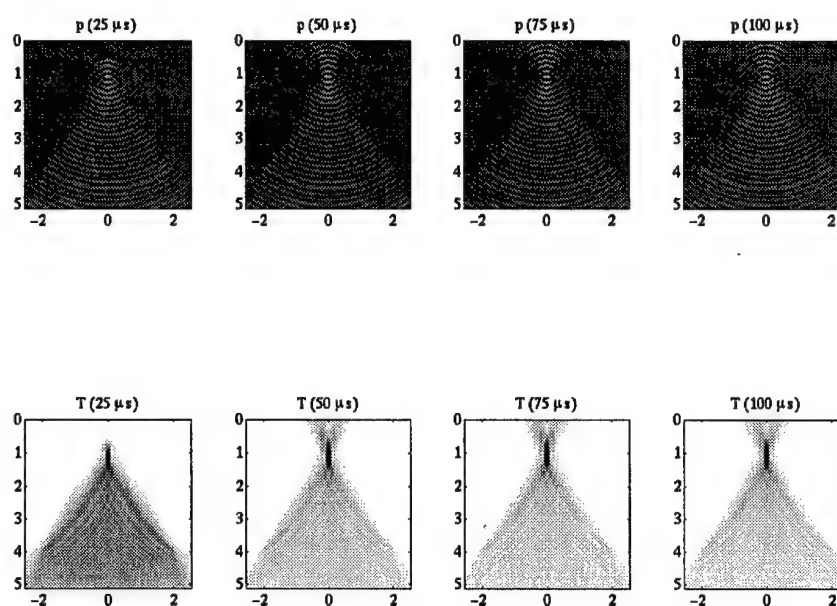
Figure 5.10: Pressure and temperature snapshots for a pulse which is long enough so that the acoustic field reaches steady state on the computational domain. Axes labeled in cm.

pulse was long enough to attain time-harmonic steady state acoustics we plot an axial slice through the pressure field at 50, 75, and 100 μs in Figure 5.11. The pressure field slices are congruent at these times, indicating that the snapshots were taken at integral multiples of a period and are at steady state. Figure 5.11 also shows temperature along the transducer axis rising with insonation time, achieving a value of 1
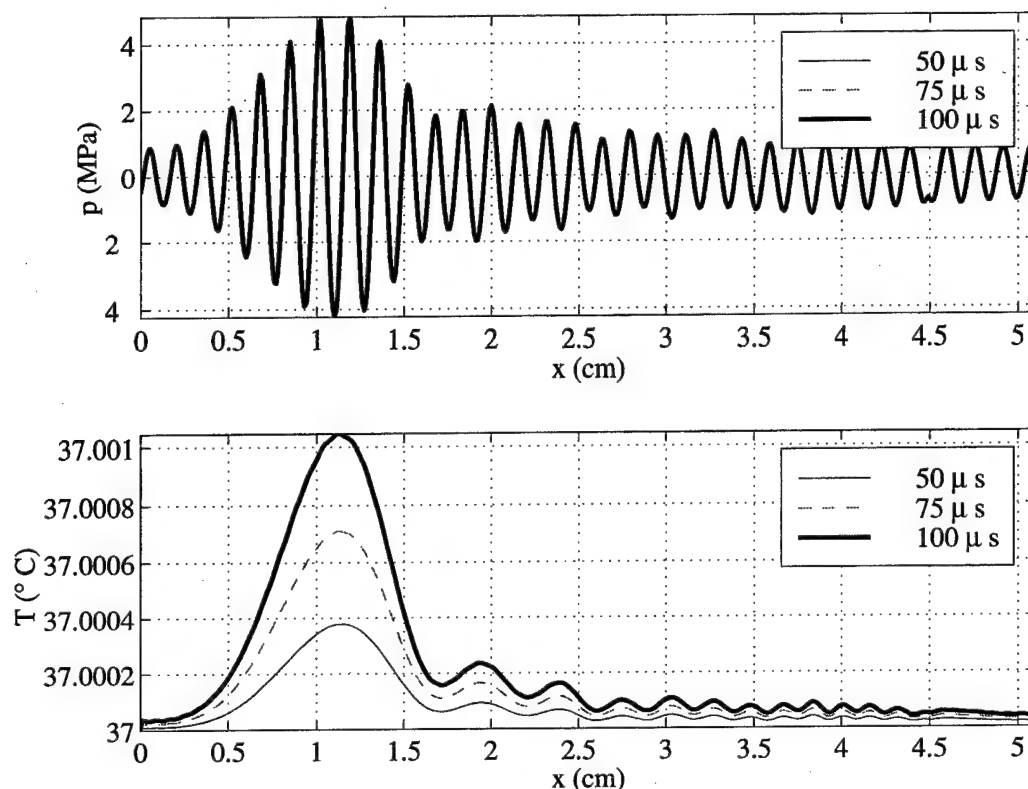
Figure 5.11: Pressure and temperature slices along the transducer axis taken at 50, 75, and 100 μs. Pressure is at steady state, while temperature continues to rise with insonation time.

mK above background after 100 μs. The linear rate of temperature rise is consistent with the steady state conditions.

Typically the FDTD time step size for acoustic calculations at 1 MHz is on the order of 10 nanoseconds. Thus it is not practical to obtain results for a 10 s insonation by running the basic acousto-thermal code until 10 s are reached (this would require approximately two years of execution time using current computers!). Since the thermal problem occurs on a much slower time scale, it is not necessary to continue acoustic field calculations once a time-harmonic steady state is achieved. Coarser time gridding is used to advance the calculations of the temperature field. To obtain the

temperature for insonations much longer than the acoustic simulation would permit, we integrate the heat deposited from the CW acoustic field over one period, then we assume that this heat deposition pattern remains unchanged (this assumption will be relaxed later) for the remainder of the insonation. The temperature field is calculated using the bioheat equation in a separate FDTD program using a much larger time step (about 10 μs) which can proceed to calculate results for insonations of several seconds in about 10 minutes of execution time using current machines. Thus knowledge of the CW pressure field allows extrapolation to calculate the heating for much longer times, on the order of several seconds for therapeutic applications.

The method for calculating the CW heat deposition term consists of integrating the heat deposition field in time for one acoustic cycle having period τ_a, after steady state is reached,

$$Q(\mathbf{x})_{\text{acoustic cycle}} = \int_{t_0}^{t_0+\tau_a} Q(\mathbf{x},t)\ \mathrm{d}t, \tag{5.23}$$

where t_0 is great enough to achieve a time-harmonic steady state acoustic field on the computational domain. Subsequent FDTD calculations of the bioheat equation can then use a larger time step than that used in the pressure calculations, and the rate of heat deposition used in the bioheat calculations $Q(\mathbf{x})_{bioheat}$ has the same spatial distribution, but has magnitude

$$Q(\mathbf{x})_{\text{bioheat}} = Q(\mathbf{x})_{\text{acoustic cycle}} \frac{\delta_{t\text{bioheat}}}{\tau_a}, \tag{5.24}$$

where $\delta_{t\text{bioheat}}$ is the timestep used for the bioheat equation solver.

The 10 s time trace of the temperature at the geometric focus of the source is shown in Figure 5.12, where the insonation lasted for 5 s followed by a cooling time of 5 s. The simulation assumes tissue parameters for soft tissue as listed in equation (5.20). The spherical section bowl transducer emits a 1 MHz field at 1 MPa source pressure. The aperture of the bowl is 4 cm and the radius of curvature is 3 cm.

At this point it is appropriate to examine the bioheat equation (5.1) again for
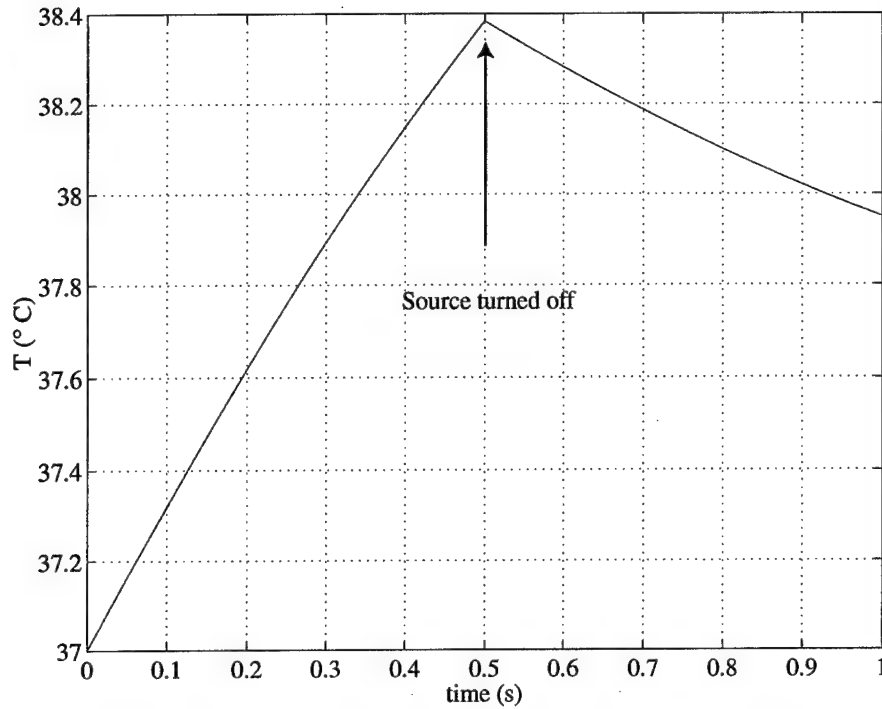
Figure 5.12: Temperature at the geometric focus due to a 10-second simulation for a 1 MHz bowl source at 1 MPa in soft tissue. The source was ON for 5 seconds, followed by 5 seconds with the source OFF.

insight into the individual terms. We rewrite the bioheat equation here for convenience

$$\frac{\partial T}{\partial t} = \frac{K_{\text{tiss}}}{\rho C_{\text{tiss}}} \nabla^2 T - \frac{W_b C_b}{\rho C_{\text{tiss}}} (T - T_a) + \frac{Q_{\text{bioheat}}}{\rho C_{\text{tiss}}}. \tag{5.25}$$

A number of effects are represented in (5.25). The driving source for the heating of the tissue is Q which is a function of space only for steady heating in quiescent media. The other terms (from left to right) represent temperature rise, conduction due to the spatial gradient of temperature, and perfusion due to the elevation in temperature above the ambient temperature, $T_a = 37°C$. Figure 5.13 shows results from a 1-second simulation using the same bowl source described in the previous paragraph. The source is on for 0.5 seconds and turned off for the remaining 0.5 seconds. The figure plots the temperature at the location of the transducer focus

under three conditions:
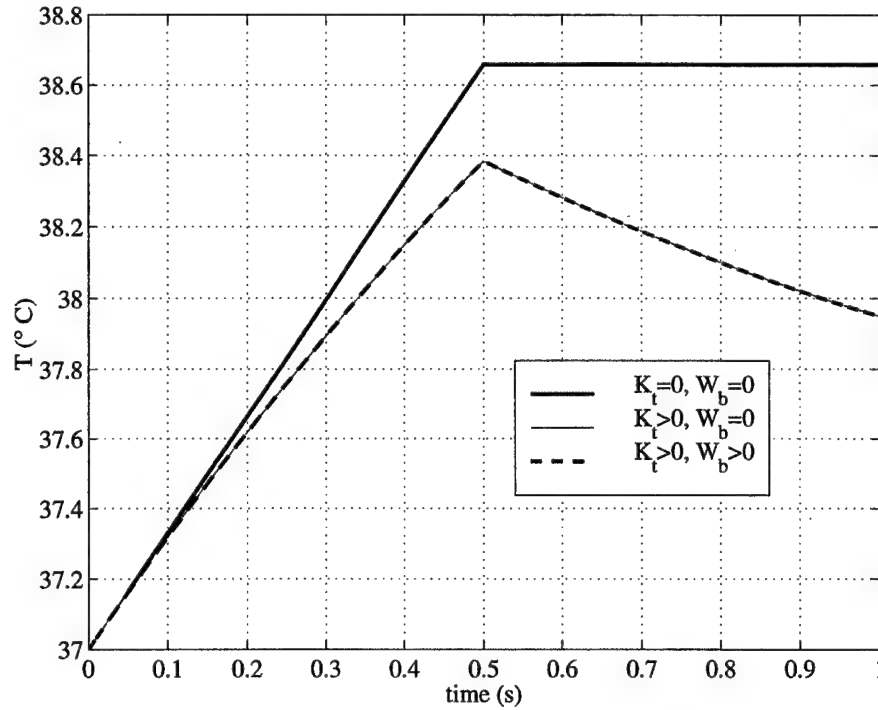
Figure 5.13: The time trace of temperature at the focus for a 0.5 s on then 0.5 s off insonation. The traces show the effect of conduction K_{tiss} and perfusion W_b on temperature.

1. $K_{\text{tiss}} = W_b = 0$: In this case no conduction or perfusion are simulated, and the only effect is due to heating by the source Q. The bioheat equation is thus reduced to the linear relation

$$\frac{\partial T}{\partial t} = \frac{Q}{\rho C_{\text{tiss}}}.$$ (5.26)

We see for this case that the temperature rise is linear, with a slope of $Q/(\rho C_{\text{tiss}})$, and that no cooling occurs after the source is extinguished. In other words, if integrated once over time τ

$$T(\tau) = T_a + \frac{Q}{\rho C_{\text{tiss}}}\tau.$$ (5.27)
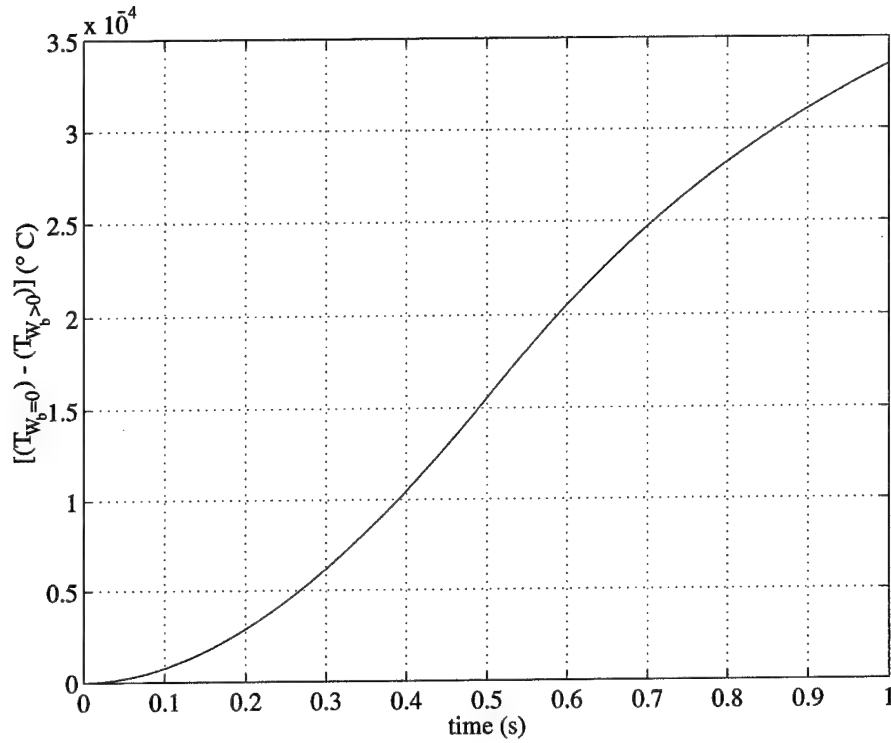
Figure 5.14: Temperature difference between the focal temperature with and without considering perfusion. An inflection point in the curve at 0.5 s indicates where $(T - T_a)$ stops increasing and starts decreasing.

2. $K_{\text{tiss}} > 0, W_b = 0$: If conduction is taken into account, but not perfusion, we see a nonlinear profile to the temperature of the hot spot in Figure 5.13. The conduction term acts to remove some of the heat from the immediate vicinity of the focus during and after the insonation. K_{tiss} used was $0.6 W/(m \cdot K)$.

3. $K_{\text{tiss}} > 0, W_b > 0$: For the case where both conduction and perfusion are taken into account, we see a curve almost identical to that for the $K_{\text{tiss}} > 0, W_b = 0$ case. However, to look at whether the perfusion has any effect on

the temperature profile we plotted the difference between the focal temperature with and without perfusion. The result is shown in Figure 5.14 and shows that indeed there is a small effect attributable to perfusion. Figure 5.14 indicates that the perfusion effect becomes increasingly important as the temperature rises above ambient temperature, because the perfusion term contains the factor $(T - T_a)$. W_b results from heat exchange from the heated tissue to the ambient blood flow network, assumed uniform in the tissue. The value used for W_b was $0.5 kg/(m^3 \cdot s)$.

5.6 Therapeutic Ultrasound in Nonlinear Time-Varying Tissue: CW Simulations

A model for propagation of finite amplitude ultrasonic waves in nonlinear, absorbing, time-varying background (TVB) media was presented in Chapter 2. Numerical simulations using the FDTD method are used to investigate the thermal and acoustic effects from focused transducers in media with TVB sound speed and attenuation coefficient.

The motivation for these simulations is the experimental data showing the temperature-dependence of c_0 and α_0 [4, 17]. The data measured by Bamber and Hill and by Damianou, *et al.* are adapted for the present study by using one data point per 5°C between 30°C and 90°C. The results are shown in Figure 5.15 along with polynomial fits to the data. The polynomial used to fit the sound speed to the data is

$$c(T) = 1466 + 8.43T - 0.167T^2 + 1.27 \times 10^{-3}T^3 - 3.33 \times 10^{-6}T^4 \ \text{m/s}. \quad (5.28)$$

The polynomial used to fit the absorption coefficient to the data is

$$\begin{aligned} \alpha(T) = &-43.8 + 6.24T - 0.303T + 7.06 \times 10^{-3}T^2 - 8.39 \times 10^{-5}T^3 \\ &+ 4.91 \times 10^{-7}T^4 - 1.12 \times 10^{-9}T^5 \ \text{Np/m}. \end{aligned} \quad (5.29)$$
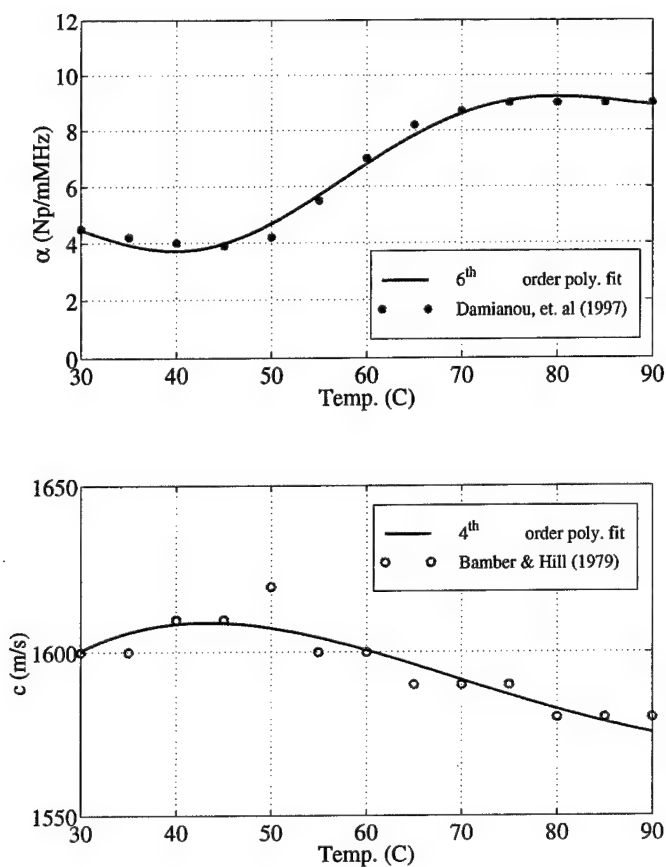
Figure 5.15: Temperature dependence of sound speed and absorption coefficient in soft tissue taken from published laboratory measurements (symbols) and the corresponding polynomial fits to the data (solid).

Caution should be exercised not to extrapolate the polynomials outside the region of fitting, as they only model the data inside the interpolation regions, here 30°C to 90°C.

These data imply that during the course of a single focused ultrasound treatment tissue properties will change and quite significantly for the absorption coefficient α_0 if temperature exceeds 60°C. Data for other properties such as nonlinearity coefficient and density are not available. The temperature-dependence of α_0 implies the rate of

heat deposition will also be temperature (and time) dependent, since the heating rate is directly proportional to the absorption coefficient.

To estimate the importance of the TVB behavior on the acoustic waves, we used order of magnitude estimates in section 2.5.2 to obtain the relative magnitudes of the TVB terms in the TVB wave equation (2.56) compared to the other terms in the wave equation. For tissue insonated by a 1 MHz bowl source of 2 cm aperture, having a source pressure of 1 MPa, we concluded that for the range of parameters of interest, the time variation in the tissue background properties is not important at the acoustic time scales. In other words, we formally demonstrated that the slow TVB effects (temperature dependence with time scales of 1 s) are too slow to affect the acoustic waves having time scales on the order of 1 μs.

One may be inclined to conclude that the previous paragraph implies that the TVB is not a factor in acoustic applications of ultrasound. This is however untrue, since a typical treatment does occur over a span of several seconds at the least, to achieve a useful temperature rise. Thus the variation in the background acoustic properties of the tissue should be taken into consideration for insonations with durations comparable to the thermal time scales. In this chapter we will show the results of simulations which couple the acoustic and the thermal behavior of tissue to see what the effect on overall heating is.

5.6.1 An Example of TVB Behavior

Now we look at one case where the background sound speed and attenuation coefficient are allowed to vary in time according to the temperature of the tissue as a function of space and time. In this case the sound field can be expected to change with both the thermal time scale as well as the acoustic time scale. Specifically, as temperature increases in the focal region, we can expect the rate of temperature rise to increase because the driving term in the bioheat equation is dependent on α, which is monotonically increasing with temperature. In fact, a doubling of the attenuation

coefficient appears to be possible over the period of a hyperthermia treatment of several seconds duration. This is because the temperature range up to 70°C and higher is possible with an insonation of a few seconds from a typical laboratory hyperthermia focused source.
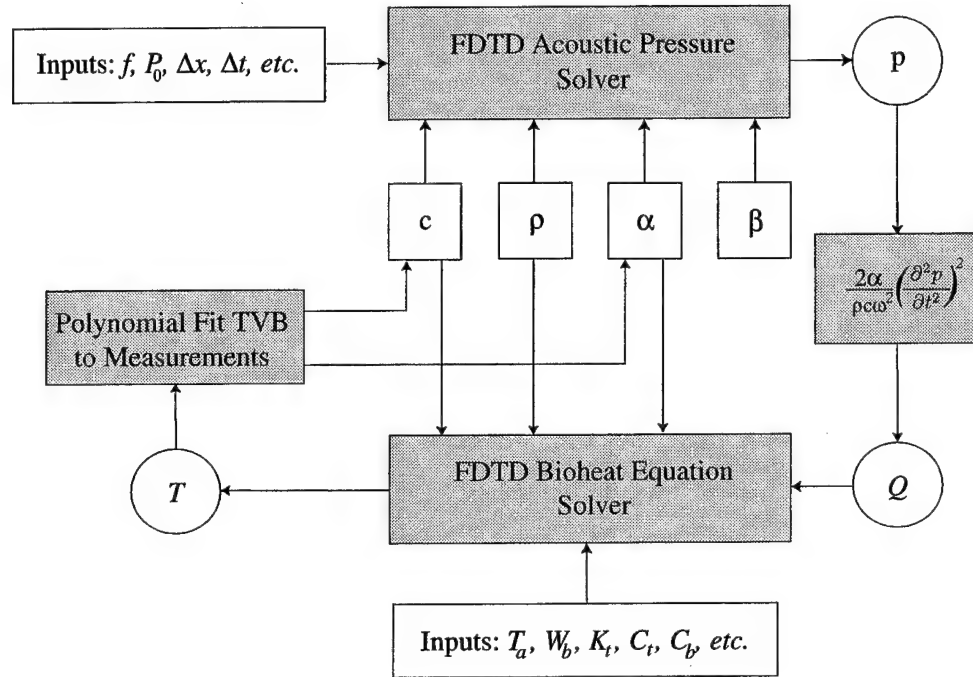
Figure 5.16: Flowchart showing the iterative method for coupling the pressure and temperature calculations in the TVB simulations.

The flowchart in Figure 5.16 shows how the acoustic and the thermal solvers were coupled for the TVB computations via the CW heating term Q as before. Periodically (at 1 s intervals) the thermal solver is made to output updated background properties of the tissue to data files. The sound speed and attenuation coefficient are updated using the polynomial fitting routine derived from the laboratory measurements of the temperature-dependence of c and α. The updated c and α are then used as inputs to the acoustic solver to calculate a new pressure field, and a new Q field, and so on in an iterative fashion. Thus the pressure field, which drives the heating, is in turn
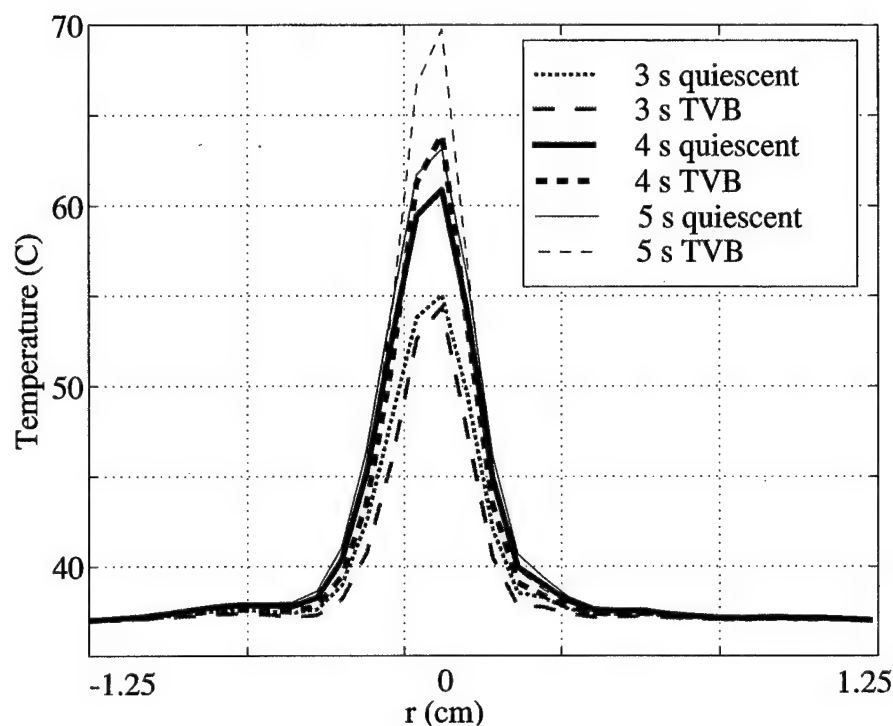
Figure 5.17: Temperature profiles across the axis in the focal plane at 3, 4, 5 s, showing increased heating in the TVB case.

affected by the temperature field. The temperature's effect on α can be particularly important in hyperthermia applications.

In Figure 5.17 we show slices across the axis of a bowl transducer as they evolve in time for quiescent and TVB simulations. Note that at 3 s the TVB case results are close to the quiescent results, or even a little lower in temperature. The reason is that at 3 s the temperature is about 55°C, and at this temperature the absorption coefficient has dropped slightly compared to that at 37°C. As the insonation time increases, the temperature exceeds 60°C, where there is a dramatic increase in α. In this case the temperature from the TVB simulation is higher than that from the quiescent simulation. This result can be explained if we look at the profile of the
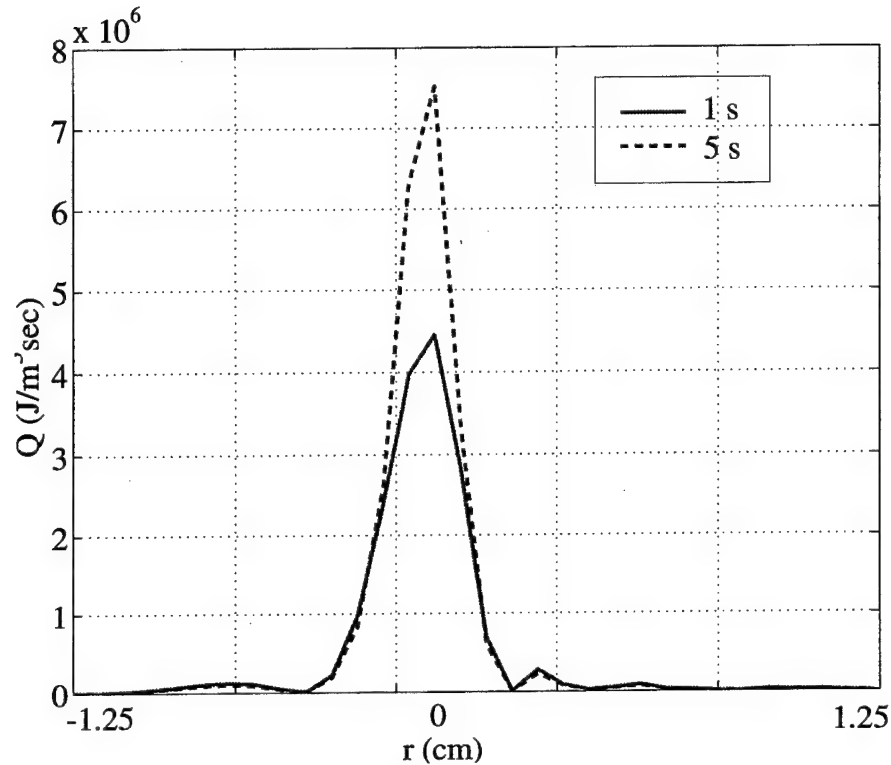
Figure 5.18: Slices of Q taken across the axis at the focal zone at 1 s and 5 s for the TVB case. A dramatic increase in the heat deposition rate Q can be observed if the attenuation coefficient (directly proportional to Q) is included in the simulation. Q would be steady for quiescent simulations.

driving source term Q in the bioheat equation as it evolves in the TVB case. Figure 5.18 shows the Q profile across the transducer axis in the focal plane at 1 s and 5 s. Q increases due to the increase in α with temperature. The direct proportionality between α and Q is responsible for the added heating noted at the focus.

5.7 Conclusions

This chapter explored several facets of focused ultrasound surgery in soft tissues using modeling and numerical simulations. The techniques developed in earlier chapters for

modeling acoustic sources and fields was coupled to the bioheat equation through the acoustic energy deposition driving term in the bioheat equation. Various effects were studied including the effect of finite-amplitude propagation, inhomogeneity contrast, and slow TVB variation in temperature-dependent tissue.

We showed that finite-amplitude propagation leads to enhanced heating. Because absorption in lossy media is monotonic with frequency, a waveform containing higher-frequency harmonics is absorbed more readily than one containing only the lower-frequency fundamental. This result is not new, but was confirmed here for focused sources in tissue-like media using the FDTD simulations. The amount of excess heating in finite-amplitude situations over linear ones depends on the same factors governing the generation of harmonics: propagation distance to target, source frequency and amplitude, and nonlinearity coefficient of the tissue. For the example used in this study, the nonlinear temperature elevation was about up to 1.8 times that of the linear case for similar insonations from a short pulse.

Inhomogeneity contrast about a mean value was studied because of its effect on the profile of the acoustic beam and the resulting distortion of the hot spot near the focus. The present study used a tissue inhomogeneity model derived from laboratory measurements using human tissue samples [43]. It was found that while increasing the percent inhomogeneity contrast does not affect the overall thermal energy deposition in the extended tissue sample (a statement of conservation of energy). However, the peak temperatures in the computational domain increased monotonically with percent inhomogeneity contrast. We hypothesize that the cause for this is local lensing of the acoustic field, and accompanying local heating due to the inhomogeneity result when small-scale inhomogeneities are inserted in the propagation path. The peak local temperature excursions can have implications for safety studies of FUS devices. Severe inhomogeneities, such as obstruction by bone, vasculature, bladders, or bubble clouds can have dramatic effects on the acoustic and temperature fields due to reflections and scattering from the obstruction.

Finally, when the effect of temperature-dependence on tissue sound speed and attenuation coefficients was taken into account (TVB simulations), increased heating near the focus was observed. It has been observed in the laboratory that the attenuation coefficient of soft tissue is approximately monotonically dependent on temperature [17] between 30°C and 90°C, with the absorption coefficient nearly doubling between 50°C and 70°C. This effect will cause an increase in the rate of heating in the regions near the focus of a FUS device. The present study shows that since the heating rate is directly proportional to the absorption coefficient, slow TVB effects need to be accounted for in modeling and simulating FUS treatments.

Chapter 6

CONCLUSIONS

This dissertation addressed issues associated with forming a high-amplitude focus using arrays and extended focused sources in various propagation media. Specifically, we addressed the problems which may face time reversal focusing in the presence of debilitating effects such as phase jitter, absorption, and nonlinearity. Further, the behavior of focused sources used for tissue heating in biomedical applications was examined in the presence of nonlinearity, inhomogeneity, and time-varying medium properties. These studies were conducted under the umbrella of finite-amplitude acoustic models and associated numerical simulation codes.

The practical applications of acoustics and ultrasonics in medical, industrial and military uses are almost completely restricted to two classes of applications:

1. Nondestructive diagnostic and imaging applications. Diagnostic medical imaging with ultrasound, nondestructive testing of materials (NDT), and communications and surveillance are examples of this use.

2. Applications requiring focused, high-intensity sound for the purpose of affecting physical change to the objects insonated near the focal spot. Examples are focused ultrasonic surgery, ultrasonic welding of plastics, and mine neutralization.

This dissertation deals with the latter use for acoustic arrays and focused sources in underwater and biomedical applications. Several topics in linear and nonlinear acoustic focusing were studied, with emphasis on the evaluation of the focusing characteristics of time reversal arrays (TRA's) and therapeutic hyperthermia sources for focused ultrasound surgery (FUS).

Two recently-proposed applications for acoustic arrays and focused sources are high-intensity time reversal arrays and focused hyperthermia applicators. The underlying concepts for the operation of these devices are reasonably well understood. However, both of these technologies in their current forms are relatively recent additions to the arsenal of underwater and biomedical engineers, and until now they have not become commercially viable. We now examine the background and the contributions of this dissertation to each of the main problems addressed in this study, as well as future directions for the use of TRA's and FUS sources.

6.1 Time Reversal Arrays

6.1.1 Motivation for the TRA Study

The advent of digital data aquisition and computer-controlled transducer arrays allowed scientists to realize the acoustic phase conjugate mirror, or time reversal array. The device allows for automatic phase correction at the array to produce a focus at the location of a scatterer in an unknown inhomogeneous medium containing arbitrary multipath and multiple scattering. The technique relies on the stationary medium providing a matched filter for the propagation of acoustic waves from and to an illuminated scatterer, even if the nature of the propagation path is not known. The technique is superior to conventional time-of-flight initial delay focusing because it captures the initial delay information as well as detailed waveform distortion information from all propagation paths, and corrects for both using the medium as a spatial-temporal filter. The technique was hailed as a true advance in imaging and focusing applications because it permitted the phase correction due to unknown extended inhomogeneities rather than just a thin phase aberrating layer near the array. One intriguing aspect of time reversal array technology is the promise of devices that can direct intense acoustic energy onto one or more scattering targets. The idea is to deposit sufficiently intense fields onto the targets to cause permanent physical change

or destruction. This idea could be useful for accurate targeting and destruction of kidney stones, or for remote mine neutralization at sea.

Currently, the most successful means for removal of kidney stones involves imaging with X-rays, then placing the patient and the stone in a coupling water bath at the focus of a lithotripter source. The lithotripter machine then fires hundreds of shots (focused shock waves) at the stone. While lithotripsy is effective and is in wide use, several problems plague lithotripters and reduce their effectiveness. The targeting requires the use of X-ray radiation to locate the stones. In addition, the targeting assumes that the propagation path is a homogeneous medium, and thus both the position of the focus and the shape of the beam will suffer from variations in the index of refraction resulting from the propagation through the human body and the body-water interface. Finally, the stone is assumed to remain stationary for the duration of the treatment, or for a portion of the treatment between repositioning. It is thought that a large percentage of shots fired at a kidney stone miss their intended target due to breathing motion and other targeting errors [67].

Using time reversal arrays has been suggested as a means of targeting kidney stones that can correct for the unknown refractive index variations in the patient's body. Iterative use of the time reversal method can track moving scatterers and maintain the focus of the array on a kidney stone in a breathing patient. The next step in the process involves amplifying the array outputs to send high-amplitude pulses, or shock waves, toward the kidney stone for the destruction phase. This is repeated, always targeting the brightest scatterer until the procedure is complete. The concept has been successfully demonstrated in the laboratory for low amplitudes [67]. A similar technique was proposed for the remote neutralization of mines in a shallow water channel, and the proposed solution was similar to that intended to destroy kidney stones.

Ideally, time reversal systems will operate very effectively to focus onto their targets according to theory. However, in real applications we will encounter problems

that will degrade the effectiveness of the TRA's as focusing implements. These factors that compromise a time reversal system's performance are called *debilitating factors* in this dissertation. Several debilitating factors are considered in this study. These include imperfect initial phasing of the TRA, absorption, and nonlinear propagation.

The arrival times for different propagation paths in a time reversal channel can be adversely affected if jitter exists in the recorded or the retransmitted signals from the array elements. This study looks at the quantitative effect of this jitter as a debilitating factor.

Absorption in the propagation medium will degrade the performance of time reversal focusing systems. This is because the absorption term in the wave equation contains odd-order time derivatives, which are not invariant under time reversal. This has unfortunate implications for high-intensity time reversal systems, and thus absorption is studied as a debilitating factor. This is especially important for high-amplitude applications.

In order for high-amplitude time reversal systems to be realized, we must reexamine the assumptions and the mathematics of the phase-conjugate arrays with finite-amplitude acoustics taken into consideration. As source amplitude and propagation distance increase, energy is transfered from the lower frequency fundamental into higher frequency harmonics due to nonlinearity. In fluids the energy loss is invariably higher for higher frequencies. The result is an overall loss of focal spot pressure amplitude when finite-amplitude time reversal is used in lossy media. For applications requiring high acoustic pressures at the focus like those described above, this means that a finite-amplitude time reversal system will not be as efficient as a linear one. This dissertation explores this degradation in a quantitative way, and uses simulations to provide evidence of the extent of the degradation as a result of the debilitating factor: finite-amplitude propagation.

In order to get an idea of how well we may expect real time reversal systems to perform for underwater and biomedical applications, this dissertation examined the

operation of time reversal arrays under nonideal conditions, *i.e.* in the presence of the debilitating effects above.

6.1.2 Contributions Made to the TRA Problem

Errors in the initial phasing of time reversed signals can occur if the electronics of the time reversal system (aquisition, storage, signal processing) are of poor resolution. Depending on the frequency and bandwidth of the signals, errors in phasing at the array can result in loss of focusing by a TRA. Jitter in the retransmitted phases of the time reversed signals was found to be tolerable up to about one-eighth to one-sixth of a fundamental period, beyond which a loss of focus occurs [41]. This is corroborated by studies of time-delay phased arrays by other researchers [70, 62], but the present study looked explicitly at the effect of jitter in time reversal applications.

Absorption in the propagation medium is a serious factor in degrading the ability of TRA's to place an intense focus at the desired target location. This is only partially due to the loss of acoustic energy in the linear absorption in the thermoviscous medium. What makes absorption a debilitating factor for TRA's is the fact that the absorption term in the wave equation causes a violation of time reversal invariance. The wave equation will no longer have twin solutions (forward time and backward time solutions). As a result, the overall ability of a TRA to form a sharp intense focus is reduced. This has been known to be the case in absorbing media, but this study presented formal analysis of the wave equation for thermoviscous fluids showing the cause for the time reversal invariance violation, along with examples of this effect in simulations of TRA's for biomedical applications.

While absorption is found to be a debilitating factor for time reversal arrays. This study used propagation through a model section of the human skull and brain as a tool to examine the effects of absorption in the skull bone layer on a TRA placed in water outside the subject's head. It was found that for the pulse used in this study a marked reduction in focal amplitude and an increase in full-width-at-half-maximum

occurred.

The operation of a time reversal array was re-examined using the nonlinear absorbing wave equation as a model for wave propagation. It was shown that the nonlinearity in itself is not responsible for degrading the performance of TRA systems. Only when combined with absorption in the medium or amplification at the array were finite-amplitude TRA systems adversely affected. It was shown analytically that the extra absorption loss due to high frequency content of shocked waveforms in nonlinear TRA's can have a very detrimental effect on the efficiency of a focusing system using TRA's. A source-target separation of more than one to two shock formation distances was found to lead to a reduction of the peak pressure amplitude at a TRA focus to a fraction of that expected from linear propagation alone in a similar linear medium. Furthermore, if the amplitude of the received signal was altered at the array (amplified for example) nonlinear TRA's would suffer a performance penalty because the exact replication of the received waveform (time-reversed) is a condition for perfect phase conjugation. This amplification at the array, which is commonly assumed for proposed applications in underwater and biomedical applications, is a violation of time reversal invariance and is a debilitating effect.

6.2 Therapeutic Ultrasound: Focused Ultrasound Surgery

6.2.1 Motivation for the FUS Study

The use of focused ultrasound sources to deposit thermal energy for therapeutic biomedical applications (hyperthermia) was also investigated in this dissertation. Much promise for treatment of deep-seated tumors has been evidenced by *in vitro* and *in vivo* experiments in the last decade using focused transducers operating in the megahertz frequency range [47, 65, 63]. The absorbing tissue acts to convert acoustic energy to thermal energy, inducing a temperature rise. The temperature rise near the focus can kill living cells via *necrosis* by exceeding the thermal dose threshold

associated with cell death. While the basic operation of hyperthermia devices is understood, and models exist to predict the behavior of the acoustic and thermal fields of such devices, some aspects of high-intensity focused surgery systems still require further study in order to be made into viable medical systems. This dissertation examines the behavior of focused ultrasonic surgery systems through numerical simulations and modeling. Key aspects of ultrasound focused surgery such as the heating from finite-amplitude sources, the heating in inhomogeneous tissue-like media, and the heating of time-varying tissue were studied.

It is known that increased tissue heating will occur from high-amplitude focused sources due to the higher harmonic content of the acoustic field near the focus. The higher frequency content in shocked waveforms deposit more energy in the absorbing tissue because of the frequency dependence of the absorption term in the wave equation. Predictions of heating based only on linear field calculations in homogeneous media are common in hyperthermia research, and a good balance between clinical utility and well-founded theoretical physical acoustics is required for the next-generation simulations of hyperthermia systems.

One aspect of propagation in real tissues that plays an important role in hyperthermia is the presence of inhomogeneities in the background properties of soft tissue and other organs in the body. Spatial variation in the propagation medium properties alter the exact shape and location of the acoustic and thermal hot spots. Most current hyperthermia research is conducted under controlled conditions using soft tissue where the effects of propagation uncertainties are minimized. Realtime measurement of such inhomogeneities for case-specific correction would require sophisticated imaging techniques in order to faithfully capture the nature of the inhomogeneity, as well as powerful computational abilities. This is especially important if passing acoustic beams through regions of high inhomogeneity contrast, or severe inhomogeneities such as bone, vasculature, bladders, or gas pockets, in which case the passage of sound may be obstructed outright and scattered to unexpected locations.

Another important feature of tissues is the way that they respond to heating. Perfusion, the adaptive cooling of bulk tissue by blood flow, is temperature dependent, and makes for a challenging control problem. More important is the behavior of temperature-dependent background propagation properties. The sound speed and absorption coefficient have been measured to be a function of temperature, so the position and shape of the focus will vary in time as the tissue is heated. For accurate simulations of bioacoustics problems, other acoustic and thermal properties' characteristics should be measured to be included in the calculations. At this time most properties have only been reported for body temperature conditions.

6.2.2 Contributions Mode to the FUS Problem

Simulations of the spatial and temporal evolution of the pressure and temperature fields from hyperthermia sources were presented. The calculated pressure field was then used to determine the local heating due to absorption. This heating was used as a source term in solutions of the transient bioheat equation. Simulations for finite-amplitude FUS sources were performed, and the results compared to similar sources in a linear medium. Enhanced heating depended on the source pressure, amplitude, frequency, and geometry, as the generation of harmonics depends on these factors. In simulations performed for this research the heating could be increased by a factor of 1.5 to 3 in comparison to predictions by linear models.

We demonstrated that inhomogeneities in the propagation medium's background parameters lead to local distortion of the acoustic beam, and a resulting distortion of the heating pattern calculated for the homogeneous (zero contrast) case. The simulations used spatial distribution data for real human tissue properties found in the literature. This study found that the overall heat deposited by a beam in an inhomogeneous medium with zero-mean-plus-average inhomogeneities is the same for any amount of inhomogeneity contrast. This is a statement of conservation of energy, since the acoustic energy loss to heat will be the same, but merely redistributed in space.

The peak temperatures observed however monotonically increased with inhomogeneity contrast. That is to say, as inhomogeneity contrast was increased, higher and higher values of peak local temperature were observed in the computational domain. Given the previously-mentioned conservation statement, this implies that other locations underwent less heating. This finding has implications for safety studies, where the peak temperature excursions are of concern, as well as for applications where raising the temperature sufficiently to ensure complete necrosis is required at all locations in the region of interest.

Finally, the coupling of pressure and temperature calculations was carried out with a slow-scale TVB tissue simulation. The tissue was assumed to change its background sound speed and attenuation coefficients in accordance with published measurements for these quantities. A polynomial fit to the reported data was used to periodically update the initial condition data files containing the sound speed and the attenuation. This new data was then fed into the pressure solver program to compute an updated acoustic field. This interdependence of heating on acoustic pressure and acoustic pressure on temperature formed a feedback loop that dramatically altered the temperature predictions for a hyperthermia system. The fact that the attenuation coefficient had a monotonically increasing dependence on temperature, and the fact that heating rate is directly proportional to absorption coefficient implies an acceleration in the rate of temperature rise for a system with slow TVB feedback. The absorption coefficient can double over the span of a hyperthermia treatment session, thus doubling the heating rate for the same acoustic field. Results confirmed that as temperature increased near the hot spot, the disparity between the cases where TVB was and was not taken into account grew in magnitude.

6.3 Other Contributions

This dissertation has made original contributions to the study of finite-amplitude propagation in inhomogeneous thermoviscous time-varying background (TVB) media. Starting from the equations of fluid mechanics, the nonlinear absorbing wave equation in inhomogeneous thermoviscous fluids was derived for the case having time-varying background (TVB) parameters. This wave equation was studied in depth and nondimensionalized to elucidate the significance of the TVB, and the regimes of operation which would require consideration of the TVB wave equation.

Simulations were carried out using original computer codes capable of representing the physics appearing in the wave equation. Finite-difference time-domain (FDTD) simulations allowed detailed study of the spatial and temporal behavior of the systems under consideration, and were especially helpful in capturing the essence of the behavior of the focal zone.

6.4 Summary

Despite having a good foundation for understanding the workings of time reversal systems and acoustic hyperthermia processes, this research reports on some important new findings. In the case of time reversal arrays, nonlinear effects were shown to have a serious debilitating effect on the ability of a TRA to form an intense focus at the desired location. Absorption and amplification of the time reversed signal at the array were shown through analysis and simulation to be detrimental to the TRA performance. Jitter in the time reversed signal was also shown to gradually erode the sharpness of the focus of a TRA system in an underwater channel. Future research involving laboratory measurements for finite-amplitude time reversal systems would complement these findings, and given the limitations of the numerical tools available, perhaps the measurements could extend the results to higher Gol'berg numbers and for greater distances than those simulated in this study. The simplest form of a TRA,

a one-dimensional two-element case, was used for this study. It would be informative to use real multi-dimensional arrays in a laboratory study. Time reversal lithotripsy systems should be investigated in the laboratory under finite-amplitude conditions to evaluate their performance. Time reversal mine-hunting systems appear to be unlikely to yield a real device capable of destroying today's mines. This is not due to a deficiency in the targeting or location of the mines, but due to the enormous acoustic pressures that would be required to cause mine neutralization. Such high pressures are currently unobtainable using time reversal arrays.

For hyperthermia, an original numerical simulation tool was designed and used to study the effects of nonlinearity, inhomogeneity, and time-varying background coupling between the acoustic and the thermal fields. The temperature of the hot spot was found to be enhanced by nonlinear generation of higher-frequency harmonics as expected from results found in modern literature on the subject. Effects of tissue inhomogeneity were studied, where an overall conservation of thermal deposition of energy was observed, but an increase in the peak local temperature was observed for the inhomogeneous media. Finally, a coupling of the acoustic and thermal response of tissue was taken into consideration. A feedback relation between acoustic and temperature fields was obtained, with a resulting increase in the absorption coefficient and temperature. A lack of measured data for tissue properties as a function of temperature was encountered. This study used the available data for sound speed and absorption coefficient, but measurements of the temperature-dependence of the other acoustic and thermal properties of tissue would be very helpful to future modelers, and could perhaps be combined with simulation tools to provide realtime FUS treatment planning on a case-specific basis.

BIBLIOGRAPHY

[1] A. L. Anderson and L. D. Hampton. Acoustics of gas-bearing sediments i: Background. *J. Acoust. Soc. Am.*, 67:1890–1903, 1980.

[2] M. A. Averkiou, L. A. Crum, V. A. Khokhlova, and O. V. Rudenko. *Nonlinear waveform distortion and energy attenuation of intense acoustic waves in biological tissue, in Proceedings of the World Congress of Ultrasonics, Part I*. Berlin, Germany, 1995.

[3] D. R. Bacon and E. L. Carstensen. Increased heating by diagnostic ultrasound due to nonlinear propagation. *J. Acoust. Soc. Am.*, 88(1):26–34, 1990.

[4] J. C. Bamber and C. R. Hill. Ultrasonic attenuation and propagation speed in mammalian tissues as a function of temperature. *Ultrasound in Med. and Biol.*, 5:149–157, 1979.

[5] L. M. Berkhovskikh and Y. P. Lysanov. *Fundamentals of Oc Acoustics, Second Edition*. Springer-Verlag, 1991.

[6] R. T. Beyer (ed.). *Nonlinear Acoustics*. Naval Sea Systems Command, Washington, D.C., 1974.

[7] D. T. Blackstock. Thermoviscous attenuation of plane, periodic, finite-amplitude sound waves. *J. Acoust. Soc. Am.*, 36:534–542, 1964.

[8] J. L. Buchanan and P. R. Turner. *Numerical Methods and Analysis*. McGraw-Hill, Inc., 1992.

[9] M. D. Cahill and A. C. Baker. Numerical simulation of the acoustic field of a phased-array medical ultrasound scanner. *J. Acoust. Soc. Am.*, 104(3):1274–1283, 1998.

[10] E. L. Carstensen, N. D. McKay, D. Delecki, and T. G. Muir. Absorption of finite amplitude ultrasound in tissues. *Acustica*, 51:116–123, 1982.

[11] L. Chen, G. ter Haar, C. R. Hill, S. A. Eccles, and G. Box. Treatment of implanted liver tumors with focused ultrasound. *Ultrasound in Med. & Biol.*, 24(9):1475–1488, 1998.

[12] W. C. Chew and Q. H. Liu. Perfectly matched layers for elastodynamics: A new absorbing boundary condition. *J. Comp. Acoust.*, 4(4):341–359, 1996.

[13] R. O. Cleveland. *Propagation of Sonic Booms Through a Real, Stratified Atmosphere.* Ph.D. Dissertation, University of Texas, Austin, 1995.

[14] M. G. Curley. Soft tissue temperature rise caused by scanned, diagnostic ultrasound. *IEEE Trans. Ultrason. Ferroelec. Freq. Contr.*, 40(1):59–66, 1993.

[15] C. A. Damianou, K. Hynynen, and X. Fan. Evaluation of accuracy of a theoretical model for predicting the necrosed tissue volume during focused ultrasound surgery. *IEEE Trans. Ultrason. Ferroelec. Freq. Contr.*, 42(2):182–187, 1995.

[16] C. A. Damianou, K. Hynynen, and X. Fan. Evaluation of accuracy of a theoretical model for predicting the necrosed tissue volume during focused ultrasound surgery. *IEEE Trans. Ultrason. Ferroelec. Freq. Contr.*, 42:182–187, 1995.

[17] C. A. Damianou, N. T. Sanghvi, F. J. Fry, and R. Maass-Moreno. Dependence of ultrasonic attenuation and absorption in dog soft tissues on temperature and thermal dose. *J. Acoust. Soc. Am.*, 102(1):628–634, 1997.

[18] A. Derode, P. Roux, and M. Fink. Robust acoustic time reversal with high-order multiple scattering. *Phys. Rev. Lett.*, 75:4206–4209, 1995.

[19] P. F. Dobbins (ed.). *Arrays and Beamforming in Sonar, Vol. 18.* University of Bristol, U.K., 1996.

[20] C. Dorme and M. Fink. Focusing in transmit-receive mode through inhomogeneous media: The time reversal matched filter approach. *J. Acoust Soc. Am.*, 98:1155–1162, 1995.

[21] D. R. Dowling. Phase-conjugate array focusing in a moving medium. *J. Acoust. Soc. Am.*, 94:1716–1718, 1993.

[22] D. R. Dowling and D. R. Jackson. Narrow-band performance of phase-conjugate arrays in dynamic random media. *J. Acoust. Soc. Am.*, 91:3257–3277, 1992.

[23] F. Dupenloup, J. Y. Chapelon, D. J. Cathignol, and O. A. Sapozhnikov. Reduction of the grating lobes of annular arrays used in focused ultrasound surgery. *IEEE Trans. Ultrason. Ferroelec. Freq. Contr.*, 43:991–998, 1996.

[24] E. S. Ebbini and C. A. Cain. Multiple-focus ultrasound phased-array pattern synthesis: optimal driving-signal distributions for hyperthermia. *IEEE Trans. Ultrason. Ferroelec. Freq. Contr.*, 43:991–998, 1996.

[25] P. C. Etter. *Underwater Acoustic Modeling.* Elsevier Applied Science, New York, 1991.

[26] J. H. Ferziger and M. Perić. *Computational Methods for Fluids Dynamics.* Springer-Verlag, Berlin, 1996.

[27] M. Fink. Time reversal of ultrasonic fields - part i: Basic principles. *IEEE Trans. Ultrason. Ferroelec. Freq. Contr.*, 39:555–566, 1992.

[28] M. Fink. Time-reversal mirrors. *J. Phys. D: Appl. Phys.*, 26:1333–1350, 1993.

[29] F. J. Fry. Precision high intensity focused ultrasound machines for surgery. *Am. J. Phys. Med.*, 37:152–156, 1958.

[30] F. J. Fry and J. E. Barger. Acoustical properties of the human skull. *J. Acoust. Soc. Am.*, 63(5):1576–1590, 1978.

[31] Gerken. *Mine Warface Technology.* American Scientific Corp., 1989.

[32] S. A. Goss, L. A. Frizzell, J. T. Kouzmanoff, J. M. Barich, and J. M. Yang. Sparse random ultrasound phased array for focal surgery. *IEEE Trans. Ultrason. Ferroelec. Freq. Contr.*, 43:1111–1120, 1996.

[33] S. A. Goss, R. L. Johnston, and F. Dunn. Comprehensive compilation of empirical ultrasonic properties of mammalian tissues. *J. Acoust. Soc. Am.*, 62(2):423–457, 1978.

[34] S. A. Goss, R. L. Johnston, and F. Dunn. Comprehensive compilation of empirical ultrasonic properties of mammalian tissues. ii. *J. Acoust. Soc. Am.*, 68(1):93–107, 1980.

[35] S. A. Goss and S.-I. Umemura. Concentric-ring and sector-vortex phased-array applicators for ultrasound hyperthermia. *IEEE Trans. Microwave Theo. and Techniques*, 34(5):542–551, 1986.

[36] O. S. Haddadin and E. S. Ebbini. Ultrasonic focusing through inhomogeneous media by application of the inverse scattering problem. *J. Acoust. Soc. Am.*, 104(1):313–325, 1998.

[37] I. M. Hallaj and R. O. Cleveland. Fdtd simulation of finite-amplitude pressure and temperature fields from biolomedical ultrasound. *to appear in Acoust. Res. Lett. [http://asa.aip.org/arlo/]*, 1(1):7–12, 1999.

[38] I. M. Hallaj, R. O. Cleveland, and S. G. Kargl. *Two-dimensional nonlinear propagation of pulsed ultrasound through a tissue-like material.* American Institute of Physics, 1998.

[39] I. M. Hallaj, R. O. Cleveland, S. G. Kargl, and R. A. Roy. *FDTD simulation of transcranial focusing using ultrasonic phase-conjugate arrays. in Acoustical Imaging, Vol. 23, Lees and Ferrari (eds.).* Plenum Press, 1997.

[40] I. M. Hallaj, R. O. Cleveland, R. A. Roy, and R. G. Holt. Coupled thermal-acoustic simulation results with temperature-dependent tissue parameters for therapeutic ultrasound. *J. Acoust. Soc. Am.*, 104(3):1844, 1998.

[41] I. M. Hallaj, S. G. Kargl, and R. A. Roy. *Retrodirective array performance case studies and implications for mine countermeasures. in High Frequency Acoustics in Shallow Water, Pace et al. (eds.).* NATO SACLANT Undersea Research Centre, 1997.

[42] M. F. Hamilton and D. T. Blackstock. *Nonlinear Acoustics.* Academic Press, 1998.

[43] L. M. Hinkleman, D.-L. Liu, L. A. Metlay, and R. C. Waag. Measurements of ultrasonic pulse arrival time and energy level variations produced by propagation through abdominal wall. *J. Acoust. Soc. Am.*, 95(1):530–541, 1994.

[44] L. M. Hinkleman, D.-L. Liu, R. C. Waag, Q. Zhu, and B. D. Steinberg. Measurement and correction of ultrasonic pulse distortion produced by the human breast. *J. Acoust. Soc. Am.*, 97(3):1958–1969, 1995.

[45] M. M. Horder, S. B. Barnett, G. J. Vella, M. J. Edwards, and A. K. Wood. In vivo heating of the guinea pig fetal brain by pulsed ultrasound and estimates of thermal index. *Ultrasound in Med. & Biol.*, 24(9):1467–1474, 1998.

[46] K. Hynynen. The threshold for thermally significant cavitation in dog's thigh muscle *in vivo*. *Ultrasound in Med. and Biol.*, 17(2):157–160, 1991.

[47] K. Hynynen. Focused ultrasound surgery guided by MRI. *Science and Medicine*, 3(5):62–71, 1996.

[48] D. R. Jackson and D. R. Dowling. Phase conjugation in underwater acoustics. *J. Acoust. Soc. Am.*, 89:171–181, 1991.

[49] A. C. Kak and M. Slaney. *Principles of Computerized Tomographic Imaging.* IEEE Press, 1988.

[50] R. Kosloff and D. Kosloff. Absorbing boundary conditions for wave propagation problems. *J. Comp. Phys.*, 63:363–376, 1986.

[51] P. K. Kundu. *Fluid Mechanics.* Academic Press, San Diego, 1990.

[52] W. A. Kuperman, W. S. Hodgkiss, H. C. Song, T. Akal, C. Ferla, and D. R. Jackson. Phase conjugation in the ocean: Experimental demonstration of an acoustic time-reversal mirror. *J. Acoust. Soc. Am.*, 103:25–40, 1998.

[53] R. J. Lalonde and J. W. Hunt. Variable frequency field conjugate acoustic lenses for ultrasound hyperthermia. *IEEE Trans. Ultrason. Ferroelec. Freq. Contr.*, 40:825–831, 1993.

[54] R. J. Lalonde, A. Worthington, and J. W. Hunt. Field conjugate acoustic lenses for ultrasound hyperthermia. *IEEE Trans. Ultrason. Ferroelec. Freq. Contr.*, 40:592–602, 1993.

[55] R. J. Last. *Anatomy, Regional and Applied, 6th Edition.* Longman Group, 1978.

[56] R. Maass-Moreno and C. A. Damianou. Evaluation of accuracy of a theoretical model for predicting the necrosed tissue volume during focused ultrasound surgery. *IEEE Trans. Ultrason. Ferroelec. Freq. Contr.*, 42(2):182–187, 1995.

[57] T. D. Mast, L. M. Hinkelman, M. J. Orr, V. W. Sparrow, and R. C. Waag. Simulation of ultrasonic pulse propagation through the abdominal wall. *J. Acoust. Soc. Am.*, 102(2):1177–1190, 1997.

[58] P. M. Meaney, R. L. Clarke, G. R. ter Haar, and I. H. Rivens. A 3-d finite-element model for computation of temperature profiles and regions of thermal damage during focused ultrasound surgery exposures. *Ultrasound in Med. and Biol.*, 24(9):1489–1499, 1998.

[59] T. G. Muir and L. L. Mellenbruch. Reflection of finite-amplitude waves in a parametric array. *J. Acoust. Soc. Am.*, 62:171–181, 1977.

[60] G. Mur. Absorbing boundary conditions for the finite-difference approximation of the time-domain electromagnetic-field equations. *IEEE Trans. Electromag. Compatibility*, 23(4):377–382, 1981.

[61] A. D. Pierce. *Acoustics, An Introduction to its Physical Principles and Applications.* Acoustical Society of America, New York, 1991.

[62] O. T. V. Ramm and S. W. Smith. Beam steering with linear arrays. *IEEE Trans. Biomed. Eng.*, 30:438–452, 1983.

[63] N. T. Sanghvi and R. H. Hawes. High-intensity focused ultrasound. *Exper. and Investig. Endoscopy*, 4(2):383–395, 1994.

[64] A. Taflove. Review of the formulation and applications of the FDTD method for numerical modeling of electromagnetic wave interactions with arbitrary structures. *Wave Motion*, 10:547–582, 1988.

[65] G. ter Haar. Ultrasound focal beam surgery. *Ultrasound in Med. and Biol.*, 21(9):1089–1100, 1995.

[66] J.-L. Thomas and M. Fink. Ultrasonic beam focusing through tissue inhomogeneities with a time reversal mirror: Application to transskull therapy. *IEEE Trans. Ultrason. Ferroelec. Freq. Contr.*, 43:1122–1129, 1996.

[67] J.-L. Thomas, F. Wu, and M. Fink. Time reversal focusing applied to lithotripsy. *Ultrasonic Imaging*, 18:106–121, 1996.

[68] J. N. Tjøtta and S. Tjøtta. Nonlinear equations of acoustics, with application to parametric acoustic arrays. *J. Acoust. Soc. Am.*, 69:535–537, 1981.

[69] D. H. Turnbull and F. S. Foster. Beam steering with pulsed two-dimensional transducer arrays. *IEEE Trans. Ultrason. Ferroelec. Freq. Contr.*, 38:320–333, 1991.

[70] H. Wang, E. Ebbini, and C. A. Cain. Effect of phase errors on field patterns generated by an ultrasound phased-array hyperthermia applicator. *IEEE Trans. Ultrason. Ferroelec. Freq. Contr.*, 38:521–531, 1991.

[71] D. J. Watmough, R. Lakshmi, F. Ghezzi, K. M. Quan, J. A. Watmough, E. Khizhnyak, T. N. Pashovkin, and A. P. Sarvazyan. The effect of gas bubbles on the production of ultrasound hyperthermia at 0.75 mhz: A phantom study. *Ultrasound in Med. and Biol.*, 19(3):231–241, 1993.

[72] Q. Wen. *Spatial Diversity Equalization and Phase Conjugation Applied in Ocean Acoustic Communications.* PhD Thesis, University of Washington, Seattle, 1991.

[73] P. J. Westervelt. Parametric acoustic array. *J. Acoust. Soc. Am.*, 35:535–537, 1963.

[74] J. Wu, J. D. Chase, Z. Zhu, and T. P. Holzapfel. Temperature rise in a tissue-mimicking material generated by unfocused and focused ultrasonic transducers. *Ultrasound in Med. and Biol.*, 18(5):495–512, 1992.

[75] J. Wu and G. Du. Temperature elevation in tissues generated by finite-amplitude tone bursts of ultrasound. *J. Acoust. Soc. Am.*, 88:1562–1577, 1990.

[76] K. S. Yee. Numerical solution of initial boundary value problems involving maxwell's equations in isotropic media. *IEEE Trans. Antennas and Propagation*, 14(3):302–307, 1966.

[77] S. Yongchen, D. Yanwu, T. Jie, and T. Zhensheng. *Ultrasonic propagation parameters in human tissues, in Proceedings of the IEEE Ultrasonics Symposium, 1986.* IEEE, 1986.

Appendix A

THE FDTD METHOD AND OTHER NUMERICAL CONSIDERATIONS

A.1 Solving the Wave Equation Using FDTD

A numerical solution of the wave equation may be computed using the finite-difference time-domain (FDTD) method, which was introduced into use in its contemporary form by Yee [76]. The FDTD method provides accurate and detailed solutions down to the smallest scales of the problem. This strength of the FDTD method is also its greatest weakness, as the detailed calculations, called *full wave simulations*, require a large amount of computer storage space. Since the wavelengths in electromagnetic applications are large enough so that most systems can be represented by a few wavelengths, the FDTD method is widely used in the field of electromagnetics. With the development of faster and larger computers, however, more practical problems in acoustics will be solved using the FDTD method.

A.1.1 Approximating Partial Derivatives Using Finite Differences

The FDTD method approximates the spatial and temporal partial derivatives with discrete differences obtained from Taylor series expansions

$$f_i^{n+1} = f_i^n + \delta_t \frac{\partial f_i^n}{\partial t} + \frac{\delta_t^2}{2} \frac{\partial^2 f_i^n}{\partial t^2} + \frac{\delta_t^3}{3!} \frac{\partial^3 f_i^n}{\partial t^3} + \dots \qquad (A.1)$$

about some node on the computational grid indexed in time by n and in space by i. In two spatial dimensions (i, j):

$$\frac{\partial^2 p}{\partial x^2} = \frac{1}{\delta_x^2}(p_{i+1}^n - 2p_i^n + p_{i-1}^n) + \mathcal{O}(\delta_x^2),$$

$$\frac{\partial p}{\partial t} = \frac{1}{2\delta_t}(3p_i^n - 4p_i^{n-1} + p_i^{n-2}) + \mathcal{O}(\delta_t^2),$$

$$\frac{\partial^2 p}{\partial t^2} = \frac{1}{\delta_t^2}(p_i^{n+1} - 2p_i^n + p_i^{n-1}) + \mathcal{O}(\delta_t^2), \quad \text{(centered)} \tag{A.2}$$

$$= \frac{1}{\delta_t^2}(2p_i^n - 5p_i^{n-1} + 4p_i^{n-2} - p_i^{n-3}) + \mathcal{O}(\delta_t^2), \quad \text{(right-sided)}$$

$$\frac{\partial^3 p}{\partial t^3} = \frac{1}{2\delta_t^3}(6p_i^n - 23p_i^{n-1} + 34p_i^{n-2} - 24p_i^{n-3} + 8p_i^{n-4} - p_i^{n-5}) + \mathcal{O}(\delta_t^2)$$

Note that two versions of the second derivative were given in (A.2). The reason for this is that in the explicit method the future value of pressure is isolated to one side of the equation, and is solved for in terms of present and past values only. The time derivative appearing in the D'Alembertian in the wave equation was chosen to contain the future unknown pressure term in the FDTD solution. The other time derivatives, including the second order derivative in the nonlinear term were all done using right-sided finite differences, so they only contained known quantities. The reason for chosing the centered difference for the D'Alembertian time derivative is that the numerical solution behaved better with this combination.

Note that as the order of the derivative increases, more instances of the pressure field are needed to be held in storage. So for example, the third order time derivative requires the current (n) pressure field, as well as the pressure fields at previous time steps $(n-1), \ldots, (n-5)$. This requirement is further increased if the order of the differencing were higher than 2. The particular formulae used to approximate the derivatives can be obtained by following one of several formal methods [8]. The exact form will differ if the differencing is to be centered or right or left handed, meaning that the expression will contain indices around n or to the left or right of n. Typically, time derivatives are formulated so that only the known pressures from previous time steps

are required for the calculation, as the explicit method steps forward and calculates $p_{i,j}^{n+1}$ at each time step. This technique is called an *explicit method*. The first derivative can be used to calculate the difference expressions for higher order derivatives to the same accuracy by applying the first derivative expression recursively. The spatial differencing is similar, but is done using centered differences, and to fourth order accuracy, $\mathcal{O}(\delta_x)^4$:

$$\frac{\partial p}{\partial x} \approx \frac{1}{12\delta_x}(-p_{i+2,j}^n + 8p_{i+1,j}^n - 8p_{i-1,j}^n + p_{i-2,j}^n), \qquad (A.3)$$

$$\frac{\partial^2 p}{\partial x^2} \approx \frac{1}{12(\delta_x)^2}(p_{i+2,j}^n + 16p_{i+1,j}^n - 30p_{i,j}^n + 16p_{i-1,j}^n - p_{i-2,j}^n). \qquad (A.4)$$

The above expressions can be found in Ferziger and Perić [26].

Using these centered-difference expressions we can obtain the third derivative by using the first derivative expression as an operator on the second derivative, yielding the centered expression to fourth order,

$$\begin{aligned}
\frac{\partial^3 \phi}{\partial t^3} = \frac{1}{144\delta_t^3}(&\phi_{i+4} - 24\phi_{i+3} + 158\phi_{i+2} \\
&- 248\phi_{i+1} + 248\phi_{i-1} - 158\phi_{i-2} + 24\phi_{i-3} - \phi_{i-4}) + \mathcal{O}(\delta_x^4).
\end{aligned} \qquad (A.5)$$

Turning (A.5) into a right-sided finite difference expression can be done if the original fourth-order derivatives are right-sided, but was not used because it requires excessive run time. One point to make is that the order of the method does not imply or guarantee accuracy, it only indicates how rapidly the truncation errors decrease with decreasing δ_x or δ_t. For this reason it is possible for a second-order solution to be more accurate than a fourth-order solution. While second-order time differencing was used exclusively in this study, both second and fourth-order spatial differencing was used. The highly-steepened waveforms in the nonlinear time reversal study behaved better with fourth order differencing in space. Less numerical dispersion (numerical propagation of different wavenumbers at different velocities on the grid) was observed when the spatial grid spacing δ_x was made as small as possible, and the fourth-order differencing was used.

The need to reduce spatial grid size leads to a requirement to reduce the time grid spacing accordingly for stability reasons. In Cartesian coordinates, the explicit finite-difference solution of the lossless linear wave equation is stable only if

$$c_{\text{max}}\delta_t \leq \left(\frac{1}{\delta_x^2} + \frac{1}{\delta_y^2} \right).$$
(A.6)

This is a statement that no wave propagation information can travel across more than δ_x in a single time step δ_t. The stability criterion becomes much more complicated for the absorbing case, and simple Von Neumann stability analysis is not possible for the nonlinear wave equation, and is beyond the scope of this study. However, it was empirically observed that a trade off between α and δ_t exists in the stability space for the absorbing wave equation. In other words, increasing α necessitates increasing δ_t for stability. Perhaps the only positive side-effect of the instability issue which plagues explicit methods is that once a code is stable, its output is generally convergent. In our studies we compared second and fourth-order spatial differencing and found very good agreement. A full investigation of the dispersion and the stability characteristics of the FDTD codes used is beyond the scope of this study. Numerical dispersion will occur in all finite difference codes on uniform grids [64], but its effect is minimized by proper selection of the spatial grid size relative to the dominant wavelength. This "magic size" δ_t as it is referred to by Taflove turns out to be when equation (A.6) has an equality sign for the relationship.

This study also used implicit solutions of the wave equation, and the results were similar to the explicit results. However, the implicit solutions require more care to ensure convergence, as large δ_t will gradually reduce accuracy. By contrast increasing δ_t in the explicit solutions will lead to instability and failure of the computer code.

A.2 Modeling the Sources

Both discrete arrays and continuous (discretized) extended sources can be modeled with the techniques used in this study. To model an array having inter-element

separation larger than the spatial grid size a gap in the placement of point sources is allowed from which no sound will emanate. To model a continuous extended source, all grid points lying on the source are driven in phase. An extended source described by many sources much smaller than a wavelength located along the surface of the simulated extended source can be expected to collectively yield a wavefront similar to that of the extended source by Huygens' construction [61].
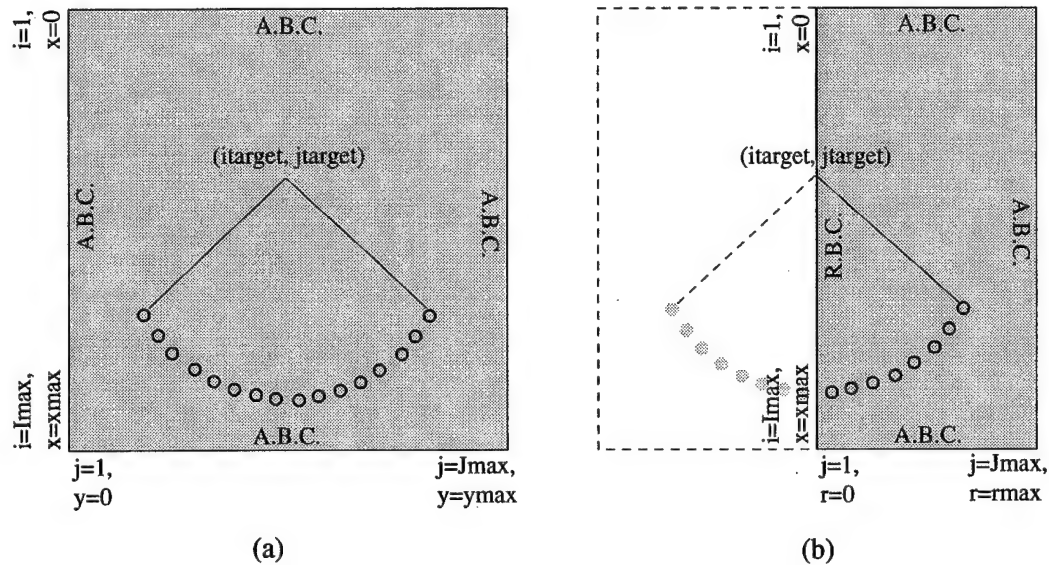

Figure A.1: The layout of the 2-D simulations in (a) Cartesian coordinates and (b) polar cylindrical coordinates. The computational domain is shaded. The boundary conditions used at the edges of the domain are either absorbing boundary conditions (ABC) or reflected boundary conditions (RBC).

A.2.1   Boundary Conditions

Two types of boundary conditions are described in this section. The absorbing boundary condition to prevent artificial wave reflections from the edges of computational domains, and the reflected boundary condition to enforce symmetry about a boundary which lies on an axis of symmetry. Since the spherical bowl sources do not guarantee

that the discretized point sources lie on exact grid positions in rectilinear coordinates, the nearest grid location was chosen in this case.

Absorbing Boundary Conditions

Since numerical simulations are carried out on finite computational domains, the issue of how to handle waves reaching the outer edges of the domains needs to be addressed. Untreated, acoustic waves reaching the edge of a computational domain would be reflected by the artificial boundaries of the simulation. In order to avoid this unnatural behavior when modeling extended regions in space, it is common to use absorbing boundary conditions (ABC's) along these edges.

Several techniques are known which prevent waves incident on domain boundaries from reflecting. We describe two different techniques here which were used successfully with the FDTD solution of the acoustic wave equation. The first involves placing an absorbing boundary layer along the edges of the computational domain in such a way as to minimize reflected wave amplitudes. This technique is described in Kosloff and Kosloff [50] for a wave equation in 2-D,

$$\frac{\partial^2 p}{\partial t^2} = \rho c^2 \left[\frac{\partial}{\partial x} \left(\frac{1}{\frac{\partial p}{\partial x}} \right) + \frac{\partial}{\partial y} \left(\frac{1}{\frac{\partial p}{\partial y}} \right) \right] - 2\gamma \frac{\partial p}{\partial t} - \gamma^2 p + Source. \qquad (A.7)$$

This ABC requires padding the computational domain with at least 10 to 20 highly absorbing grid cells, on which no useful calculations can be performed due to the artifice of the padding. Further, the slope of the profile of γ is a compromise between two evils: on one hand if the profile is too shallow, a wider padded region is necessary to absorb the wave. On the other hand if the absorbing region has a very steep profile the wave will be partially reflected by the change in impedance, depending on the wavelength of the wave compared to the width of the transition region. Which means that the absorbing boundary layer ABC results in different reflection coefficients for different incident frequencies, and would have to be optimized for best effect. A profile

for γ which produces good results is

$$\gamma = U_0 / \cosh^2(\sigma\, n), \qquad\qquad\qquad (A.8)$$

where U_0 is a constant describing the magnitude of the absorption near the edge of the domain, and σ controls the slope of the profile, and n is the number of grid cells over which the transition takes place from the nonabsorbing interior to the edge.

The second ABC implemented successfully in this study uses a radiation condition normal to the boundaries and was first described for the FDTD method by Mur [60], and is commonly known as Mur's ABC. This is the ABC of choice for the simulations presented in this dissertation. Mur's first-order ABC uses the first-order radiation condition

$$\left. \frac{\partial p'}{\partial x} - \frac{1}{c_0} \frac{\partial p'}{\partial t} \right|_{x=0} = 0 \qquad\qquad\qquad (A.9)$$

along the $x = 0$ boundary, and

$$\left. \frac{\partial p'}{\partial x} + \frac{1}{c_0} \frac{\partial p'}{\partial t} \right|_{x=x_{max}} = 0 \qquad\qquad\qquad (A.10)$$

along the $x = x_{max}$ boundary. The radiation conditions ensure that waves normally incident upon the boundaries are absorbed. However, for obliquely-incident waves the reflection coefficient increases as the direction of incidence departs from normal. For grazing incidence, the first-order Mur ABC's are very inefficient and a second-order Mur ABC may be used [60].

Recently, a type of ABC known as the perfectly matched layer method (PML) has been introduced, and is considered to be the most effective of all known ABC's [12]. The method is usually associated with spectral methods, and its implementation is more complicated than the other ABC's described above.

Reflected Boundary Conditions

Another type of boundary condition used in this study is the reflected boundary condition (RBC). This is the result of truncating the computational domain at a

region of symmetry, where two identical but opposing waves would meet. In our case we assumed azimuthal symmetry about the central axis of bowl transducers. Thus only one half of the 2-D (x r) plane need be computed, and the computational domain is $r = [0, r_{max}]$, $x = [0, x_{max}]$, as shown in Figure A.1 is used to obtain solutions on $r = [-r_{max}, r_{max}]$, $x = [0, x_{max}]$. This reduces the required storage space by half, and reduces the execution time. For such cases the boundary condition along the $r = 0$ edge is

$$\frac{\partial p'}{\partial r} = 0,$$
$$\frac{\partial T}{\partial r} = 0. \tag{A.11}$$

As a natural result, the term containing $1/r$ in the Laplacian for polar coordinates is dropped, since it is multiplied by $\partial p'/\partial r$.

Other types of boundary conditions

The RBC is closely related to the periodic boundary condition, which causes waves reaching and exiting one face of the computational domain to re-enter the computational domain from the opposite end. For example, if computer memory is limited we can "reuse" available space by allowing the wave to enter from the left of the domain immediately upon exiting from the right side of the domain. In both the reflected and the periodic boundary conditions, the variables near the edges of the domain are replaced by values taken from the adjacent and opposite sides of the boundary respectively.

A.3   Simulation Challenges

Ideally, computer simulations of acoustic fields would provide exact information regarding all field variables (pressure, velocity, *etc.*) over any size computational domain for any length of time desired. Realistically of course, computer resources such

as memory and execution time limit the size of any simulation. Several simulation parameters determine the extent of the maximum spatial domain and time span attainable.

The primary parameter that defines the size of a simulation in acoustics is the number of spatial dimensions and the number of wavelengths per dimension. Until recently, it was not possible to simulate realistic wave propagation problems in three dimensions over ranges greater than a few tens of wavelengths. Even today, such three-dimensional simulations are beyond the reach of most engineering workstations because the memory required to hold the variables being calculated is proportional to the total number of spatial grid points used. So for a n-dimensional simulation having N_λ wavelengths on a side in the computational domain, and N_γ grid points per wavelength, the total number, N_{total}, of data points needed to hold one scalar field quantity at any instant in time is

$$N_{total} = m(N_\lambda N_\gamma)^n, \qquad (A.12)$$

where m is an integer usually between 3 and 7, depending on the highest order of the time derivatives taken on the unknown in the wave equation, and the degree of accuracy used in the time differencing. For a 3-dimensional simulation, having 10 wavelengths on a side of a computational cube, each wavelength sampled by a modest 15 grid points, N_{total} is greater than 10^7 when the linear wave equation is solved to second order accuracy in time.

For the above reasons, unless the three-dimensionality significantly contributes to the qualitative yield of the simulation, two- and sometimes one-dimensional simulations are the choice for most research problems. Another item to note is that while N_γ of 15 to 25 is reasonable for most sinusoidal waves, this number must be increased to adequately sample wavefronts with steep gradients, such as shock waves.

REPORT DOCUMENTATION PAGE

Form Approved
OMB No. 0704-0188

| 1. AGENCY USE ONLY (Leave Blank) | 2. REPORT DATE
5/21/99 | 3. REPORT TYPE AND DATES COVERED
Final (5/1/96 - 7/31/99) |
|---|---|---|

4. TITLE AND SUBTITLE
Nonlinear Acoustics in Underwater and Biomedical Applications:
Array Performance Degradation and Time Reversal Invariance

5. FUNDING NUMBERS
N00014-96-1-1119

6. AUTHOR(S)
Ibrahim M. Hallaj

7. PERFORMING ORGANIZATION NAME(S) AND ADDRESS(ES)
Applied Physics Laboratory
University of Washington
1013 NE 40th St.
Seattle, WA 98105-6698

8. PERFORMING ORGANIZATION REPORT NUMBER

9. SPONSORING/MONITORING AGENCY NAME(S) AND ADDRESS(ES)
Office of Naval Research
800 N. Quincy St.
Arlington, VA 22217-5660
    Attn: Dr. Randall Jacobson, Code 321TS

10. SPONSORING/MONITORING AGENCY REPORT NUMBER

11. SUPPLEMENTARY NOTES
Report is a dissertation submitted in partial fulfillment of the requirements for the degree of PhD, University of Washington

12a. DISTRIBUTION/AVAILABILITY STATEMENT

Approved for public release

12b. DISTRIBUTION CODE

13. ABSTRACT (Maximum 200 words)

This dissertation describes a model for acoustic propagation in inhomogeneous fluid media and explores the focusing by arrays onto targets under various conditions. The work explores the use of arrays for acoustic and biomedical applications. Aspects of propagation and phasing that can lead to reduced focusing effectiveness are described. Among the most important debilitating effects studied here are medium absorption, medium nonlinearity, and imperfect initial phasing of the signals at the array elements.

Acoustic wave propagation in fluid media is modeled by obtaining a wave equation from the basic equations of fluid mechanics, and from some description of the propagating environment and its boundaries. This study uses analysis and numerical simulations to study the behavior of the acoustic focusing systems described. The finite-difference time-domain method is used to solve the wave equation for some applications, and the strengths and weaknesses of this method are discussed.

Beyond modeling and simulating the propagation and focusing of acoustic fields, this dissertation looks at the heating effects of ultrasound in an absorbing thermoviscous fluid. The application considered is the deposition of ultrasonic energy onto target tissue regions for the purpose of effecting therapeutic heating for hyperthermia.

14. SUBJECT TERMS
acoustic wave propagation, nonlinear acoustics, underwater acoustics, biomedical acoustics, focused ultrasound surgery, time reversal arrays, therapeutic ultrasound

15. NUMBER OF PAGES

16. PRICE CODE

| 17. SECURITY CLASSIFICATION OF REPORT
Unclassified | 18. SECURITY CLASSIFICATION OF THIS PAGE
Unclassified | 19. SECURITY CLASSIFICATION OF ABSTRACT
Unclassified | 20. LIMITATION OF ABSTRACT
UL |
|---|---|---|---|